



# VNIVERSITAT DE VALÈNCIA

PhD in Nanoscience and Nanotechnology

- PhD thesis -

## Interfacial Engineering in Vacuum-Deposited Perovskite Solar Cells for Improved Performance and Space Stability

PhD candidate:

**Daniel Pérez del Rey**

Supervisors:

**Prof. Hendrik J. Bolink**

**Dr. Pablo P. Boix**

Tutor:

**Prof. Hendrik J. Bolink**

September 2021



**Prof. Hendrik J. Bolink y Dr. Pablo P. Boix**, profesor de la Universidad de Valencia en el Instituto de Ciencia Molecular (ICMol) e investigador postdoctoral del Instituto de Ciencia de los Materiales (ICMUV), respectivamente, certifican que la memoria presentada por el doctorando Daniel Pérez del Rey con el título “*Interfacial Engineering in Vacuum-Deposited Perovskite Solar Cells for Improved Performance and Space Stability*” corresponde a su tesis doctoral y ha sido realizada bajo su dirección, autorizando mediante este escrito la presentación de la misma.

En Valencia, a 23 de septiembre de 2021

Prof. Hendrik J. Bolink

(director y tutor)

Dr. Pablo P. Boix

(director)



*“The beauty of a living thing is not the atoms that go into it,  
but the way those atoms are put together.”*

Carl Sagan

*A mi tía*



## Acknowledgments

Firstly, I want to thank my supervisor, Prof. Hendrik J. Bolink. Thank you, Henk, for giving me the opportunity of joining your group. When I started, I had no idea about perovskites, but you trusted me anyway. You have always treated me with respect and gave me freedom to be myself in the lab. I feel very lucky of being part of your group and having you as my supervisor. You are a great director and group leader, always listening our concerns and requirements, and offering solutions to our problems, and I am fully sure that I will miss that in my future life path. These have been the best years of my life, and it is an honour for me to say that I did my thesis in your group. Quiero agradecer también a mi subdirector de tesis, Pablo Boix, primero por los grandes momentos que hemos pasado, muy divertidos y que espero que vuelvan a ocurrir cuando el mundo vuelva a la normalidad. Pero también por todo lo que he aprendido contigo, sobre ciencia en particular, pero también consejos de la vida. Y sobre aquel viaje a Sevilla del que no voy a hablar, que esto lo va a leer mi madre. No me puedo dejar a Michele, quien fue mi mayor apoyo en mis inicios como científico, siempre encontrando tiempo en su apretada agenda para charlar conmigo sobre mis resultados y responder a mis dudas con un nivel de detalle muy alto. No sé si leerás esto, pero espero que no pierdas la ilusión, eres un guía y un gran apoyo para mucha gente y este grupo nunca habría podido funcionar sin ti. Y los memes de Michele (o memecheles) están graciosos.

Now, I want to thank the people that has been in the group during these years and that now are gone. Thank you, David, you taught me how to do the basic processes for making a perovskite solar cell and gave me a warm welcome when I joined the group. Gracias Enrico por tu sentido del humor y ser el fan número 1 de mis memes, si los sigo haciendo es en parte por ti. Toni, siempre te recordaré como una de las personas más agradables del grupo de Henk. Giulia y Maria Grazia, mis dos italianas favoritas con las que tantas excursiones y fiestas hemos hecho. Espero que no perdamos el contacto y nos sigamos encontrando en nuestros caminos, sois geniales y os tengo mucho aprecio. Cris, para mi

eres la persona más trabajadora que he conocido, una persona perfeccionista y luchadora que nunca se rinde y que destila sabiduría. Espero que encuentres tu lugar en el mundo, donde encajes y se te valore. Benni, te quiero agradecer lo bien que nos lo hemos pasado juntos y lo buena persona que has sido siempre conmigo. Azin, eres genial y se te echa mucho de menos, especialmente tu sentido del humor y alegría de la vida (y tus recetas de Irán :D). Vaheed, you are great and unique, please don't change and keep always that attitude. I really hope we will meet again and have lots of fun and kebab. Jorge, se te echa de menos por aquí, nuestros cafés, charlas frikis y experimentos juntos. Has sido un buen amigo en el laboratorio, y sé que seguiremos haciendo grandes planes fuera, en persona o en la red. Eres una persona de gran valor. Ana, fuiste un gran apoyo en nuestras aventuras en el Máster, encontré en ti una buena amiga que espero mantener por siempre. Vales mucho y espero que te sirva para llegar a donde te propongas. Y sé que puedo contar contigo para cualquier cosa, lo cual no es fácil de encontrar.

Lau, aunque deberías ir en el grupo anterior, todavía me cuesta admitir que te has ido. Sigo mirando a la puerta de la sala limpia cuando entra alguien esperando que seas tú y se haga más amena la estancia. Has sido (y eres) un gran apoyo y una excelente compañera. Has dejado tu huella en el laboratorio y da igual donde mires, puedes encontrar algo que es mejor gracias a ti, incluido yo mismo. Siempre conservaré un grato recuerdo de nuestro camino juntos. Eres una de las personas más inteligentes e inconformistas que he conocido, y estoy convencido de que seas profesora, ingeniera industrial o dibujante, serás la mejor. No dejes que nada te borre la sonrisa (esta frase es de un azucarillo).

Lidón, simplemente eres genial. Eres una buena persona, sin maldad, sin rencor y que cuesta infinito hacer enfadar. Haces que un día gris mejore al instante. Sin menospreciar a nadie, este grupo está donde está en gran medida gracias a ti, de manera directa e indirecta. Eres incansable y trabajadora como una hormiga, si te sobran 10 minutos te pones a calibrar una capita de C<sub>60</sub> timidilla jaja. Si algún día monto una empresa serás la primera persona a la que llame, sin lugar a duda. Te tengo mucho cariño y espero que a la larga nuestros caminos no se separen mucho.

I also want to thank my actual colleagues, the ones that have been for longer time and also the new ones. You are very hard-working people, very kind and nice, and you are building a new generation for the group in which I really trust. I hope we can make great parties when we are all fully vaccinated. Danke Chris für deine Hilfe bei meiner Reise nach Deutschland, deine Hilfe bei der Physik und für unsere Ausflüge und Exkursionen. Gracias Isidora por ser tan agradable conmigo (y por ser mi modelo :P), eres muy trabajadora y una magnífica persona. Kassio, espero que te mantengas incansable, eres la persona en la que más confío para mantener este grupo funcionando. For the rest, I didn't have the chance to know you better, but we still have time to live new adventures. Thanks to Paco, Lorenzo, Paz, Argha, Nathan, Sang, Bas, Abhi and Lucía. I wish you the best in your PhD and your life, and you can count with me for any help.

Quiero hacer una mención especial a Jorge Ferrando, nuestro ingeniero y solucionador de problemas. Gracias por estar siempre ahí, por trabajar a sol y sombra y siempre estar pendiente de que tengamos todo en la mejor forma posible. Eres una pieza fundamental de este grupo y estamos aquí todos gracias a ti. El día que no estés estoy convencido de que Henk tendrá que meter a 2 personas para llenar tu hueco. No dejes que nadie te infravalore. También a María Monrabal, quien trabaja desde la sombra, pero cuyo trabajo es fundamental para que todo funcione. No creo que haya nadie que ponga en duda que eres otra pieza clave en este grupo y una magnífica persona. Me gustaría incluir en la mención especial a dos de mis profesoras del colegio, Esperanza y Gabi, la primera me enseñó a amar la química y es por ella que hoy estoy aquí, y la segunda fue un gran apoyo y estuvo siempre pendiente de mí. Nunca os olvidaré, gracias.

Mis agradecimientos van también a la gente que no es de mi grupo. A los del grupo de Eugenio con quienes tan bien me lo he pasado en fiestas y tomando un café después de comer, a Javi López, Javi Castells, José Alberto, Mario, Euge, Ale, Víctor y muchos más... las mejores fiestas las he vivido con vosotros y vosotras, y espero que aun tengamos la oportunidad de vivir unas cuantas más. Sois buena gente y unas personas increíbles, os deseo lo mejor. Gracias Cristian, eres un tío auténtico, una buena persona y el tipo de gente con el que me siento

tranquilo porque haces que los problemas desaparezcan. Ángel, mi compañero de astronomía, te aprecio mucho como persona, eres alguien que es capaz de dejarlo todo por ayudarte, incansable y trabajador, espero que nunca cambies y que tengamos la oportunidad de seguir viviendo aventuras bajo las estrellas.

No me puedo olvidar de mis amigos de fuera del laboratorio, quienes han hecho (y hacen) que mis días sean mejores y con quienes puedo desconectar del trabajo. Gracias Javi (british) por los grandes momentos que vivimos aprendiendo inglés, las risas jugando a cualquier mierda y nuestros viajes y aventuras. Eres de las pocas personas con quien puedo ser yo mismo al 100% sin sentirme raro. Gracias al otro Javi (García), mi amigo de la carrera, con quien más me siento identificado y con quien me gusta charlar de la vida y contarle mis pensamientos y problemas (y echar unas partidas con cerveza de barrica malarda). Pablo, nos conocemos hace poco, pero nuestra conexión ha sido muy fuerte. Encuentro en ti un amigo de verdad, de esos que sabes que no te va a fallar ni traicionar. Eres una persona súper inteligente y polivalente, y tengo fe ciega en que llegarás lejos. Además, sé que da igual donde nos lleve la vida que nos seguiremos encontrando. Me dejo a mucha gente, gracias a todas las personas que me consideráis vuestro amigo.

No me olvido de dar las gracias a mi familia. Me siento muy afortunado de haber nacido en esta familia, sois todos buena gente y siento que siempre os tendré ahí para lo que haga falta. Si estoy hoy aquí es gracias a haber nacido a vuestro lado. Si me lo permitís, voy a empezar por mi tía, a quien va dedicada esta tesis. Has sido una persona muy especial y siempre que imaginé el día de mi defensa te veía la primera. Sé que estarías orgullosa de mí, y no pasa un día en el que no me acuerde de ti, de tu alegría y tu amor infinito. Te queremos y no te olvidamos. A mis primos valencianos, Pablo y Javi, sois como mis hermanos, y sé que si tengo un problema no me fallaréis. Si alguien me quiere hacer daño ahí estaréis para recibir el golpe por mí. Espero algún día llegar a ser tan fuerte y valiente como vosotros. Somos un equipo de remo. A mi tío Jose, eres para mí un referente en muchas cosas, esfuerzo, dedicación, constancia, resiliencia... da igual cuantos golpes te dé la vida, que siempre te levantas. No sé qué me deparará el futuro, pero espero ser al menos la mitad de fuerte que tú. A mi familia del norte, aunque la

distancia nos separa os llevo dentro cada día. Sé que si algún día vivo cerca vuestra nada me faltará, y eso es algo que no se encuentra fácilmente. Sois una piña y espero que siempre sigáis así. Espero que nos podamos ver pronto. Os quiero.

Finalmente, a mis padres, los artífices de todo esto. Hoy estoy aquí y soy quien soy gracias a vosotros. Os habéis desvivido por mí, me lo habéis dado todo, siempre con una sonrisa y con el mayor amor que existe. No ha sido fácil el camino, pero aquí estamos. Os lo debo todo y más, y siempre estaré en deuda con vosotros, por darme la vida y gran parte de la vuestra. Nunca querré a nadie tanto como a vosotros y solo espero llegar a ser la mitad de buena persona y adulto funcional de lo que sois vosotros. Esta tesis es, en gran parte, vuestra también. Os quiere vuestro hijo.



# Contents

<b>1. Introduction and aim of the thesis</b>	<b>19</b>
1.1 Renewable Energy Paradigm	19
1.2 Perovskite solar cells	21
1.3 Perovskites for solar cell applications	22
1.4 Deposition techniques	26
1.5 Vacuum deposition	27
1.6 Main device architectures	29
1.7 Metal oxides as transport layers	30
1.8 Aim of the thesis	32
<b>2. Experimental and methods</b>	<b>35</b>
2.1 Materials for solar cell fabrication	35
2.2 Fabrication of $\text{CH}_3\text{NH}_3\text{PbI}_3$ perovskite	36
2.3 Fabrication of a P-i-N solar cell	38
2.4 Fabrication of an N-i-P solar cell	40
2.5 Thin-film characterization	41
2.6 Solar cell characterization	41
<b>3. Interfacial Modification for High-Efficiency Vapor-Phase-Deposited Perovskite Solar Cells Based on a Metal Oxide Buffer Layer</b>	<b>51</b>
3.1 Introduction	51
3.2 Experimental and methodology	53
3.3 Results and discussion	54
3.4 Conclusions	57
3.5 Contribution of the author	58

4. Molecular Passivation of MoO <sub>3</sub> : Band Alignment and Protection of Charge Transport Layers in Vacuum-Deposited Perovskite Solar Cells	73
4.1 Introduction	73
4.2 Experimental and methodology	76
4.3 Results and discussion	77
4.4 Conclusions	81
4.5 Contribution of the author	82
5. Perovskite Solar Cells: Stable under Space Conditions	95
5.1 Introduction	95
5.2 Experimental and methodology	97
5.3 Results and discussion	98
5.4 Conclusions	101
5.5 Contribution of the author	102
6. Conclusions	117
7. Resumen en castellano	121
7.1 Capítulo 1: Introducción	121
7.1.1 Células solares de perovskita	122
7.1.2 Perovskitas para uso fotovoltaico	123
7.1.3 Técnicas de deposición	124
7.1.4 Deposición a vacío	125
7.1.5 Óxidos metálicos como capas transportadoras	126
7.1.6 Objetivos de la tesis	127

7.2	Capítulo 2: Metodología experimental	127
7.2.1	Materiales	127
7.2.2	Fabricación de la perovskita de $\text{CH}_3\text{NH}_3\text{PbI}_3$	128
7.2.3	Fabricación de los dispositivos	128
7.2.4	Caracterización de las células solares	129
7.3	Capítulo 3: Modificación interfacial en células solares de perovskita evaporadas basada en un óxido metálico	129
7.3.1	Introducción	129
7.3.2	Resultados y discusión	131
7.4	Capítulo 4: Pasivación molecular del $\text{MoO}_3$ : Alineamiento de bandas y protección de las capas transportadoras en células solares de perovskitas evaporadas.	132
7.4.1	Introducción	132
7.4.2	Detalles experimentales y metodología	133
7.4.3	Resultados y discusión	133
7.5	Capítulo 5: Células solares de perovskita: estables en condiciones espaciales	135
7.5.1	Introducción	135
7.5.2	Detalles experimentales y metodología	136
7.5.3	Resultados y discusión	137
7.6	Capítulo 6: Conclusiones	138
8.	Bibliography	141
	Index of figures	157
	Index of tables	161
	List of publications	167



# **Chapter 1**

## **Introduction and aim of the thesis**

*“If you wish to make an apple pie from scratch, you must first invent the universe.”*

Carl Sagan



# 1. Introduction and aim of the thesis

## 1.1 Renewable Energy Paradigm

Humanity needs energy to live and evolve, both as individuals and as a society. Energy in the universe is available in many forms and we need to find new ways of converting it into something useful efficiently and cleanly. 80% of the energy is currently obtained from non-renewable sources (figure 1), which are finite and generate by-products such as carbon dioxide or methane that contribute to global warming through the greenhouse effect. This is leading to an increase in the global temperature, presenting the main anthropogenic risk for our civilization.

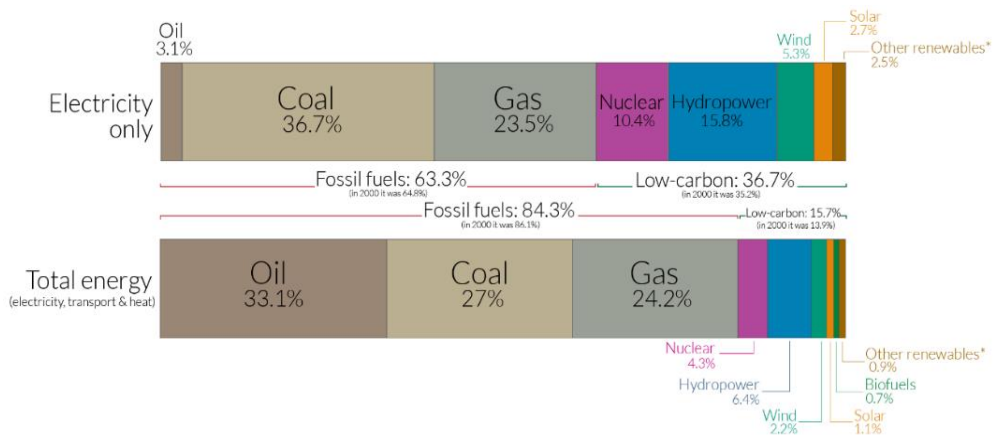


**Figure 1:** Global energy generation by source. Caption from reference 1.

When picturing an endless and clean energy source, the first thing we think of is the Sun. With almost 5 thousand million years of non-stop energy generation, the Sun obtains its energy from nuclear fusion. We are still far from functional artificial power production with this method. Still, we can learn something that microorganisms already knew 3000 million years ago: the Sun gives us energy for free. Solar energy can be employed from different approaches, such as wind farms, thanks to the temperature gradients in our atmosphere. Although wind generation and undoubtedly nuclear fission are excellent candidates for a transition from fossil fuels towards cleaner

alternatives, photovoltaics is the most versatile and adaptative method because the amount of available energy per unit area is enormous. Photovoltaic solar cells are the most direct way to convert solar energy into usable electrical power, transforming photons into an electrical current through the photoelectrical effect. Solar cells are such a clear candidate to become the primary source of energy generation that solar farms around stars (variations of the so-called Dyson spheres) are considered a key footprint of advanced alien civilizations.<sup>2</sup>

Nowadays, silicon dominates the mainstream market of solar cells, with more than 80% of the global annual production.<sup>3</sup> Polycrystalline silicon is cheap and works as expected, but it is not the most efficient material compared to other technologies such as monocrystalline silicon. The latter is much more efficient, but the cost and complexity of production is higher. In addition, both have the disadvantage of their indirect bandgap, leading to a poorer light absorption, and therefore needing to be very thick to absorb enough light. Alternatives include amorphous silicon, CdTe and CIGS (Copper Indium Gallium Selenide), prepared in thin films due to their higher absorption coefficients. GaAs solar cells are more efficient, although the production cost is too high for their extended use, being relevant only in very technical fields such as space applications where the power generated per gram must be as high as possible.

There are also emerging photovoltaic technologies with interesting properties, such as easiness of deposition, flexibility or potential low cost, yet with lower performance and stability compared to the previous technologies described. Some examples are copper zinc tin sulfide (CZTS) solar cells, dye-sensitized solar cells, organic solar cells, quantum dot solar cells, and perovskite solar cells.<sup>4</sup> Perovskite solar cells stand out from this list due to their advantageous properties, such as high absorption coefficient, low exciton binding energy, or bandgap tunability, that will be described in detail in the following sections. These properties allow them to directly compete with silicon solar cells in terms of efficiency and with GaAs solar cells in terms of power-to-weight ratio. Not only are they efficient, but also the production costs are much lower due to the low prices of the materials and their abundance.<sup>5</sup> These and many other vital factors that will be addressed during this thesis make them an excellent candidate for future applications on earth and even in space.

## 1.2 Perovskite solar cells

In a semiconductor, when a photon with enough energy is absorbed, an electron is promoted from the valence band to the conduction band. The energy difference between the valence band and the conduction band is referred to as the bandgap ( $E_g$ ), described as the minimum amount of energy required for a photon to be absorbed by the material. The vacancy left from the photogenerated electron in the valence band can be usefully described and formalized as a positively charged particle or entity, called a hole. Depending on the coulombic interaction between these photogenerated charge carriers, photons absorbed by the semiconductor can form a bound state called exciton, which can decouple to create free electrons and holes. The balance between free carriers and excitons in a semiconductor depends on the exciton binding energy. If it is higher than the thermal energy at room temperature ( $kT$ ), the semiconductor is mainly excitonic. Otherwise, free carriers will be the dominant species, being the latter advantageous for a solar cell as no energy is wanted for separating excitons.

In perovskite solar cells (PSCs), the photons are absorbed in the photoactive material, the perovskite. Photogenerated electron-hole pairs only exist, on average, for a finite length of time until they are extracted, producing work, or recombining either radiatively or non-radiatively. One way of reducing the recombination rate is to induce a concentration gradient to separate the carriers. This can be achieved by sandwiching the perovskite absorber between charge selective materials, which are permeable for electrons (or holes), and block the reciprocal charge carrier generating a gradient that can act as the driving force. Typically, these materials are P-type and N-type semiconductors, with an excess of negative (N) or positive (P) charge induced chemically or by doping, which creates energy states close to the conduction or valence band, respectively, forming the so-called P-i-N junction. The concentration of carriers determines the Fermi level ( $E_F$ ). The difference between the contacts'  $E_F$  leads to a "built in" potential ( $V_{bi}$ ). Therefore, the electrical field induced by this voltage can act as a driving force for the photogenerated carriers beyond the diffusion, being extracted to the external circuit separately thanks to the selectivity of these semiconductors (figure 2).

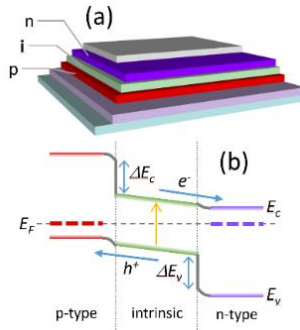


**Figure 2:** P-i-N device architecture (a) and potential profile (b).

In open circuit conditions there is no external circuit and hence no flow of electrons and holes, which end up recombining in this flat-band situation. At short circuit, when applying voltages lower than the built-in, diffusion and drift current have the same sign and photogenerated charges are extracted to the external circuit. Oppositely, when a voltage larger than the built-in is applied, the diffusion current is overtaken by the drift current. The external field accelerates charges through the junction, and electrons and holes are injected into the absorber.

### 1.3 Perovskites for solar cell applications

In geology, a perovskite is a mineral composed of calcium titanate ( $\text{CaTiO}_3$ ). Still, in a more general sense, it is any material that shares this crystal structure, generally expressed as  $\text{ABX}_3$  where A is a monovalent cation, B is a divalent cation, and X a monovalent anion. The unit cell, depicted in figure 3, comprises a ‘B’ cation coordinated in octahedra with 6 ‘X’ anions, filled with the ‘A’ cations at the interstitial holes between 8 octahedra.

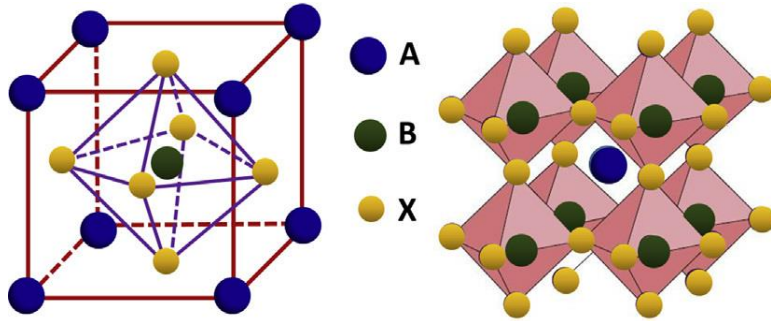


**Figure 3:** Perovskite general  $ABX_3$  crystal structure. Figure from reference 6.

Not every element can form the perovskite structure. One key parameter to determine if a set of elements could form a stable perovskite structure is their atomic radius ( $r_A$ ,  $r_X$  and  $r_M$ ), which enables the determination of the Goldschmidt tolerance factor ‘ $t$ ’, where a tolerance factor of  $0.7 < t < 1.1$  typically predicts stable structures. In fact, the different state-of-the-art perovskite compositions have their tolerance factors inside this range (figure 4).

$$t = \frac{r_A + r_X}{\sqrt{2}(r_M + r_X)}$$

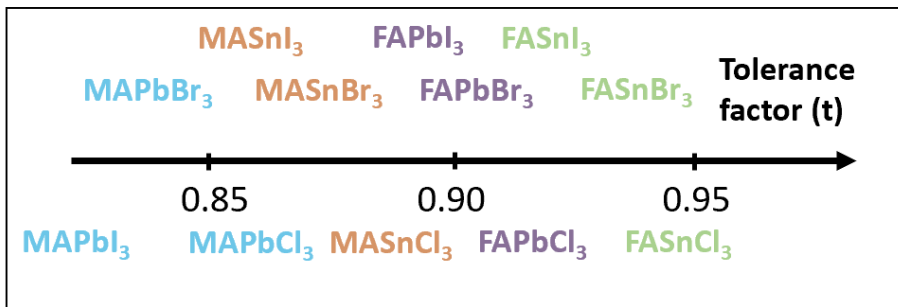


**Figure 4:** Tolerance factors of the most used perovskites for photovoltaic applications.

Focusing on perovskites relevant for optoelectronic applications, the ‘A’ cation is a small organic molecule such as methylammonium ( $\text{CH}_3\text{NH}_3^+$ ), formamidinium ( $\text{NH}_2\text{CHNH}_2^+$ ), or a small ion such as cesium ( $\text{Cs}^+$ ). The ‘B’ divalent cation is a metal with stable octahedral coordination such as  $\text{Pb}^{2+}$  or

$\text{Sn}^{2+}$ , and the ‘X’ anion is a halide, generally iodide ( $\text{I}^-$ ) and bromide ( $\text{Br}^-$ ) but also chloride ( $\text{Cl}^-$ ) is sometimes used.

By choosing different A, B, and X ions or molecules, one can change the material’s optical and electronic properties in very different ways. The conduction band of halide perovskites is formed from the antibonding orbitals of the hybridization of Pb p orbitals and halide s orbitals, whilst the valence band is formed from the antibonding states of the hybridized Pb s and halide p-orbitals. As the conduction band is mostly influenced by the energy of the Pb p atomic orbitals, the halide exchange affects mainly the valence band, resulting in an increase in the bandgap energy when replacing the I atom for Br or Cl. On the other hand, the A site cation does not directly participate in the bonding and only influences the electronic structure indirectly by changing the volume of the perovskite lattice (figure 5).<sup>7-10</sup> Changing the size of the A cation, for example, replacing partly or totally the  $\text{CH}_3\text{NH}_3^+$  with  $\text{Cs}^+$  or  $\text{NH}_2\text{CHNH}_2^+$ , generally increases the volume or distortion of the lattice, which leads to a decrease in the Pb energy levels. Varying the A cation leads to small changes in volume and structure, and, consequently, the bandgap is only slightly affected.<sup>7</sup> In contrast, it does have a rather high impact on chemical properties of the perovskite such as temperature stability.

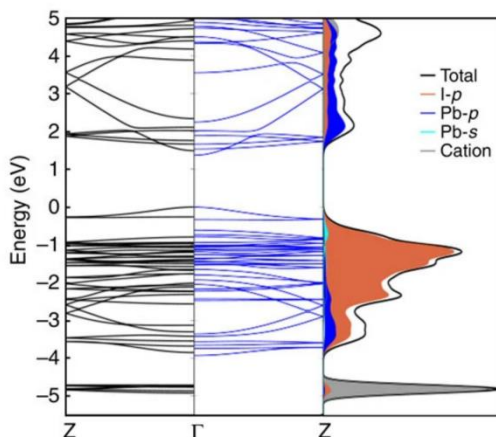


**Figure 5:** Band diagram of  $\text{CH}_3\text{NH}_3\text{PbI}_3$ . Image from reference 11.

The classical perovskite used for photovoltaic applications is methylammonium lead triiodide ( $\text{CH}_3\text{NH}_3\text{PbI}_3$ ), sometimes abbreviated as MAPI or just MAPI. Its crystal structure has a reversible tetragonal ( $\beta$ ) to cubic ( $\alpha$ ) phase transition at about 56 °C,<sup>12,13</sup> although it has been found in a stable

cubic structure at room temperature.<sup>14</sup> It exhibits suitable properties for a solar cell<sup>15–19</sup> such as:

- High optical absorption coefficient over a broad wavelength range, comparable to semiconductors used in high efficiency solar cells such as GaAs or CdTe,<sup>20</sup> allowing the perovskite solar cells to harvest the photons efficiently while maintaining a low thickness, which increases the already mentioned power-to-weight ratio and opens the possibility of deposition on flexible substrates.
- Low exciton binding energy: Upon photon absorption, electron-hole pairs are generated, also called excitons. The critical factor for a solar cell is separating this quasiparticle into its two components and extracting them separately. Hybrid perovskites have high dielectric constants, which has a shielding effect, thus reducing the binding energy of the electrons and holes, facilitating the generation of free carriers in the perovskite at room temperature.<sup>21–24</sup>
- Long charge carrier diffusion lengths: Diffusion lengths for both electrons and holes have been found to be larger than the minimum thickness needed to harvest 95% of the photons with an energy above the bandgap.<sup>25–27</sup> This means an increase in the photon collection and current generation without reducing the device's performance.<sup>28–33</sup>
- High defect tolerance: One of the key features of metal halide perovskites is the fact that defects in their crystal structure have a very low impact on the final performance of the device. Although those defects can induce electronic states which could act as recombination centers, they generally tend to be very shallow or localized in the electronic bands, having no negative impact on the overall performance.<sup>34</sup> Hence, no single crystals are needed, and they can be processed using low-cost techniques.

## 1.4 Deposition techniques

As mentioned before, the perovskites can be deposited with simple techniques and without the need of controlling in detail the crystallinity. There is a wide variety of low-cost deposition techniques available (figure 6). The deposition technique has some impact on the final properties of the film, such as the crystallinity, grain size, or maximum thickness.<sup>28,35</sup> Thus, the goal when preparing a perovskite layer is to maximize all the beneficial properties previously described to reach the highest power conversion efficiencies. The most used deposition techniques can be separated into two groups: solution-processed, where a solvent is used to dissolve the perovskite components, and dry methods, such as vacuum deposition, which will be addressed more deeply in the next section as it is the main technique used in this thesis.

Solution process methods employ polar solvents such as N,N dimethylformamide (DMF), dimethyl sulfoxide (DMSO), or  $\gamma$ -butyrolactone (GBL) to dissolve the perovskite components. Then, the solution can be deposited using different methods, such as blade coating or spin coating via a one-step or two-step deposition. In the one-step method (figure 6, a), the perovskite is formed by direct spin-coating of the precursor solution, and the process is controlled by the solvent evaporation speed and by the subsequent crystallization of the solid perovskite film. Choosing a proper substrate and parameters such as the spinning speed of the substrate and annealing temperature to remove the excess of solvent is fundamental to achieve the desired optoelectronic properties.<sup>36</sup> In order to improve the control of the crystallinity of the perovskite layer, this method has incorporated the addition of a small amount of another solvent in which the perovskite is not soluble (antisolvent) during the drying. This step promotes and triggers the crystallization, leading to better quality layers with the highest efficiencies reported.<sup>37-41</sup> For the two-step deposition method (figure 6, b), the metallic salt (usually  $PbX_2$ ) is first deposited from a solution, and then it is converted into perovskite by exposing it to the rest of the components. This can be done by spin coating a solution of the monovalent cation or by simply dipping the  $PbX_2$  layer into it. The final layer is usually annealed to remove the remaining solvents and promote the reaction of the components.<sup>42-45</sup> This process can also be combined with vacuum sublimation, for example, by depositing the  $PbX_2$  layer by evaporation and converting it into perovskite with a solution of the organic cation, or the opposite, converting the solution processed  $PbX_2$  layer into perovskite by exposing it to the vapor of the cation. When both

components are deposited by evaporation, we speak of vacuum deposition, described in the next section.

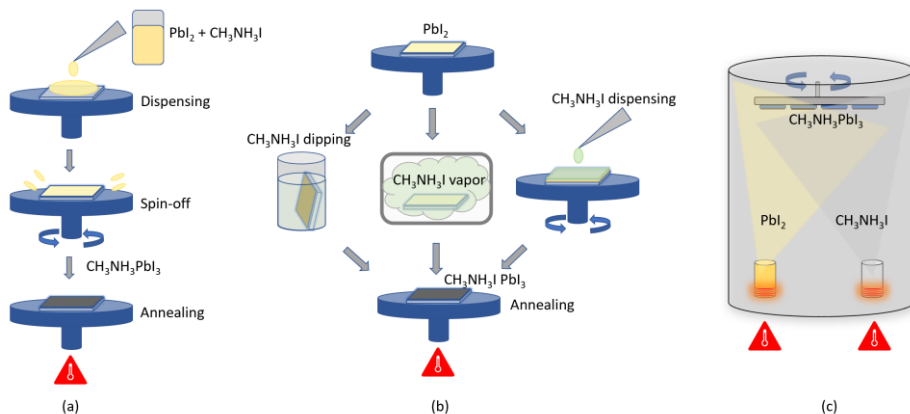


**Figure 6:** Most employed deposition techniques for the preparation of perovskite layers. 1 step deposition (a), 2 step deposition via solution processing of both components or a combination of solution processing and vacuum deposition (b) and co-evaporation (c).

## 1.5 Vacuum deposition

From all the deposition techniques, vacuum sublimation stands out due to several advantageous characteristics. This method consists in subliming in high vacuum the required precursor materials for a certain composition, depositing the resulting perovskite onto a substrate. It presents some advantages with respect to the techniques previously discussed, such as:

- High purity of the materials: due to the difference in sublimation temperature, impurities generally are not sublimed, resulting in a purer layer.
- Fine control of the thickness: By using quartz crystal microbalances (QCMs), one can control the thickness of the layer with nanometric precision.
- Compatibility with several substrates: When stoichiometric conditions are used, no annealing is required, opening the possibility of deposition on plastic foils or any other substrate sensitive to high temperatures. It is also

compatible with large area devices due to the homogeneity of the layers and the conformality.

- Intrinsicly additive: The absence of solvents allows the deposition of materials with similar polarities on top of each other without major chemical interactions, being one key property for the preparation of multilayer architectures such as tandem solar cells.

Vacuum deposition can be divided into different categories depending on the number of evaporation sources used and how they are employed:

- Single source vapor deposition: Using only one source is the simplest way of obtaining a compact layer of material. It is a widely extended technique for non-doped organic molecules, where the powder of the material is deposited in a crucible and heated until it starts subliming. It can also be used to prepare multicomponent materials such as the perovskites using a method called “flash evaporation”, where a mixture of the components is placed together in the same crucible.<sup>46-48</sup> The temperature increase is very intense and fast to avoid compositional gradients due to the differences in the sublimation temperature of each component. This is achieved by using an aluminum boat to ensure a fast energy transfer to all the materials. The components can be found either in fine powder (prepared, for example, by ball milling) or in a previously deposited thin film with the desired composition. This method leads easily to partially degraded films.
- Multi-source vapor deposition: A multicomponent material with a controlled composition can also be achieved with more than one evaporation source. Multi-source vapor deposition can be divided into two categories, co-evaporation, and sequential deposition. In the former, two or more evaporation sources are used at the same time, controlling with QCMs the amount of material deposited from each source. This is used mainly to obtain doped organic layers, subliming the molecule and the dopant at the same time, and for perovskites, subliming each of its components at precisely controlled rates. For example, for  $\text{CH}_3\text{NH}_3\text{PbI}_3$ , one would sublime in one crucible  $\text{CH}_3\text{NH}_3\text{I}$  and in another crucible  $\text{PbI}_2$ , in a 1:1 ratio. It is also possible to form the layer by sequential deposition, where thin layers (less than 50 nm) of each component are alternated in a sandwich structure, and the diffusion is promoted with heat to achieve a homogenous and isotropic layer.

Coevaporation is the technique used all along this thesis to prepare the perovskite layer. The first use of this technique was in 2013 using  $\text{PbCl}_2$  and excess of  $\text{CH}_3\text{NH}_3\text{I}$  as precursors, leading to 15% power conversion efficiency with a mixed  $\text{CH}_3\text{NH}_3\text{PbI}_{3-x}\text{Cl}_x$  perovskite.<sup>49</sup> Also in 2013, our group adapted the method to deposit pure iodide  $\text{CH}_3\text{NH}_3\text{PbI}_3$  films.<sup>50</sup> In this thesis, we report the record efficiency for the pure iodide  $\text{CH}_3\text{NH}_3\text{PbI}_3$  perovskite, with more than 20% power conversion efficiency, which is shown in chapter 3.<sup>32</sup> In the experimental section, we will address the basic principles of this technique and along the thesis I will describe its advantages.

## 1.6 Main device architectures

Perovskite solar cells can be fabricated in 2 main configurations, planar and mesoporous. The mesoporous architecture was the main configuration, however later it was found that planar films could also be used due to the balanced electron and hole mobilities with long diffusion lengths in perovskite solar cells.<sup>33</sup> The first demonstration of a PSC reported by the group of Miyasaka was similar to a dye-sensitized solar cell (DSSC), where the traditional organometallic dye was replaced with the perovskite.<sup>20,51</sup> In the field of DSSC, it is vital to have the photoactive material infiltrated in a mesoporous scaffold in order to maximize the light absorption and facilitate the charge transport. In a planar configuration, the perovskite is sandwiched between materials with different conduction and valence band energies in order to extract one charge carrier to an external circuit while blocking the opposite, preventing the recombination and therefore a loss of electrical current. Depending on the deposition order, we can distinguish between P-i-N and N-i-P configurations, based on the material (P or N) through which the sunlight passes first.

P-i-N configuration for PSCs typically has a planar structure similar to the ones used in the organic solar cells field. The commonly used hole transport layers (HTLs) are polymers like poly(3,4-ethylenedioxythiophene) poly(styrenesulfonate) (PEDOT:PSS) or Poly[bis(4-phenyl)(2,4,6-trimethylphenyl)amine] (PTAA), organic molecules like ( $\text{N}^4,\text{N}^4,\text{N}^4'',\text{N}^4''$ -tetra([1,1'-biphenyl]-4-yl)-[1,1':4',1"-terphenyl]-4,4"-diamine (TaTm) and metal oxides such as NiO. For electron transport layers (ETLs), stand out the fullerene  $\text{C}_{60}$  and its derivatives.<sup>52-56</sup> This kind of structure is more likely to avoid extreme thermal processes, being compatible with flexible and sensitive

substrates. Also, it facilitates its implementation into perovskite/silicon tandems, as P-N is the dominant configuration in commercial silicon solar cells.

On the other hand, the N-i-P configuration is primarily used in a mesoporous architecture, reaching record efficiencies of more than 25%.<sup>57</sup> These devices normally use a combination of a compact and a mesoporous metal oxide layer, generally TiO<sub>2</sub> or SnO<sub>2</sub>, as ETL, and a thick doped organic molecule as HTL, generally spiro-OMeTAD (2,2',7,7'-tetrakis(N,N-di-p-methoxyphenylamine)-9,9'-spirobifluorene). Despite this, a planar configuration can also be fabricated with high power conversion efficiencies by using only a thin planar dense non-mesoporous TiO<sub>2</sub> or SnO<sub>2</sub> layer.

## 1.7 Metal oxides as transport layers

Charge transport layers are a fundamental part of a perovskite solar cell. As mentioned previously, the general structure in perovskite solar cells is either P-i-N or N-i-P. The P and N materials need to be fine-tuned to have a proper band alignment with the energy levels of the perovskite. For example, for a proper N material, its conduction band must be aligned with the conduction band of the perovskite, while its valence band must have an energy barrier that ensures a hole blocking character, being the opposite case for the P material.

On the one hand, organic molecules have the advantage of being chemically tunable, easily varying their HOMO (highest occupied molecular orbital) and LUMO (lowest unoccupied molecular orbital) levels. Other properties must also be accomplished, such as suitable charge transport, proper solubility if they are deposited by solution processes, chemical and photochemical stability, and charge carrier selectivity, among others. On the other hand, they should have low absorbance in the visible. This sometimes leads to a trade-off since charge transport requires conjugation, which implies increased absorption and a certain chemical instability.

Some metal oxides are excellent transporting materials with advantageous properties and a wide variety of alternatives for both P and N contacts (figure 7). They are chemically more robust than organic molecules, their large bandgap leads to minimal parasitic absorption, and they can be formed by a

wide range of possible deposition methods, such as atomic layer deposition (ALD) or spin coating using a nanoparticle dispersion, to name a few.

Transition metal oxides (TMOs) can also present relatively high charge carrier concentrations. As a result, they generally have an excellent ohmic contact with the common cathodes or anodes used in PSCs, providing efficient charge injection. Nowadays, transition metal oxides are heavily utilized in many optoelectronic devices such as OLEDs,<sup>58</sup> organic photovoltaics (OPV),<sup>59–64</sup> and OFETs,<sup>65–71</sup> and they are essential components of many high-efficiency perovskite solar cells reported in the literature.<sup>72,73</sup>

One key feature of metal oxides is self-doping. Hypothetically, a perfectly stoichiometric semiconducting metal oxide would have the Fermi level in the middle of the bandgap, but an oxide usually has defects due to its higher entropy. The typical defects in metal oxides are oxygen or metal vacancies, giving rise to undercoordinated or over coordinated metal centers, leading to new occupied or unoccupied states near the conduction band or valence-band edges. These defect states make an oxide behave as either a P or N-type semiconductor.

The wide variety of work functions make them very versatile for device applications, spanning from extremely low for defective  $ZrO_2$  (3.5 eV) to extremely high for stoichiometric  $V_2O_5$  (7.0 eV).<sup>74</sup> High work function metal oxides are used as hole injection materials, with  $NiO$ ,  $V_2O_5$ , and  $MoO_3$  examples of oxides used as HTLs in perovskite solar cells, whereas low work function metal oxides such as  $TiO_2$ ,  $ZnO$  or  $SnO_2$  are used as electron injection materials.

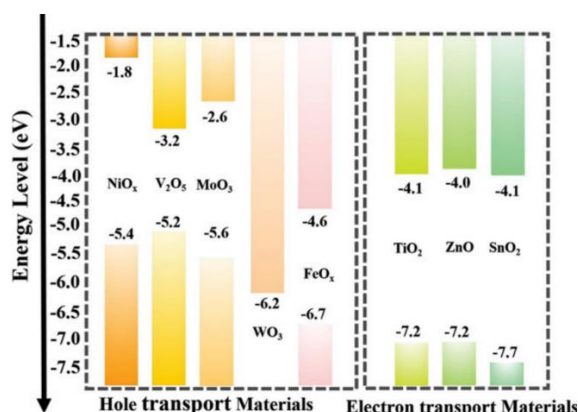


**Figure 7:** Valence and conduction bands of different metal oxides used as transport layers in perovskite solar cells. Image from reference 71.

## 1.8 Aim of the thesis

This thesis aims to improve vacuum deposited perovskite solar cells, enhancing the stability and performance of the devices. To fulfill this objective, we explore the substitution of the weakest part of the device, the doped transport layers, by implementing the use of transition metal oxides. The thesis is structured as follows:

-**Chapter 3:** Substitution of doped C<sub>60</sub> in N-i-P vacuum deposited perovskite solar cells by a TiO<sub>2</sub> nanoparticle dispersion, leading to devices with higher efficiencies and better reproducibility.

-**Chapter 4:** Substitution of doped TaTm in P-i-N vacuum deposited perovskite solar cells by MoO<sub>3</sub> and then the implementation of this layer in the N-i-P configuration, leading to a design with metal oxides on both contacts.

-**Chapter 5:** Characterization of the P-i-N architecture with MoO<sub>3</sub> from chapter 4 under space conditions, which was proven to be very stable and opened the possibility of using perovskite solar cells in high altitude conditions.

The substitution of the doped transport layers led to devices with higher power conversion efficiencies (more than 20%, among the highest values for vacuum deposited CH<sub>3</sub>NH<sub>3</sub>PbI<sub>3</sub> solar cells to date) and more robustness, passing stability tests under space conditions. The work developed in this thesis has opened an interesting field for vacuum deposited perovskite solar cells and changed the main fabrication routes in our laboratory.

## **Chapter 2**

### **Experimental and methods**

*"Extraordinary claims require extraordinary evidence."*

Carl Sagan



## 2. Experimental and methods

The experimental work carried out in this thesis follows the scientific method, building a hypothesis and testing it experimentally to reach the conclusions described in the following chapters. Different fabrication and characterization tasks were necessary to test the proposed hypotheses, following the standard procedures established by the scientific knowledge in the perovskite solar cell field. Most of the work was performed in a class 10000 cleanroom to reduce the presence of dust particles, which is fundamental in view of the very thin film ( $<1\text{ }\mu\text{m}$ ) fabrication. Moreover, almost every fabrication process was done in an inert environment inside a  $\text{N}_2$ -filled glovebox to avoid the degradation of the materials due to oxygen and moisture.

In this chapter, we first describe the materials used to fabricate the solar cells, specifying their role in the device structure. Then, we describe the fabrication process of the perovskite layer and the P-i-N and N-i-P device stacks. To conclude, we report the different characterization techniques for the individual thin films that compose the devices and also the device characterization as a whole, focusing on the electrical properties.

### 2.1 Materials for solar cell fabrication

In the following section, we describe the materials used to prepare a standard perovskite solar cell used in this work. The solar cells are built in a bottom-top architecture starting from a commercial glass substrate of  $3\times 3\text{ cm}$  with a patterned transparent conductive oxide (TCO) on top. The TCO used in this work is indium tin oxide (ITO), deposited by sputtering, with a sheet resistance of  $13\text{--}20\text{ }\Omega\cdot\text{sq}$  and optical transmittance in the visible range higher than 80%. Prior to any other step, those substrates were cleaned following a standard procedure using soap, miliQ water, and ethanol supported with sonication steps and finished with a  $\text{UV-O}_3$  treatment to remove organic contamination. For the charge carrier transport and injection/extraction, the materials used are: 2,2'-(Perfluoronaphthalene2,6-diylidene)dimalononitrile ( $\text{F}_6\text{-TCNNQ}$ ),  $\text{N}_4,\text{N}_4,\text{N}_4'',\text{N}_4''$ -tetra([1,1'-biphenyl]-4-yl)[1,1':4',1"-terphenyl]-4,4"-diamine ( $\text{TaTm}$ ) and  $\text{N}_1,\text{N}_4$ -bis(tri-ptolylphosphoranyli-dene)benzene-1,4-diamine ( $\text{PhIm}$ ), provided by Novaled GmbH.  $\text{TaTm}$  is the HTL used to transport the holes and block the electrons,  $\text{F}_6\text{-TCNNQ}$  is the dopant used in combination

with TaTm to allow an ohmic contact with the electrodes, and PhIm is the dopant of the ETL for the same purpose. Fullerene C<sub>60</sub> was purchased from Sigma Aldrich and 2,9-Dimethyl-4,7-diphenyl-1,10-phenanthroline (BCP) along with Molybdenum oxide (MoO<sub>3</sub>) from Lumtec. C<sub>60</sub> is used as the ETL to transport electrons and block holes, BCP is used as the injection layer for electrons in substitution of doped C<sub>60</sub> and MoO<sub>3</sub> is used as the injection layer for holes in substitution of doped TaTm. The chemical structures of the organic molecules are depicted in figure 8. Finally, a titanium oxide (TiO<sub>2</sub>) nanoparticle dispersion was provided by our collaborator Dr. Hadipour from IMEC (Interuniversity Microelectronics Centre) and a tin oxide (SnO<sub>2</sub>) nanoparticle dispersion was bought from Alpha Aesar. Both were used as electron injection layers in substitution of doped C<sub>60</sub>. For the perovskite fabrication, the materials used are lead (II) iodide (PbI<sub>2</sub>), purchased from Tokyo Chemical Industry CO (TCI), and methylammonium iodide (CH<sub>3</sub>NH<sub>3</sub>I, MAI) from Lumtec.

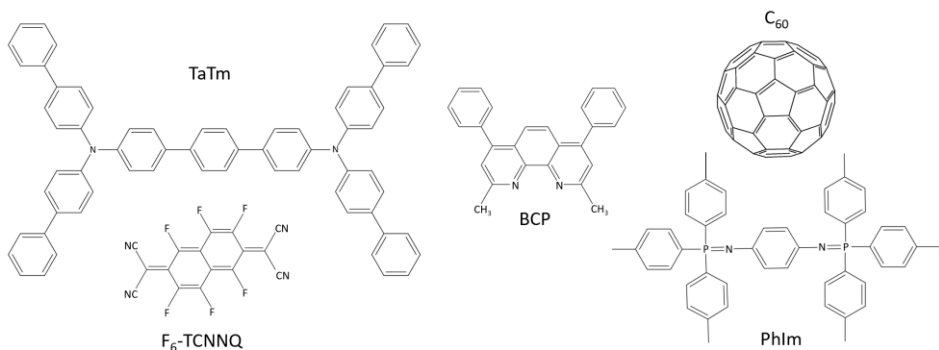


**Figure 8:** Chemical structures of the molecules TaTm, F<sub>6</sub>-TCNNQ, BCP, C<sub>60</sub> and PhIm.

## 2.2 Fabrication of CH<sub>3</sub>NH<sub>3</sub>PbI<sub>3</sub> perovskite

As mentioned before, there are two possible architectures for a solar cell, P-i-N and N-i-P, depending on the deposition sequence, always starting from the glass/ITO side. There are significant differences between both structures, which are addressed below, both having in common the perovskite absorber.

The MAPI perovskite is prepared by coevaporation of two precursors: PbI<sub>2</sub> and CH<sub>3</sub>NH<sub>3</sub>I in a high vacuum chamber equipped with a turbomolecular pump (Pfeiffer TMH 261P, DN 100 ISO-K, 3P) coupled to a scroll pump (figure 9). The vacuum chamber is integrated into a nitrogen-filled glovebox and contains six temperature-controlled evaporation sources (Creaphys) fitted with ceramic

crucibles. Each source is dedicated to a different type of material to avoid contamination. The sources are directed upwards with an angle of 90° with respect to the chamber base, and the distance between the substrate holder and the evaporation sources is approximately 20 cm. Three quartz crystal microbalance (QCM) sensors are used to monitor the deposition rate of the materials from each thermal source ( $\text{PbI}_2$  and  $\text{CH}_3\text{NH}_3\text{I}$  in this case), and a third one closer to the substrate holder monitoring the total deposition rate, allowing nanometric precision. The perovskite evaporation was carried out at a pressure of approximately  $10^{-6}$  mbar.

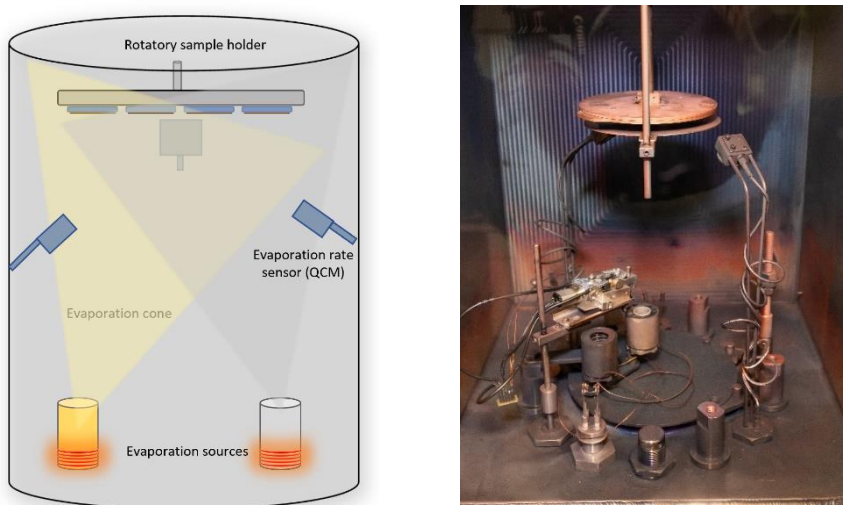


**Figure 9:** Basic schematic of the evaporation chamber and real picture of a similar chamber.

All the sublimed materials must be calibrated with their specific sensor in order to have a correct reading of the deposited thickness. This process is only required for the first time and is repeated after several months of evaporation to verify it is still correct. The calibration for the perovskite precursors,  $\text{PbI}_2$  and MAI ( $\text{CH}_3\text{NH}_3\text{I}$ ), includes the following steps: setting the material density in the QCM readers ( $6.16$  and  $2.22 \text{ g/cm}^3$ , respectively), depositing a layer of an established thickness and measuring it in a profilometer to correct the value by using a tooling factor. Repeating this process 3-4 times is enough to have a proper reading of the thickness. For MAI, the process was similar, but it was necessary to evaporate silver on top to protect the film from moisture when measuring it in the profilometer.

Once both materials are calibrated, coevaporation can be carried out. The powder of the materials is deposited into ceramic crucibles and heated inside the Creaphys sources. MAI was set to a temperature of approximately 80°C and  $\text{PbI}_2$  to 260°C. The evaporation rate of MAI was kept constant at 1 Å/s and the  $\text{PbI}_2$  rate was adjusted in order to have stoichiometric conditions with a small excess of  $\text{PbI}_2$ , which is beneficial according to literature.<sup>75</sup> The resulting film composition and crystallinity were confirmed by using X-ray diffraction and absorbance measurements, which are discussed in section 2.5. Generally, the thickness of the perovskite is around 600 nm in order to maximize light absorption while ensuring a proper charge transport.

## 2.3 Fabrication of a P-i-N solar cell

The general structure for a P-i-N solar cell is, from the bottom (substrate) to the top (metal contact): Glass / ITO / HTL / Perovskite / ETL / Ag (figure 10). In order to extract the holes and block the electrons, the HTL used is at least a 10 nm layer of TaTm. For the opposite purpose, as ETL is used a 25 nm layer of fullerene  $C_{60}$ . The  $C_{60}$  layer can be thicker due to its better electron mobility, which can be used to compensate the potential roughness of the perovskite layer. Beyond the charge selectivity of the materials in contact with the perovskite, injecting or extracting carriers into the TCO and metal contacts minimizes the losses when an ohmic contact is formed. A thicker doped version of each material previously described was used: TaTm doped with F<sub>6</sub>-TCNNQ and  $C_{60}$  doped with PhIm. The doping is achieved by coevaporation of the dopant, following the exact same procedure described for the perovskite, with small modifications. In this case, it is important considering the cross-reading between the rate sensors. During the coevaporation, the dopant sensor may read not only the dopant evaporation rate, but also partly the organic molecule that is being evaporated at the same time in another source. This happens due to the small size of the evaporation chamber and the big difference between the amount of organic molecule and dopant. To correct this parasitic reading we first set the organic molecule rate to 0.8 Å/s and check the reading in the dopant sensor. Although it should be 0, generally there is a certain X value. Then, we start the evaporation of the dopant until its sensor reaches this X value plus a pre-calculated amount that depends on the desired doping concentration. In this thesis, the goal was to replace these doped layers due to their chemical instability and reduced optical transmittance. For the P-i-N architecture, the doped TaTm was replaced by

$\text{MoO}_3$ , which has a deep conduction band that ensures a proper hole extraction.  $\text{MoO}_3$  requires a post-deposition annealing step in  $\text{N}_2$  in order to have the desired transport conditions by the formation of sub-gap charge states. It was also found that substituting the doped  $\text{C}_{60}$  layer with a single layer of BCP improves the stability and general performance of the device.<sup>76</sup> Thus, I will be using this standard P-i-N solar cell structure: Glass / ITO /  $\text{MoO}_3$  (7 nm) / TaTm (10 nm) /  $\text{CH}_3\text{NH}_3\text{PbI}_3$  (600 nm) /  $\text{C}_{60}$  (25 nm) / BCP (7 nm) / Ag (100 nm).

$\text{MoO}_3$  was sublimed in a different vacuum chamber following a similar procedure, but instead of using Creaphys sources, the heating was achieved by applying a high current input, around 4 A, through a metal boat (generally tungsten, tantalum or molybdenum). TaTm and  $\text{C}_{60}$  were sublimed at a rate of 0.5 Å/s, with temperatures of approximately 300 °C and 400 °C, respectively. BCP was sublimed at a rate of 0.3 Å/s and a temperature of 150 °C. Finally, 100 nm of silver are evaporated as the top electrode in the same vacuum chamber as  $\text{MoO}_3$ .

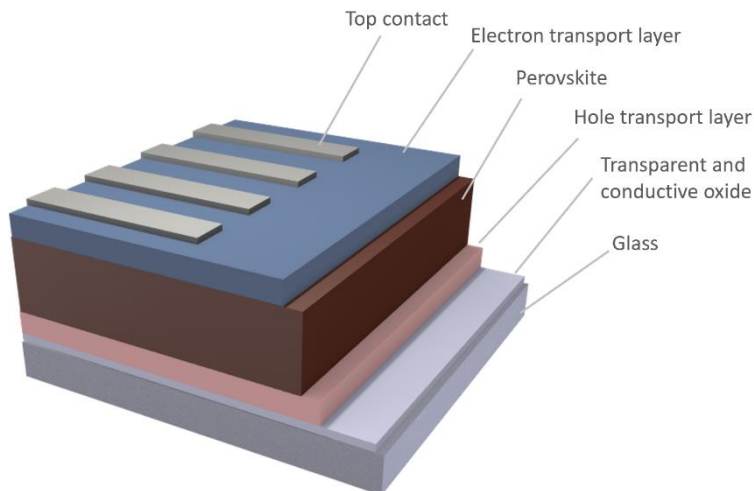


**Figure 10:** Schematic of the P-i-N structure (not to scale)

## 2.4 Fabrication of an N-i-P solar cell

The general structure for an N-i-P solar cell is symmetrical to the one previously described, being: Glass / ITO / ETL / Perovskite / HTL / Au. In this case, the materials used as HTL and ETL are the same as in P-i-N, TaTm and C<sub>60</sub>, but the thickness of C<sub>60</sub> is reduced to 10 nm in order to reduce parasitic light absorption. The injection layers are different than in the P-i-N case. As an electron injection layer, we implemented the use of nanoparticles dispersed in ethanol deposited by spin coating. First, a TiO<sub>2</sub> nanoparticle dispersion prepared by a collaborator in IMEC was used, and later I switched to a commercial one of SnO<sub>2</sub>. The SnO<sub>2</sub> dispersion was diluted in miliQ water to a final concentration of 5% and deposited on top of a Glass/ITO substrate in air. Then it was dried by spinning it at 3000 RPM for 30 s, forming a compact layer of around 30 nm. The layer was annealed on a hot plate in air at 150 °C for 30 min to remove the solvent excess and fully oxidize it. For TiO<sub>2</sub>, the procedure is the same, except for the dilution part, as it was not required. For hole injection, the doped TaTm was maintained in chapter 3 and then substituted by 1 nm of 2,2',2''-(1,3,5-Benzenetriyl)-tris(1-phenyl-1-H-benzimidazole) (TPBi) and 7 nm of MoO<sub>3</sub> in chapter 4. Finally, as top contact was used 100 nm of gold, that was evaporated in the same vacuum chamber as MoO<sub>3</sub> and Ag. Thus, the standard N-i-P configuration I used is: Glass / ITO / SnO<sub>2</sub> (30 nm) / C<sub>60</sub> (10 nm) / CH<sub>3</sub>NH<sub>3</sub>PbI<sub>3</sub> (600 nm) / TaTm (10 nm) / TPBi (1 nm) / MoO<sub>3</sub> (7 nm) / Au (100 nm).

All the evaporation conditions are the same as in the P-i-N configuration. In this case, MoO<sub>3</sub> does not require annealing due to the interaction with the TPBi layer, explained in chapter 4. This layer is evaporated similarly as the other molecules but at a slower rate, around 0.2 Å/s at a temperature of 170 °C.

## 2.5 Thin-film characterization

The layer thicknesses were measured using a mechanical profilometer (Ambios XP-1). This measurement was particularly important for each material's individual calibration. X-ray diffraction (XRD) patterns were collected at room temperature on an Empyrean PANalytical powder diffractometer using the Cu K $\alpha$ 1 radiation. This measurement gives information about the crystallinity of the perovskite film, including the presence of secondary phases (e.g. PbI<sub>2</sub>), the exact crystal structure (e.g., cubic vs tetragonal MAPI), the average grain size, or the crystalline orientation. Absorbance spectra were obtained using a fiber optics based Avantes Avaspect 2048 spectrometer. Absorbance can give useful information on the bandgap energy, Urbach energy and the general quality of the perovskite film. Also, doped layers' doping concentration can be inferred from the absorbance spectra. Scanning Electron Microscopy (SEM) images were collected on a Hitachi S-4800 microscope operating at an accelerating voltage of 2 kV over samples metallized with platinum. SEM images give useful information about the grain size of the perovskite and overall surface morphology.

## 2.6 Solar cell characterization

In this section, the basic characterization techniques for a solar cell will be described, which give information about the diode quality and the solar cell power conversion efficiency. We will divide the characterization into 2 sections: External quantum efficiency and current density versus voltage curve, in dark conditions and under illumination.

External quantum efficiency (EQE):

The external quantum efficiency, also named incident photon to current efficiency (IPCE), is the ratio between photons that reach the device of a given energy and the extracted charge carrier pairs, plotted as a function of the photon wavelength (figure 11). In an ideal case without parasitic light absorption, without charge carrier recombination or any other possible losses, each photon with energy equal to or higher than the material's bandgap will generate one electron/hole pair. However, that is not the case in real

conditions. That is why this measurement can be key to determine the quality of the solar cell at each wavelength in terms of charge carrier generation, charge carrier extraction, parasitic absorption, reflection losses, and charge carrier recombination, among others. The EQE is estimated by measuring the cell response at different wavelengths using a white halogen lamp in combination with band-pass filters and a MiniSun simulator made by the Energy Research Center of the Netherlands (ECN). The spectrum mismatch from the lamp and the real sun spectrum at sea level are corrected using a calibrated Silicon reference cell.

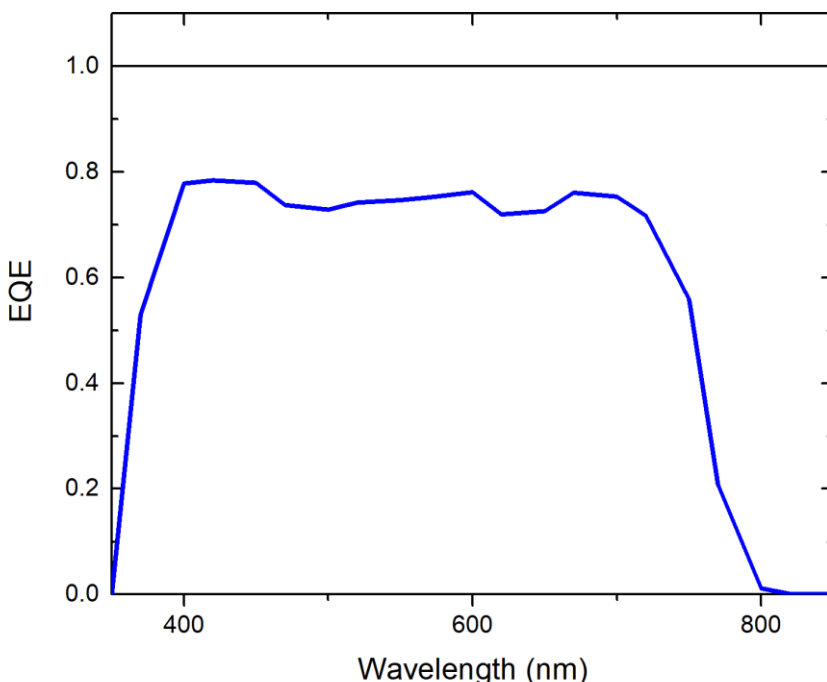


**Figure 11:** EQE measurement of a MAPI perovskite solar cell.

Current density-voltage (J-V) curve:

Perovskite solar cells electrical behaviour is based on a diode, which can be modelized with the circuit in figure 12. Their quality depends on different parameters:

- The leakage current: a residual current typically coming from undesired imperfections and defects in the diode. Its magnitude is determined by the shunt resistance ( $R_{SH}$ ). Low shunt resistance causes power losses in solar cells by providing an alternate current path for the light-generated current. In

particular, it reduces the photocurrent flowing through the solar cell and reduces the photovoltage.

- Series resistance: the series resistance ( $R_s$ ) is one of the loss mechanisms limiting the performance of a solar cell, which arises from the resistance within the device itself. It is a parasitic effect coming from the resistance of the absorber, the transport materials, the metal contacts, and the metal connections on the device. The main impact of series resistance is a reduction of the fill factor, although very high values may also reduce the short-circuit current.

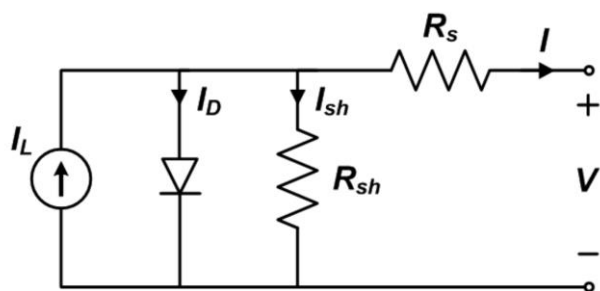


**Figure 12:** Simplified equivalent circuit model of a solar cell (diode).

A J-V curve is based on applying a voltage bias sweep and measuring the current flowing through the device. In an ideal diode, the current can only flow in one direction (referred to as forward voltage), therefore in dark conditions, in an ideal case the current density is negligible until applying a forward voltage higher than a threshold value defined by the device characteristics. Representing the J-V curve in semilogarithmic scale gives a better insight into the parameters previously described (figure 13). At reverse and low forward voltages, the J-V curve is ohmic, and this regime is dominated by the leakage current, and hence, by the magnitude of the shunt resistance. For lower shunt resistances, higher leakage currents will be observed. As mentioned before, this part of the curve contains information about the defect density and diode quality in general. The second regime is dominated by the diffusion current; hence, it is called the diffusion regime. The diffusion current arises from the non-uniform concentration of charged particles in a semiconductor. This regime gives indications about the electron/hole transport through the device, as well as about the electron/hole recombination. Finally, at higher applied voltages, the drift current starts to dominate the J-V curve. This current comes from the motion of charge carriers under an electric field, and the deviation

from the diffusion to the drift regime identifies the built-in potential. The drift current can be limited by the injection at the contact or by the transport within the active materials.

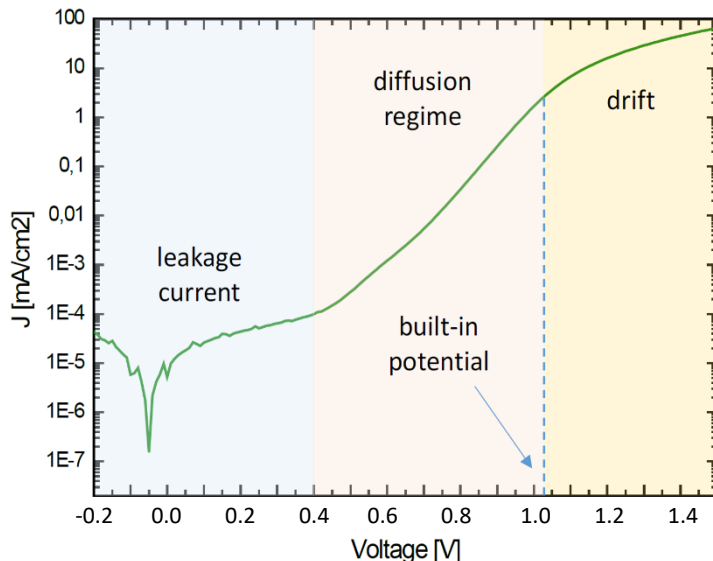


**Figure 13:** J-V curve under dark conditions of a perovskite solar cell in semilogarithmic scale.

When this measurement is performed under illumination, we call it an illuminated J-V curve. The measurement concept is similar to the dark curve but with an additional source of photogenerated current. This measurement is key to determine the solar cell power generation, as well as the quality of the device. Several parameters can be obtained from the illuminated J-V curve (all depicted in figure 14):

- Short-circuit current density ( $J_{sc}$ ): It is the current flowing through the solar cell under illumination when the applied voltage is zero. This current is generated in the photoactive material by the absorbed photons. In the absence of resistance losses, it is the largest current that may be extracted from the solar cell. It depends on several factors, such as the area of the solar cell, the photon flux, the absorption spectrum of the material and its ability to separate and extract charge carriers. Its value is usually given normalized to the effective area, in  $\text{mA}/\text{cm}^2$ .

-Open-circuit voltage ( $V_{oc}$ ): It is the maximum voltage available from a solar cell when the net current through the device is zero. It is limited by the band gap of the absorber and, in some cases, by the energetics of the transporting layers, and it is strongly influenced by the charge carrier recombination.

-Maximum power point (MPP): It is the point in the J-V curve where the product of the voltage and the current is maximum,  $P_{max} = (J \cdot V)_{max}$ . The values of current and voltage at the MPP, also defined as  $J_{MPP}$  and  $V_{MPP}$ , are always lower than  $J_{sc}$  and  $V_{oc}$ .

-Fill factor (FF): It is a parameter obtained from the ratio between the maximum power obtained from the solar cell ( $P_{max}$ ) and the product of  $V_{oc}$  and  $J_{sc}$ . Graphically, it is a measure of the “squareness” of the graph. This parameter gives information about the efficiency of the charge extraction within the device, the resistance of the device and the recombination of the charge carriers.

$$FF = \frac{V_{MPP} \cdot J_{MPP}}{V_{oc} \cdot J_{sc}} = \frac{\text{Real area (A)}}{\text{Ideal area (B)}}$$

-Power conversion efficiency (PCE): It is defined as the ratio of energy output from the solar cell to input energy at specific illumination conditions. Generally, a reference illumination intensity for Earth applications is the solar spectrum considering different atmospheric and geometric conditions representative to real photovoltaic applications. This standard spectrum is called AM1.5G and its power density is equal to 97 mW/cm<sup>2</sup> but has been normalized to 100 due to the convenience of the round number and the fact that there are inherent variations in incident solar radiation. Consequently, the power conversion efficiency formula for an AM1.5G light spectrum is:

$$PCE = \frac{J_{sc} \cdot V_{oc} \cdot FF}{100 \text{ mW/cm}^2}$$

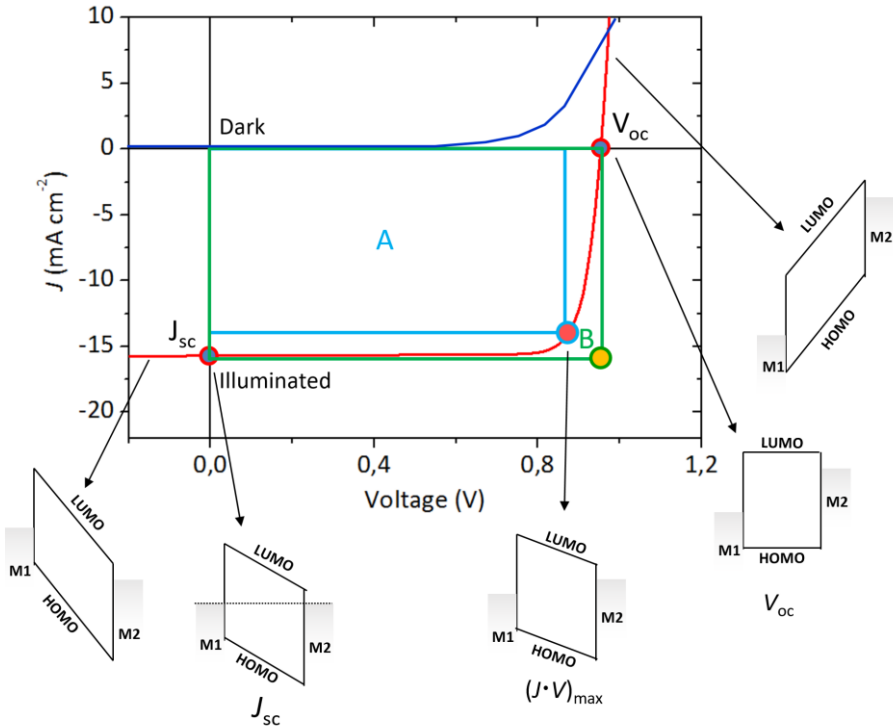


**Figure 14:** J-V curves in dark (blue) and under illumination (red) highlighting the  $V_{oc}$ ,  $J_{sc}$  and maximum power points, with common simplified band diagrams for each working regime.

Figure 14 depicts a standard J-V curve under illumination in linear scale along with simplified band diagrams (assuming that there is no doping at the interfaces and therefore no band bending). At short-circuit ( $V = 0$ , when the Fermi levels of the external contacts M1 and M2 are aligned in steady state), electrons are extracted through M2 and holes through M1. When the product of current and voltage is maximum,  $(J \cdot V)_{max}$ , the maximum power is obtained. At the open circuit voltage point, the bands are approximately aligned and there is no electric field to extract electrons and holes which consequently recombine (current is zero). At voltages higher than the  $V_{oc}$ , electrons and holes are injected into the device instead of being extracted (positive current) in the same way as in the dark J-V measurement.

The current density-voltage characteristics of this thesis were obtained using a Keithley 2400 source-measure unit under white light illumination. For the measurements in this work, two kinds of lamps were used, a tungsten and a xenon lamp, for different purposes explained in the corresponding chapters. Both were calibrated using a silicon reference cell equipped with an infrared cut-off filter (KG-3, Schott). For the measurements performed with the tungsten lamp the short circuit current density was corrected considering the device EQE. The measurements done with a Xe lamp were performed in air using appropriate filters, leading to an AM1.5G emission spectrum. The combination of filters and the xenon lamp are referred to as a solar simulator. The J-V curves were recorded between -0.2 and 1.2 V with 0.01 V steps, integrating the signal for 20 ms after a 10 ms delay. This corresponds to a speed of about  $0.3 \text{ V s}^{-1}$ . The layouts used to test the solar cells have four equal areas of  $0.04 \text{ cm}^2$ , (defined as the overlap between the ITO and the top metal contact) or 16 equal areas of  $0.0825 \text{ cm}^2$  and were measured through a shadow mask with  $0.01 \text{ cm}^2$  and  $0.05 \text{ cm}^2$  aperture, respectively (figure 15).

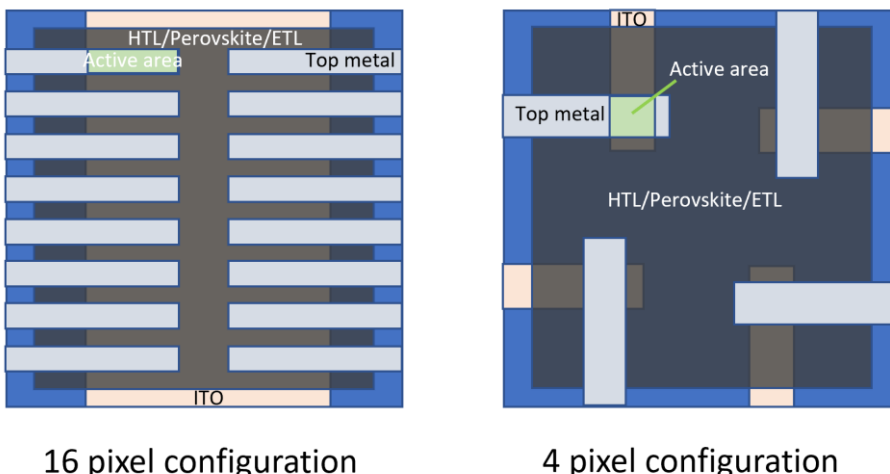


**Figure 15:** Solar cell layouts employed in this thesis (not to scale). ITO and top metal are the bottom and top contacts, respectively.



# **Chapter 3:**

## **Interfacial Modification for High-Efficiency Vapor-Phase-Deposited Perovskite Solar Cells Based on a Metal Oxide Buffer Layer**

*“Somewhere, something incredible is waiting to be known.”*

Carl Sagan



### 3. Interfacial Modification for High-Efficiency Vapor-Phase-Deposited Perovskite Solar Cells Based on a Metal Oxide Buffer Layer

In this chapter, the target was the implementation of a metal oxide as electron extraction layer in high-efficiency vacuum-deposited perovskite solar cells. Doped organic layers were the dominant extraction materials in vacuum-deposited PSCs, leading to high PCEs despite their stability, cost and parasitic absorption issues. However, functional layers based on metal oxides, widespread in the solution-process perovskite devices, do not allow a direct implementation in vacuum-deposited devices. We developed a novel way to ensure a proper passivation of the metal oxide's surface states while maintaining an adequate substrate for the perovskite growth, leading to PCEs higher than 20% and  $V_{oc}$ s of more than 1.15 V for a 1.55 eV absorber bandgap.

#### 3.1 Introduction

The use of metal oxides as transport layers is widely extended in the perovskite photovoltaic field due to their suitable properties such as low parasitic absorption, high electron and hole mobilities, long term stability and ease of deposition. Furthermore, metal oxides act not only as charge transport layers, but also ensure a proper injection/extraction of charge carriers due to their self-doping, arising from defects in the lattice (oxygen and metal vacancies, for example). For these reasons, most of the record perovskite solar cells employ a combination of mesoporous and planar  $TiO_2$  as electron transport layers, leading to efficiencies as high as 25%.<sup>57</sup> These works, however, are focused on solution-processed perovskites, where the solution is infiltrated into the pores of the  $TiO_2$  layer.  $TiO_2$  and  $SnO_2$  are currently the ETLs of choice for the best performing devices in the perovskite field. Their adequate energy levels allow a proper band alignment with the perovskite, as the conduction band minimum (CBM) energy is suitable to collect electrons and inject/extract them, and the valence band maximum (VBM) is deep enough to block holes, as depicted in figure 16.

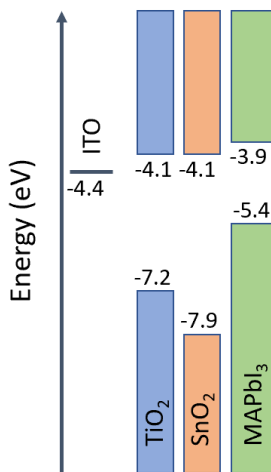


**Figure 16:** Energy levels of TiO<sub>2</sub>, SnO<sub>2</sub> and MAPI perovskite.

These metal oxides also display high electron mobilities, which can contribute to mitigate the charge accumulation at the perovskite interface,<sup>77</sup> and have a wide bandgap (>3 eV), resulting in adequate transmittances when employed in an N-i-P configuration. Apart from that, both can be deposited with a wide variety of methods, such as spray pyrolysis,<sup>78</sup> thermal oxidation,<sup>79</sup> atomic layer deposition,<sup>80</sup> spin coating and electrochemical deposition,<sup>81</sup> among others.

As it was already said, perovskite vacuum deposition is a competitive process which presents significant advantages with respect to other techniques. It was used to fabricate solar cells with power conversion efficiencies higher than 20%,<sup>82</sup> rivalling the solution-processed records at that time. The use of doped organic materials as injection/extraction layers sandwiching the perovskite has typically been a common trait of highly efficient vacuum deposited perovskite solar cells, as well as one of the main characteristics of this record stack. Organic doped layers are excellent charge transporting materials, as they can form ohmic contacts with the electrodes and present good electron and hole mobilities along with a reduced series resistance.<sup>83</sup> On the other hand, they induce parasitic absorption and a certain chemical instability.<sup>84</sup>

In contrast, using the excellent potential of metal oxides as transporting materials with vacuum deposited perovskites has been elusive. Only a few reports exist in which the sublimed perovskites were evaluated. Olthof et al. found a PbI<sub>2</sub>-enriched interface with the metal oxide which they attributed to

a low sticking coefficient of MAI, which would lead to an energy barrier hindering the charge transport.<sup>85</sup> Adding a self-assembled monolayer helped to prevent this interfacial substoichiometry. In these studies, however, no photovoltaic devices were prepared from the perovskite films, which leaves unanswered questions on the effect of these findings on device performance.<sup>86</sup> Also, direct use of conventional mesoporous metal oxide layers requires a high temperature annealing step (>400 °C) which excludes the use of flexible polymer substrates. In order to maintain the characteristic advantages of vacuum deposited perovskites, such as the growth of very efficient annealing-free conformal thin-films onto substrates with different morphologies, low temperature processed metal oxide layers need to be employed.

Here, I demonstrate that it is possible to replace the organic doped N layer, commonly used at that time in the record vacuum deposited MAPI solar cells, with a compact film of TiO<sub>2</sub> nanoparticles processed at low temperature. This increases the overall performance of the device. A thin C<sub>60</sub> interlayer was deposited between the metal oxide and the perovskite to passivate the surface traps and promote a stoichiometric growth of the perovskite. The reduction of parasitic absorption and recombination rates allowed the use of a perovskite thickness of almost 1 μm. This enabled a PCE of more than 20%, the highest obtained value for a vacuum-deposited MAPI perovskite solar cell at that time.

### 3.2 Experimental and methodology

In this work I optimized a low-temperature (100 °C) deposition of TiO<sub>2</sub> using a nanoparticle dispersion deposited by spin coating. The rest of the layers were kept the same to compare the results obtained with the fully evaporated stack from reference 82. The architecture of the devices in this section consists in an N-i-P planar structure with the following configuration: ITO / TiO<sub>2</sub> (30 nm) / CH<sub>3</sub>NH<sub>3</sub>PbI<sub>3</sub> (500-600 nm) / TaTm (10 nm) / TaTm:F<sub>6</sub>-TCNNQ (40 nm)/ Au (100 nm).

In this architecture, TiO<sub>2</sub> acts as electron transport layer, the perovskite is the photoactive material, TaTm acts as electron blocking and hole transport layer and TaTM: F<sub>6</sub>-TCNNQ is a doped layer acting as hole injection layer.

All the materials except ITO and  $\text{TiO}_2$  were deposited via vacuum deposition. More detailed information about the materials and deposition techniques can be found in chapter 2 and in the complete publication, available at the end of the chapter.

### 3.3 Results and discussion

The initial analysis of the devices with this configuration revealed a rather poor performance, with all the solar cell parameters lower than expected, leading to PCEs of less than 10% (figure 17, a). We attributed this to an interfacial problem due to a poor formation of the perovskite on top of  $\text{TiO}_2$ . As previously mentioned, other works have shown that the MAI sticking coefficient on metal oxides is poor, which results in an energy barrier near the interface due to the insulating character of  $\text{PbI}_2$ .<sup>85</sup> This, along with the high surface recombination in the metal oxide trap states leads to a decrease in all the PV parameters. Therefore, considering the optimal perovskite co-sublimation on fullerene derivatives films,<sup>82</sup> we incorporated a 10 nm-thick  $\text{C}_{60}$  interlayer between the  $\text{TiO}_2$  and the perovskite. This led to a drastic improvement of all photovoltaic parameters (Table 1). In figure 17 are depicted the J-V curves of the solar cells in these two configurations, without (a) and with  $\text{C}_{60}$  (b), showing the latter higher  $V_{oc}$ ,  $J_{sc}$  and FF values as a consequence of a better charge transport and reduced recombination.

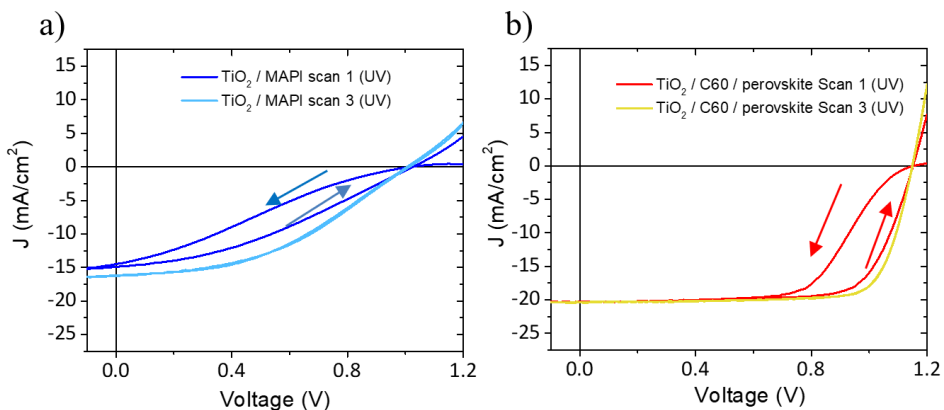


**Figure 17:** J-V curves of N-i-P solar cells using  $\text{TiO}_2$  with (b) and without (a)  $\text{C}_{60}$  interlayer measured under a xenon lamp. Arrows indicate scan direction (negative to positive voltage bias and vice-versa).

Interestingly, all the devices presented an activation process characterized by a continuous improvement of FF (all analyzed samples) and  $J_{sc}$  (samples without  $C_{60}$  interlayer) after subsequent scans. This process was accelerated when the solar cells were measured using a xenon lamp, due to a small UV component present in its spectrum. Kelvin probe and impedance spectroscopy measurements, both described in the complete publication after this section, evidenced the improvement of the band alignment between the  $TiO_2$  and the perovskite upon UV exposure. This change in the metal oxide work function is attributed to the accelerated defect filling on the  $TiO_2$ , photoactive in the UV region.

**Table 1:** Solar cell parameters under full solar spectrum illumination. The measurements were performed first in reverse (from positive to negative bias) and immediately afterwards in forward direction (from negative to positive bias).

Sample	Scan number (direction)	$V_{oc}$ (V)	$J_{sc}$ (mA/cm <sup>2</sup> )	FF (%)	PCE (%)
$TiO_2$	Scan 1 (Reverse)	1.02	14.47	24.5	4
	Scan 1 (Forward)	1.03	14.92	35.1	5
	Scan 3 (Reverse)	1.01	16.30	42.2	7
	Scan 3 (Forward)	1.00	16.18	42.2	7
$TiO_2/C_{60}$	Scan 1 (Reverse)	1.15	20.40	54.6	13
	Scan 1 (Forward)	1.15	20.35	71.1	17
	Scan 3 (Reverse)	1.15	20.54	76.1	18
	Scan 3 (Forward)	1.15	20.55	76.3	18

Similar UV activation phenomena in  $TiO_2$ -based devices has been previously described, especially in the organic photovoltaics field, with interpretations related to adsorbed molecular oxygen or shallow charge carrier traps that are filled upon UV illumination.<sup>87</sup> Other works in the perovskite field associate a similar activation process to ion migration, in particular to the accumulation of  $MA^+$  cations at the fullerene/perovskite interface which reduces its energy disorder and enhances the  $V_{oc}$ .<sup>88</sup>

The solar cells using  $\text{TiO}_2/\text{C}_{60}$  as electron selective contact displayed efficiencies between 18 and 19%, with a better reproducibility and less data spreading compared with the configuration with doped  $\text{C}_{60}$  (figure 18, left). The record  $V_{\text{oc}}$  was 1.17 V, with less than 400 mV deficit with the absorber band gap, and only 119 mV lower than the highest achievable value according to the Shockley-Queisser limit.<sup>89</sup> These high voltage values imply low recombination rates, both at the interfaces and in the bulk. This was a motivation to increase the perovskite thickness to values close to 1  $\mu\text{m}$ , trying to maximize the light harvesting, and consequently, the device short circuit current. After optimizing the perovskite deposition to increase the total thickness, the resulting devices achieved a higher  $J_{\text{sc}}$  while maintaining the same the  $V_{\text{oc}}$  and FF. This led to a champion cell of almost 21% PCE (figure 18, right), beating the current efficiency record for vacuum-deposited MAPI perovskite. The PV parameters of the record device are summarized in table 2. Such a good performance with a very thick perovskite film highlights the long diffusion lengths of charge carriers achievable by sublimed perovskites, at least higher than 1  $\mu\text{m}$ , something challenging to achieve by solution process.

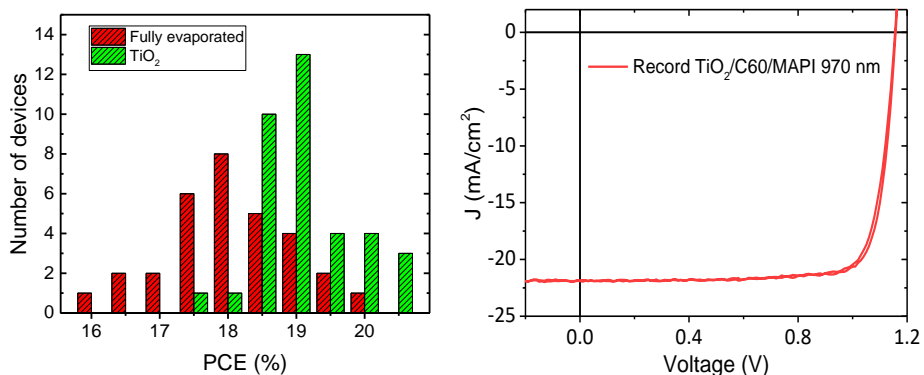


**Figure 18:** Statistical distribution of the power conversion efficiency obtained for the fully evaporated devices from reference 82 and for our configuration employing  $\text{TiO}_2/\text{C}_{60}$  (left) and J-V curve of the best device (right).

**Table 2:** Record device with the corresponding photovoltaic parameters.

Best cell	PCE (%)	V <sub>oc</sub> (V)	J <sub>sc</sub> (mA/cm <sup>2</sup> )	FF (%)
TiO <sub>2</sub> /C <sub>60</sub>	20.83	1.158	21.91	82.09

### 3.4 Conclusions

In conclusion, we report the fabrication of high efficiency vacuum-deposited perovskite solar cells using a TiO<sub>2</sub> electron transport layer fabricated from a nanoparticle dispersion. The power conversion efficiencies obtained are over 20%, being among the highest for CH<sub>3</sub>NH<sub>3</sub>PbI<sub>3</sub> perovskite. An interlayer of fullerene C<sub>60</sub> is needed between the TiO<sub>2</sub> and the perovskite in order to ensure a proper substrate for the perovskite deposition and to passivate the shallow trap states of the metal oxide. An activation process is observed, which can be boosted by the small UV component present in a full AM1.5G spectrum. In this process, electronic traps within the TiO<sub>2</sub> are filled and the band alignment is improved, thus increasing the FF to values higher than 80%. This is demonstrated by kelvin probe measurements showing a clear variation of the material's work function upon UV exposure and by means of impedance spectroscopy analysis, finding a clear variation of the capacitance at the interfaces. This work opens new avenues for using metal oxides as charge extracting materials in vacuum-deposited solar cells overcoming the problems of deposition on bare metal oxides and inadequate band alignment. Not only that, but also the use of sintered nanoparticles allows the use of low temperature deposition, opening the possibility of using sensitive substrates such as flexible PET foils or tandem solar cells.

### 3.5 Contribution of the author

The work developed in this chapter was carried out in collaboration with Dr. Afshin Hadipour from the Interuniversity Microelectronics Centre (IMEC), where the TiO<sub>2</sub> nanoparticle dispersion was synthesized. All the fabrication and characterization tasks were performed in the Molecular Science Institute (ICMol) from the University of Valencia. The author developed the main fabrication and characterization tasks along with the writing of the manuscript.

**Daniel Pérez-del-Rey**, Pablo P. Boix, Michele Sessolo, Afshin Hadipour, Henk J. Bolink. "Interfacial Modification for High-Efficiency Vapor-Phase-Deposited Perovskite Solar Cells Based on a Metal Oxide Buffer Layer". *The journal of physical chemistry letters* 9 (5), 1041-1046.



Letter

pubs.acs.org/JPCL

## Interfacial Modification for High-Efficiency Vapor-Phase-Deposited Perovskite Solar Cells Based on a Metal Oxide Buffer Layer

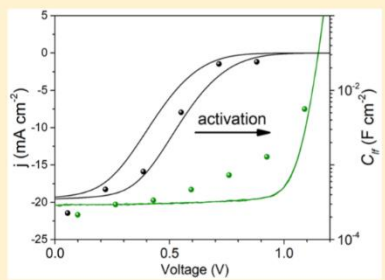
Daniel Pérez-del-Rey,<sup>†</sup> Pablo P. Boix,<sup>\*,†,○</sup> Michele Sessolo,<sup>,†,○</sup> Afshin Hadipour,<sup>,‡</sup> and Henk J. Bolink<sup>\*,†,○</sup>

<sup>†</sup>Instituto de Ciencia Molecular, Universidad de Valencia, C/J. Beltrán 2, 46980 Paterna, Spain

<sup>‡</sup>IMEC, Kapeldreef 75, 3000 Leuven, Belgium

### Supporting Information

**ABSTRACT:** Vacuum deposition is one of the most technologically relevant techniques for the fabrication of perovskite solar cells. The most efficient vacuum-based devices rely on doped organic contacts, compromising the long-term stability of the system. Here, we introduce an inorganic electron-transporting material to obtain power conversion efficiencies matching the best performing vacuum-deposited devices, with open-circuit potential close to the thermodynamic limit. We analyze the leakage current reduction and the interfacial recombination improvement upon use of a thin (<10 nm) interlayer of  $C_{60}$  as well as a more favorable band alignment after a bias/ultraviolet light activation process. This work presents an alternative for organic contacts in highly efficient vacuum-deposited perovskite solar cells.



Metal halide perovskite photovoltaics have become the most promising alternative to current commercial solar cells because of these materials' unprecedented properties, such as high light absorption coefficient, electron–hole diffusion lengths, and band gap tunability, among others.<sup>1–3</sup> As a result, the efficiency of the perovskite solar cells (PSC) has increased abruptly in the past decade, reaching record values of 22.1%.<sup>4</sup> Despite the excellent performances achieved by perovskite solar cells, rivalling those of Si devices, the main concerns for the commercialization lie in device stability and processability.

To make the leap from the laboratory to industrial production, it is necessary to optimize the deposition processes, implementing a scalable and profitable fabrication procedure. Vacuum deposition stands out as a technique with the advantages of avoiding problems of miscibility and precursors compatibility, as well as the toxicity of the solvents.<sup>5</sup> It is widespread in several fields, such as the organic light-emitting diodes industry, where they are mass produced in the form of fully evaporated devices. The highest reported efficiency for a vacuum-deposited perovskite solar cell, obtained with the archetype perovskite  $\text{CH}_3\text{NH}_3\text{PbI}_3$  (~20%),<sup>6</sup> is still lower than the record device prepared by solution processes, with important differences such as the perovskite composition. Interestingly, the best-performing solution-processed cells usually employ titanium dioxide,  $\text{TiO}_2$ , as the electron collection layer.  $\text{TiO}_2$ , in its anatase form, is a widely studied metal oxide in different photovoltaic fields, successfully implemented in perovskite solar cells as mesoporous and/or compact layers. Despite the advantages of this material, such as easy deposition, transparency, and good electron collection and transport, their use in vacuum-deposited perovskite solar cells has been limited. The replacement of doped organic charge

collection layers, employed in the most efficient vacuum-deposited perovskite solar cells, by  $\text{TiO}_2$  could circumvent disadvantages associated with these materials, such as chemical instability and parasitic light absorption.<sup>6</sup> Thus, developing methods to combine inorganic charge-transporting materials with vacuum-deposited perovskites can be an important contribution to the development of highly efficient and stable solar cells.

Here we report the use of a charge transport layer based on  $\text{TiO}_2$  as the electron contact for vacuum-deposited perovskite solar cells based on  $\text{CH}_3\text{NH}_3\text{PbI}_3$ . Efficient devices are obtained only when a thin layer of  $C_{60}$  is deposited on top of the  $\text{TiO}_2$ . Furthermore, we analyze the effect of a device activation process strongly dependent on bias and ultraviolet (UV) light exposure, which suppresses the charge extraction barrier and enables the highest efficiencies. The devices reach open-circuit voltages,  $V_{oo}$ , of 1.17 V, which are, to the best of our knowledge, the highest reported for  $\text{CH}_3\text{NH}_3\text{PbI}_3$  perovskites to date.<sup>7,8</sup> Together with short-circuit current densities,  $J_{sc}$ , of up to 21–22  $\text{mA cm}^{-2}$  and fill factors, FF, above 80%, the devices achieve power conversion efficiencies exceeding 20%.

The  $\text{TiO}_2$  films are deposited from a suspension of  $\text{TiO}_2$  nanoparticles in ethanol. This process requires a relatively low temperature annealing (100 °C), which makes it compatible with ITO substrates (details in Materials). The resulting films can be employed as electron transport layer (ETL) in vacuum-deposited perovskite solar cells with the configuration ITO/ $\text{TiO}_2/\text{CH}_3\text{NH}_3\text{PbI}_3/\text{HTL}/\text{doped HTL}/\text{Au}$ , where the hole

Received: December 20, 2017

Accepted: February 12, 2018

Published: February 12, 2018

transport layer (HTL) used is a derivative of an arylamine ( $N_4N_4N_4''N_4'''$ -tetra([1,1'-biphenyl]-4-yl)-[1,1':4',1''-terphenyl]-4,4''-diamine, abbreviated as TaTm) and the doped HTL is the same molecule partially oxidized by cosublimation with 2,2'-(perfluoronaphthalene-2,6-diylidene) dimalononitrile, abbreviated as  $F_6$ -TCNNQ. The full device architecture is depicted in Figure 1.

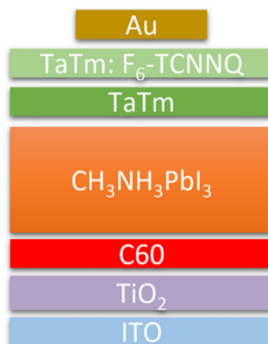


**Figure 1.** Device structure where  $TiO_2$  has a thickness of 30 nm, the  $C_{60}$  10 nm, the perovskite 590 nm, TaTm 10 nm, TaTm: $F_6$ -TCNNQ 40 nm, and gold 100 nm. Samples without the  $C_{60}$  layer present the same thickness in the rest of the layers.

The performance of these solar cells is significantly lower than what is reported for spin-coated  $CH_3NH_3PbI_3/TiO_2$ -based devices in the literature. Under 100 mW cm<sup>-2</sup> calibrated illumination, with the UV component of the illumination filtered to avoid  $TiO_2$  degradation,<sup>9</sup> the devices display a  $V_{oc}$  of ~1 V,  $J_{sc}$  of about 9 mA cm<sup>-2</sup>, and FF of 25%, leading to an efficiency of ~4%. The extremely low FF, which strongly limits the cell performance, can be due to a series of factors, such as (a) leakage pathways in the cell ETL, which can be estimated from the dark current–voltage characteristics; (b) shallow trap states in the  $TiO_2$  that enhance the recombination and reduce the photoconductivity of this layer;<sup>10</sup> or (c) poor band alignment.<sup>11</sup> However, upon several forward (from  $J_{sc}$  to  $V_{oc}$ ) and reverse (from  $V_{oc}$  to  $J_{sc}$ ) alternating scans, the FF improves (from 24 to 31%) as does the  $J_{sc}$  (from 8 to 14 mA cm<sup>-2</sup>). Nevertheless, the overall power conversion efficiencies improvement saturated after ~10 scans, and the efficiency remained under 5% (Figure 2). Dark current density–voltage ( $J$ – $V$ ) analysis of the cells indicates the presence of leakage paths (Figure S1), which influence the  $V_{oc}$  and importantly the FF. These leakage paths may be related to the pinholes in the  $TiO_2$  layer that were revealed by the surface profile measured with atomic force microscopy (AFM) showing 30 nm deep pinholes in a 50–80 nm thick layer (Figure S4).

The insertion of a layer of a fullerene-derivative between the  $TiO_2$  and the perovskite has been reported to improve the electron-extracting interface due to a surface trap passivation,<sup>12</sup> while the full coverage with an intrinsic material such as  $C_{60}$  has been demonstrated to reduce the leakage current.<sup>6</sup> Therefore, a thin layer (10 nm) of  $C_{60}$  was sublimed onto the spin-coated  $TiO_2$  film prior to the perovskite deposition. Previous reports using such a layer as the sole electron-selective and extracting contact resulted in poor performance, which was attributed to the material's charge transport properties.<sup>6</sup> However, the use of

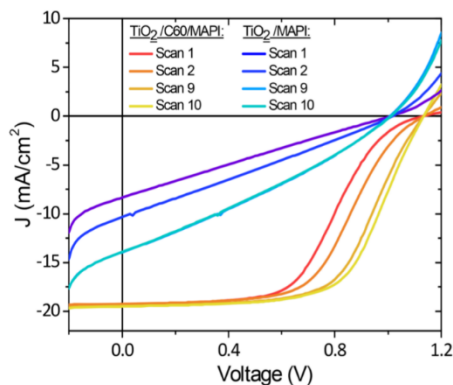


**Figure 2.**  $J$ – $V$  characteristics under illumination of solar cells using  $TiO_2$  nanoparticles as ETL with and without a thin layer (10 nm) of  $C_{60}$  and measured from  $V_{oc}$  to  $J_{sc}$  several times.

$C_{60}$  as an interlayer in our system results in a significant improvement of all performance parameters ( $J_{sc}$  from 15 to 20 mA cm<sup>-2</sup>,  $V_{oc}$  from 1.0 to >1.12 V, and FF from 20 to ~60%), yet with the overall efficiency still limited to less than 16%. Consecutive  $J$ – $V$  measurements, alternating forward and reverse scans, result again in a FF increase, reducing the characteristic S-shape present in the initial scans while leaving unchanged  $V_{oc}$  and  $J_{sc}$  (Figure 2). The characteristics of the curves remained practically constant from the 10th scan onward. All cell parameters for the first and the last scan, with and without  $C_{60}$ , are summarized in Table 1.

**Table 1. Solar Cell Parameters under Solar Simulated Illumination without UV Component**

sample	scan number	$V_{oc}$ (V)	$J_{sc}$ (mA cm <sup>-2</sup> )	FF (%)	PCE (%)
$TiO_2$	scan 1	1.00	8.3	24.3	2
	scan 10	1.02	14.2	31.3	4
$TiO_2/C_{60}$	scan 1	1.12	19.3	50.3	11
	scan 10	1.12	19.5	62.5	14

In order to elucidate the mechanisms governing the activation process, we measured the solar cells with and without  $C_{60}$  under full simulated solar spectrum with AM1.5G illumination. In contrast to previous reports, where the UV-component in the light source was detrimental to the  $TiO_2$ /perovskite devices,<sup>9</sup> we observed a clear improvement in the photovoltaic behavior of the devices and especially a faster activation process. For the solar cells with the structure  $TiO_2$ /perovskite, the full suppression of hysteresis and performance saturation was reached after 2–3 scans, with the FF as the main improved parameter (in contrast to both FF and  $J_{sc}$  enhancement in the previous experiment) (Figure 3a). Solar cells with a  $C_{60}$  interlayer show a substantial improvement of FF in just 1 scan, whereas both  $V_{oc}$  and  $J_{sc}$  remain unvaried. After 3 scans, the devices maintain its peak performance with negligible hysteresis, and no significant change is observed (Figure 3b) during consecutive scans nor after prolonged light exposure. All cell parameters for the first and the last scan in both directions under full sun spectra are summarized in Table 2.

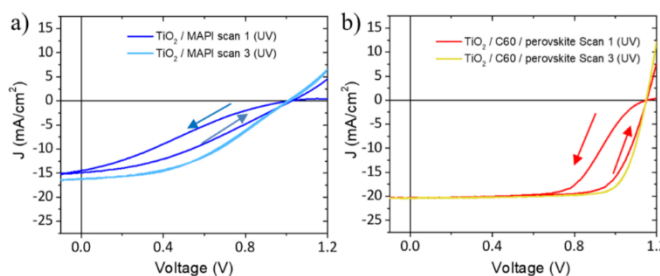


**Figure 3.** Representative  $J$ – $V$  characteristics under illumination of a solar cell without (a) and with  $C_{60}$  (b) under a full simulated solar spectrum.

**Table 2. Solar Cell Parameters under Full Solar Spectrum Illumination<sup>a</sup>**

sample	scan number (direction)	$V_{oc}$ (V)	$J_{sc}$ (mA cm <sup>-2</sup> )	FF (%)	PCE (%)
$TiO_2$	scan 1 (reverse)	1.02	14.47	24.5	4
	scan 1 (forward)	1.03	14.92	35.1	5
	scan 3 (reverse)	1.01	16.30	42.2	7
	scan 3 (forward)	1.00	16.18	42.2	7
$TiO_2/C_{60}$	scan 1 (reverse)	1.15	20.40	54.6	13
	scan 1 (forward)	1.15	20.35	71.1	17
	scan 3 (reverse)	1.15	20.54	76.1	18
	scan 3 (forward)	1.15	20.55	76.3	18

<sup>a</sup>The measurements were performed first in reverse (from positive to negative bias) and immediately after in forward direction (from negative to positive bias).

Besides the significantly faster activation obtained upon addition of  $TiO_2/C_{60}$  as electron-selective contact, these solar cells display efficiencies between 18 and 19%, with a champion device reaching 20.8% (Figure S2). These values are on par with those of the best vacuum-deposited perovskite cells<sup>6</sup> based in doped organic ETLs, yet with enhanced reproducibility (Figure S3). The record  $V_{oc}$  obtained, 1.17 V, has only a 390 mV deficit compared with the charge energy corresponding to the material's band gap, 1.56 eV (as calculated from the Tauc plot in Figure S7), and it is only 119 mV lower than the highest achievable value for this band gap's Shockley–Queisser limit.<sup>13</sup> This is among the highest reported photovoltages for pure  $CH_3NH_3PbI_3$  cells,<sup>7</sup> and a clear indication of the reduced nonradiative recombination occurring in these devices.

Once the cells are exposed to full solar simulated spectra, with the corresponding UV component, the devices stay in the hysteresis-free highest-performing condition, reproducing the best results even under lamps without UV-component. After a few minutes, the FF starts to drop until reaching the full "deactivated" state overnight (Figure 4). Interestingly, the use of the full AM1.5G spectra with UV component does not compromise the device performance, which is robust under continuous illumination (Figure S9). Furthermore, encapsulated devices maintain the efficiency (with the corresponding 2–3 activation scans) in subsequent days.

Similar UV activation phenomena in  $TiO_2$ -based devices have been previously described, especially in the OPV field, with interpretations related to adsorbed molecular oxygen or shallow charge carrier traps that are filled upon UV illumination.<sup>10</sup> Other works in the perovskite field account a similar activation process to ion migration, in particular to the accumulation of  $MA^+$  cations at the fullerene/perovskite

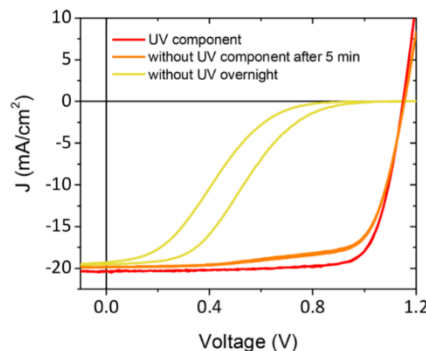


**Figure 4.** Current–voltage characteristics of cells with  $C_{60}$  interlayer illustrating the deactivation process over time.

interface which reduces its energy disorder and enhances the  $V_{oc}$ .<sup>14</sup> The devices without  $C_{60}$  show a change in  $J_{sc}$  during photoactivation, in good agreement with trap filling at the  $TiO_2$ /perovskite interface. Nevertheless, these devices are still strongly dominated by the leakage current, which keeps the FF as the limiting factor as previously discussed. In contrast,  $J_{sc}$  and  $V_{oc}$  are not affected by the activation in the systems with the  $C_{60}$  interlayer. In order to understand the photoactivation effect in that device configuration, the work function of the  $TiO_2$  films with and without  $C_{60}$  was estimated with Kelvin probe before and after the UV exposure (Figure S5). The results show a decrease of about 300 mV for  $TiO_2$  upon activation, while a smaller difference of about 100 mV is observed in  $TiO_2/C_{60}$  systems. This is interpreted by stronger effect of the trap filling in the absence of the fullerene layer, which can passivate the  $TiO_2$  surface states. In absolute terms, the activation in the system with the  $C_{60}$  interlayer moves the work function values toward those measured in the  $C_{60}$ -free system. This point is in good agreement with the leakage limitation of the performance observed in the fullerene-free devices, as previously discussed.

Further study of the band alignment in  $TiO_2/C_{60}$  systems in full solar cell configuration is carried out by impedance spectroscopy. This technique applies a small voltage perturbation which allows characterizing the device at any steady state. The full spectra of the samples were measured under white halogen illumination (without UV component) before and after UV activation. The fitting of the impedance results to a simple equivalent circuit<sup>15</sup> (Figure S5a) allows extracting the high- and low-frequency capacitances. The former, typically ascribed to the geometric capacitance of the

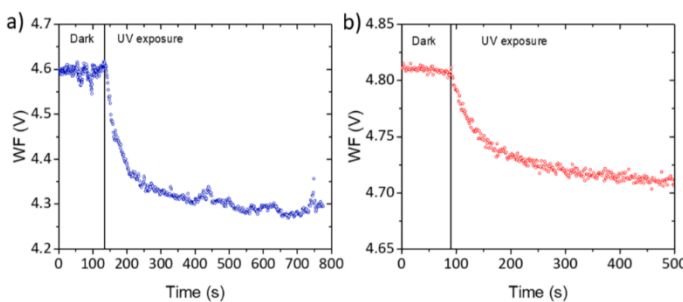


**Figure 5.** Kelvin probe (KP) measurement of a  $\text{TiO}_2$  (a) and  $\text{TiO}_2/\text{C}_{60}$  (b) layer with and without UV illumination.

perovskite film, does not show significant variation upon activation (Figure S5b), indicating that the process does not modify the dielectric properties of the absorber. The low-frequency capacitance, in contrast, displays a clear shift upon activation (Figure 6). This parameter is generally associated

limits the device performance, which can be overcome by the introduction of a thin interlayer of  $\text{C}_{60}$  (<10 nm). An activation process, strongly accelerated under UV-exposure, is necessary to fill the  $\text{TiO}_2$  traps and improve the band alignment, as demonstrated by Kelvin probe and impedance spectroscopy analysis. This work opens new avenues for using inorganic materials as charge-extracting materials in vacuum-deposited solar cells.

## ■ EXPERIMENTAL METHODS

Photolithographically patterned ITO coated glass substrates were purchased from Naranjo Substrates. 2,2'-(Perfluoronaphthalene-2,6-diylidene)-dimalononitrile ( $\text{F}_6\text{-TCNNQ}$ ),  $\text{N},\text{N},\text{N}^{\prime},\text{N}^{\prime\prime}\text{-tetra}([1,1'\text{-biphenyl}]_4\text{-yl})[1,1':4',1''\text{-terphenyl}]_4,4''\text{-diamine}$  ( $\text{TaTm}$ ) and  $\text{N},\text{N}\text{-bis}(\text{tri}-\text{p-tolylphosphoranylidene})\text{benzene-1,4-diamine}$  ( $\text{Phlm}$ ) were provided from Novaled GmbH.  $\text{TiO}_2$  nanoparticle suspensions were prepared in IMEC and deposited through a low-temperature process compatible with ITO substrates. A nonaqueous sol-gel route is used,<sup>18</sup> in which the oxygen required for the nanoparticle formation is provided by benzyl alcohol. In detail, 2 mL of anhydrous ethanol is mixed with 0.5 mL of titanium(IV) chloride ( $\text{TiCl}_4$  from Sigma-Aldrich) inside a nitrogen field glovebox. After the mixture is stirred for 10 min at room temperature, 10 mL of benzyl alcohol (Sigma-Aldrich) is added to the mixture leading to a light yellow and clear solution. This solution is stirred for at least 18 h at 80 °C leading to colorless hazy suspension. The haziness of the suspension is caused by creation of white titanium oxide nanoparticles. In order to separate them, 1 mL of the resulting milky suspension was precipitated in 10 mL of diethyl ether (from Sigma-Aldrich) and centrifuged at 5000 rpm for 2 min to isolate the nanoparticles from the solvent and the unreacted precursor. After the sample was centrifuged, the solvent was drained out and solid white nanoparticles were dispersed into 3 mL of pure ethanol leading to a milky (white and hazy) solution. In order to stabilize this final dispersion, 45  $\mu\text{L}$  of diisopropoxytitaan-bis(acetylacetonaat) ( $\text{TiAcac}$  purchased from Sigma-Aldrich) is added to the solution. After less than 1 h, a light green and clear solution is created.<sup>19</sup> This is the final product containing  $\text{TiO}_2$  nanoparticles in pure ethanol. After spin coating of the  $\text{TiO}_2$  dispersion, the substrates are annealed at 100 °C for 15 min in air. Fullerene ( $\text{C}_{60}$ ) was purchased from sigma Aldrich.  $\text{PbI}_2$  was purchased from Tokyo Chemical Industry CO (TCI), and  $\text{CH}_3\text{NH}_3\text{I}$  (MAI) was purchased from Lumtec.

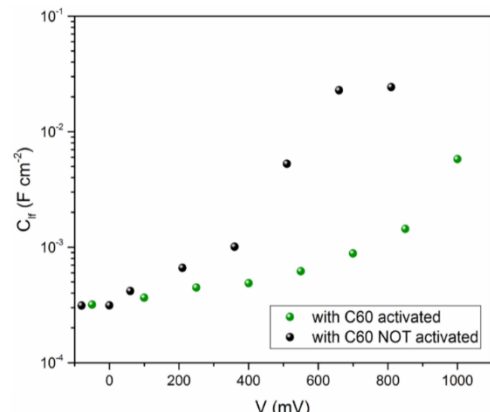


**Figure 6.** Low-frequency capacitance obtained from the impedance spectroscopy fitting of solar cells with and without  $\text{C}_{60}$  interlayer under illumination.

with the charge accumulation at the perovskite/ $\text{TiO}_2$  interface.<sup>16</sup> The low-frequency capacitance measured for the not-activated cell displays a rapid increase at  $\sim 500$  mV, the region where the shape of the  $J-V$  curve starts the S-shape. This increase of capacitance is shifted toward higher values ( $\sim 800$  mV) upon activation, consistent with the work function variation and with the  $J-V$  characteristics. It is worth noting the similar values ultimately reached by the capacitance, which are reflected in the similar  $V_{oc}$  independently of the activation. Analogously, the unmodified  $J_{SC}$  of the device indicates an optimum band alignment at 0 V, unaffected by the activation. Therefore, all our results suggest that band alignment plays a major role in the UV-induced activation process in the  $\text{TiO}_2/\text{C}_{60}$ -based devices, reducing the barrier which limits the charge extraction at intermediate voltages, in turn limiting the FF of the devices, as previously investigated for hybrid solar cells.<sup>17</sup>

In conclusion, we have reported the fabrication of  $\text{TiO}_2$ -based vacuum-deposited MAPI solar cells with power conversion efficiencies over 20%. The leakage current severely

**Device Preparation.** ITO-coated glass substrates were subsequently cleaned with soap, water, and isopropanol in an ultrasonic bath, followed by UV-ozone treatment. The  $\text{TiO}_2$  dispersion was deposited in air by spin-coating at 3000 rpm for 30 s and annealed at 100 °C for 30 min, leading to a 50–80 nm thick compact layer. Then, they were transferred to a vacuum chamber integrated into a nitrogen-filled glovebox ( $\text{H}_2\text{O}$  and  $\text{O}_2 < 0.1 \text{ ppm}$ ) and evacuated to a pressure of  $10^{-6} \text{ mbar}$ . The vacuum chamber is equipped with six temperature-controlled evaporation sources (Creaphys) fitted with ceramic crucibles. The sources were directed upward with an angle of approximately 90° with respect to the bottom of the evaporator. The substrate holder to evaporation sources distance is approximately 20 cm. Three quartz crystal microbalance (QCM) sensors are used: two monitoring the deposition rate of each evaporation source and a third one close to the substrate holder monitoring the total deposition rate. For thickness calibration, we first individually sublimed the charge transport materials and the HTM dopant (TaTm,  $\text{F}_6\text{-TCNNQ}$  and  $\text{C}_{60}$ ). A calibration factor was obtained by comparing the thickness inferred from the QCM sensors with that measured with a mechanical profilometer (Ambios XP1). Then these materials were cosublimed at temperatures ranging from 135 to 160 °C for the dopants to 250 °C for the pure charge transport molecules, and the evaporation rate was controlled by separate QCM sensors and adjusted to obtain the desired doping concentration. In general, the deposition rate for TaTm was kept constant at  $0.8 \text{ \AA s}^{-1}$  while varying the deposition rate of the dopant during codeposition. Pure TaTm and  $\text{C}_{60}$  layers were deposited at a rate of  $0.5 \text{ \AA s}^{-1}$ .

For the n-i-p configuration, after deposition the  $\text{TiO}_2$  layer is annealed at 100 °C for 15 min in air. Then, 10 nm thick  $\text{C}_{60}$  is vacuum-deposited in the case where we specify its presence in the layout. Once this deposition was completed, the chamber was vented with dry  $\text{N}_2$  to replace the  $\text{C}_{60}$  crucible with those containing the starting materials for the perovskite deposition,  $\text{PbI}_2$  and  $\text{CH}_3\text{NH}_3\text{I}$ . The vacuum chamber was evacuated again to a pressure of  $10^{-6} \text{ mbar}$ , and the perovskite films were then obtained by codeposition of the two precursors. The calibration of the deposition rate for the  $\text{CH}_3\text{NH}_3\text{I}$  was found to be difficult because of nonuniform layers and the soft nature of the material, which impeded accurate thickness measurements. Hence, the source temperature of the  $\text{CH}_3\text{NH}_3\text{I}$  was kept constant at 70 °C and the  $\text{CH}_3\text{NH}_3\text{I}:\text{PbI}_2$  ratio was controlled off line using grazing incident X-ray diffraction by adjusting the  $\text{PbI}_2$  deposition temperature. The optimum deposition temperatures were found to be 250 °C for the  $\text{PbI}_2$  and 70 °C for the  $\text{CH}_3\text{NH}_3\text{I}$ . After deposition of a 500 nm thick perovskite film, the chamber was vented and the crucibles were replaced with those containing TaTm and  $\text{F}_6\text{-TCNNQ}$ ; the chamber was then evacuated again to a pressure of  $10^{-6} \text{ mbar}$ . The devices were completed by depositing a film of pure TaTm and one of the p-ETL (TaTm: $\text{F}_6\text{-TCNNQ}$ ), with thicknesses of 10 and 40 nm, respectively. Finally, the substrates were transferred to a second vacuum chamber where the metal top contact (Au, 100 nm thick) was deposited.

Surface morphology of the thin films was analyzed using AFM (Multimode SPM, Veeco, United States). Scanning electron microscopy (SEM) images were obtained on a Hitachi S-4800 microscope operating at an accelerating voltage of 2 kV over Platinum-metallized samples. Absorption spectra were collected using a fiber-optics based Avantes Avaspec2048 Spectrometer. Characterization of the solar cells was performed

as follows. The external quantum efficiency (EQE) was estimated using the cell response at different wavelengths (measured with a white light halogen lamp in combination with band-pass filters), where the solar spectrum mismatch is corrected using a calibrated Silicon reference cell (MiniSun simulator by ECN, The Netherlands). The  $J$ – $V$  characteristics were obtained using a Keithley 2400 source measure unit and under white light illumination, and the short-circuit current density was corrected taking into account the device EQE. The electrical characterization was validated using a solar simulator by Abet Technologies (model 10500 with an AM1.5G xenon lamp as the light source). Before each measurement, the exact light intensity was determined using a calibrated Si reference diode equipped with an infrared cutoff filter (KG-3, Schott). The  $J$ – $V$  curves were recorded between  $-0.2$  and  $1.2 \text{ V}$  with  $0.01 \text{ V}$  steps, integrating the signal for 20 ms after a 10 ms delay. This corresponds to a speed of about  $0.3 \text{ V s}^{-1}$ . The layout used to test the solar cells has four equal areas ( $0.0625 \text{ cm}^2$ , defined as the overlap between the ITO and the top metal contact) and measured through a shadow mask with  $0.01 \text{ cm}^2$  aperture.

## ■ ASSOCIATED CONTENT

### Supporting Information

The Supporting Information is available free of charge on the ACS Publications website at DOI: [10.1021/acs.jpclett.7b03361](https://doi.org/10.1021/acs.jpclett.7b03361).

Figures S1–S9 as noted in the text (PDF)

## ■ AUTHOR INFORMATION

### Corresponding Authors

\*E-mail: Pablo.P.Boix@uv.es.

\*E-mail: henk.bolink@uv.es.

### ORCID

Pablo P. Boix: [0000-0001-9518-7549](https://orcid.org/0000-0001-9518-7549)

Michele Sessolo: [0000-0002-9189-3005](https://orcid.org/0000-0002-9189-3005)

Henk J. Bolink: [0000-0001-9784-6253](https://orcid.org/0000-0001-9784-6253)

### Notes

The authors declare no competing financial interest.

## ■ ACKNOWLEDGMENTS

We acknowledge financial support from the European Union H2020 project INFORM (Grant 675867); the Spanish Ministry of Economy and Competitiveness (MINECO) via the Unidad de Excelencia María de Maeztu MDM-2015-0538, MAT2014-55200, PCIN-2015-255, MAT2017-88905-P and MAT2017-88905-P; and the Generalitat Valenciana (Prometeo/2016/135). M.S. and P.P.B. thank the MINECO for their postdoctoral RyC contracts. P.P.B. acknowledges the financial support from the Conselleria d'Educació, Investigació, Cultura i Esport Valenciana (SEJ12017/2017/012).

## ■ REFERENCES

- Berry, J.; Buonassisi, T.; Egger, D. A.; Hodes, G.; Kronik, L.; Loo, Y.-L.; Lubomirsky, I.; Marder, S. R.; Mastai, Y.; Miller, J. S.; et al. Hybrid organic–inorganic perovskites (HOIPs): opportunities and challenges. *Adv. Mater.* **2015**, *27*, 5102–5112.
- Brenner, T. M.; Egger, D. A.; Kronik, L.; Hodes, G.; Cahen, D. Hybrid organic–inorganic perovskites: low-cost semiconductors with intriguing charge-transport properties. *Nat. Rev. Mater.* **2016**, *1*, 15007.
- Stoumpos, C. C.; Kanatzidis, M. G. Halide perovskites: Poor man's high-performance semiconductors. *Adv. Mater.* **2016**, *28*, 5778–5793.

- (4) Yang, W. S.; Park, B.-W.; Jung, E. H.; Jeon, N. J.; Kim, Y. C.; Lee, D. U.; Shin, S. S.; Seo, J.; Kim, E. K.; Noh, J. H.; et al. Iodide management in formamidinium-lead-halide-based perovskite layers for efficient solar cells. *Science* **2017**, *356*, 1376–1379.
- (5) Ávila, J.; Momblona, C.; Boix, P. P.; Sessolo, M.; Bolink, H. J. Vapor-deposited perovskites: the route to high-performance solar cell production? *Joule* **2017**, *1*, 431–442.
- (6) Momblona, C.; Gil-Escrí, L.; Bandiello, E.; Hutter, E. M.; Sessolo, M.; Lederer, K.; Blochwitz-Nimoth, J.; Bolink, H. J. Efficient vacuum deposited p-i-n and n-i-p perovskite solar cells employing doped charge transport layers. *Energy Environ. Sci.* **2016**, *9*, 3456–3463.
- (7) Tress, W. Perovskite solar cells on the way to their radiative efficiency limit – insights into a success story of high open-circuit voltage and low recombination. *Adv. Energy Mater.* **2017**, *7*, 1602358.
- (8) Son, D.-Y.; Lee, J.-W.; Choi, Y. J.; Jang, I.-H.; Lee, S.; Yoo, P. J.; Shin, H.; Ahn, N.; Choi, M.; Kim, D.; et al. Self-formed grain boundary healing layer for highly efficient CH<sub>3</sub>NH<sub>3</sub>PbI<sub>3</sub> perovskite solar cells. *Nat. Energy* **2016**, *1*, 16081.
- (9) Lee, S.-W.; Kim, S.; Bae, S.; Cho, K.; Chung, T.; Mundt, L. E.; Lee, S.; Park, S.; Park, H.; Schubert, M. C.; et al. UV degradation and recovery of perovskite solar cells. *Sci. Rep.* **2016**, *6*, 38150.
- (10) Bok Kim, J.; Ahn, S.; Ju Kang, S.; Nuckolls, C.; Loo, Y.-L. Ligand chemistry of titania precursor affects transient photovoltaic behavior in inverted organic solar cells. *Appl. Phys. Lett.* **2013**, *102*, 103302.
- (11) Guerrero, A.; Chambon, S.; Hirsch, L.; Garcia-Belmonte, G. Light-modulated TiO<sub>x</sub> interlayer dipole and contact activation in organic solar cell cathodes. *Adv. Funct. Mater.* **2014**, *24*, 6234–6240.
- (12) Peng, J.; Wu, Y.; Ye, W.; Jacobs, D. A.; Shen, H.; Fu, X.; Wan, Y.; Duong, T.; Wu, N.; Barugkin, C.; et al. Interface passivation using ultrathin polymer-fullerene films for high-efficiency perovskite solar cells with negligible hysteresis. *Energy Environ. Sci.* **2017**, *10*, 1792–1800.
- (13) Rühle, S. Tabulated values of the Shockley–Queisser limit for single junction solar cells. *Sol. Energy* **2016**, *130*, 139–147.
- (14) Zhang, T.; Cheung, S. H.; Meng, X.; Zhu, L.; Bai, Y.; Ho, C. H. Y.; Xiao, S.; Xue, Q.; So, S. K.; Yang, S. Pinning down the anomalous light soaking effect toward high-performance and fast-response perovskite solar cells: the ion-migration-induced charge accumulation. *J. Phys. Chem. Lett.* **2017**, *8*, 5069–5076.
- (15) Zarazua, I.; Han, G.; Boix, P. P.; Mhaisalkar, S.; Fabregat-Santiago, F.; Mora-Seró, I.; Bisquert, J.; Garcia-Belmonte, G. Surface recombination and collection efficiency in perovskite solar cells from impedance analysis. *J. Phys. Chem. Lett.* **2016**, *7*, 5105–5113.
- (16) Zarazua, I.; Bisquert, J.; Garcia-Belmonte, G. Light-induced space-charge accumulation zone as photovoltaic mechanism in perovskite solar cells. *J. Phys. Chem. Lett.* **2016**, *7*, 525–528.
- (17) Manor, A.; Katz, E. A.; Tromholt, T.; Krebs, F. C. Enhancing functionality of ZnO hole blocking layer in organic photovoltaics. *Sol. Energy Mater. Sol. Cells* **2012**, *98*, 491–493.
- (18) Niederberger, M. Nonaqueous sol–gel routes to metal oxide nanoparticles. *Acc. Chem. Res.* **2007**, *40*, 793–800.
- (19) Hadipour, A. Doped titanate. WO 2017/108710 A1, June 29th 2017.

**Supporting information**

# Interfacial Modification for High Efficiency Vapor Phase Deposited Perovskite Solar Cells Based on Metal-Oxide Buffer Layers

*Daniel Pérez-del-Rey<sup>1</sup>, Pablo P. Boix<sup>1</sup>, Michele Sessolo<sup>1</sup>, Afshin Hadipour<sup>2</sup>, Henk J. Bolink<sup>1</sup>*

<sup>1</sup>Instituto de Ciencia Molecular, Universidad de Valencia, C/J. Beltrán 2, 46980, Paterna, Spain

<sup>2</sup>IMEC, Kapeldreef 75, 3000 Leuven, Belgium

## AUTHOR INFORMATION

### **Corresponding Author**

Pablo P. Boix, e-mail: Pablo.P.Boix@uv.es  
Henk J. Bolink, e-mail: henk.bolink@uv.es

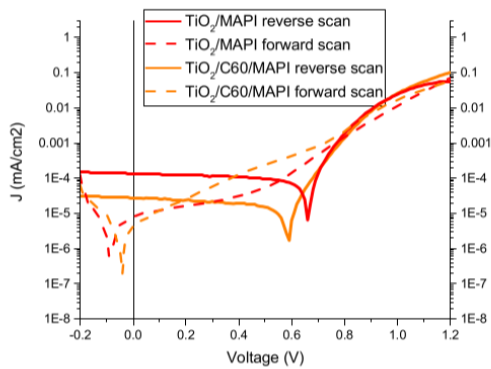


Figure S1: Dark J-V characteristics for devices with  $\text{TiO}_2$  and  $\text{TiO}_2/\text{C}_{60}$

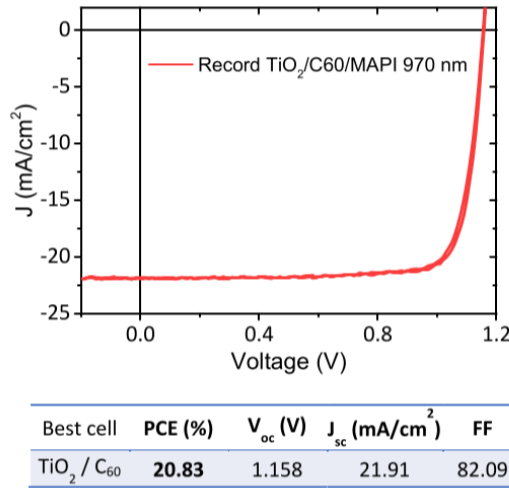


Figure S2: Record device with the corresponding photovoltaic parameters.

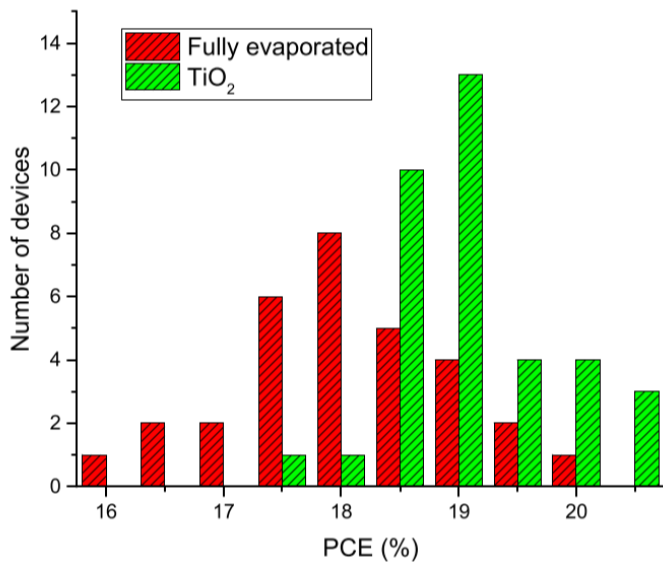


Figure S3: Statistical distribution of power conversion efficiency obtained for the devices from the fully evaporated solar cells publication and for our configuration employing  $\text{TiO}_2/\text{C}_{60}$

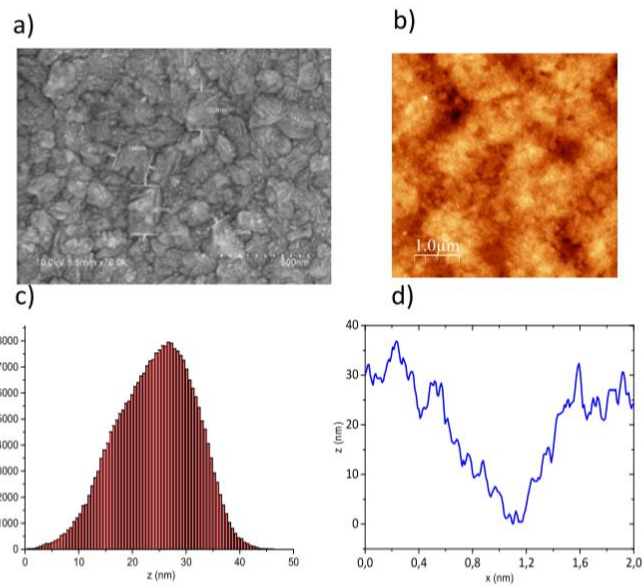


Figure S4: SEM (a) and AFM (b,c,d) analysis of the perovskite on top of  $\text{TiO}_2/\text{C}_{60}$ . C) shows height distribution and D) shows cross section.

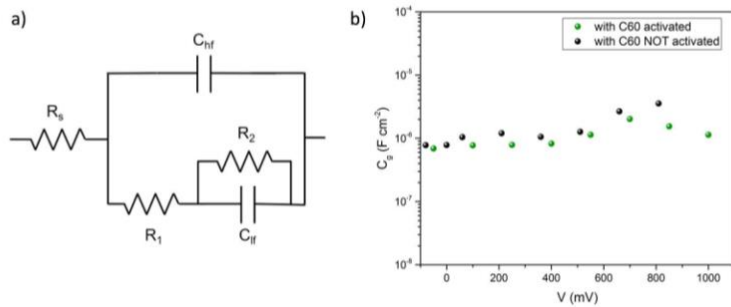


Figure S5: a) Equivalent circuit employed to fit the impedance spectroscopy results. b) geometric capacitance obtained for devices with and without  $\text{C}_{60}$  under illumination.

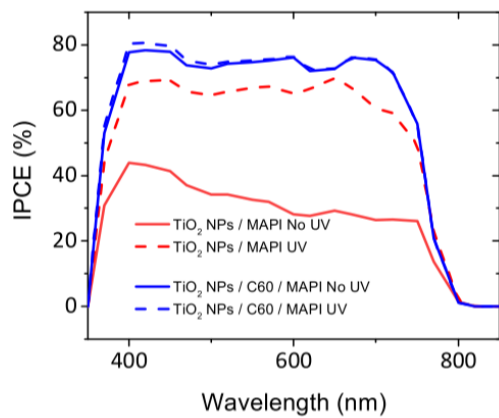


Figure S6: EQE of NiP devices with and without  $C_60$  activated and not activated with UV wavelengths

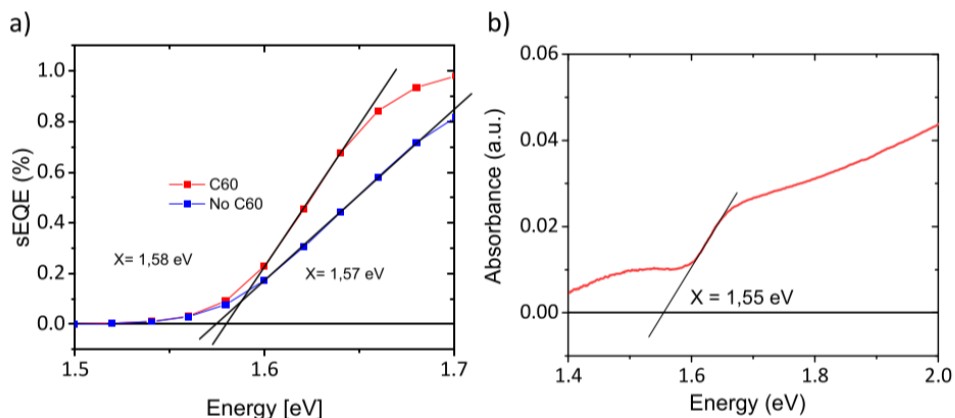


Figure S7: Band gap calculation of  $\text{CH}_3\text{NH}_3\text{PbI}_3$  perovskite with Tauc plot (a) and from sEQE (b)

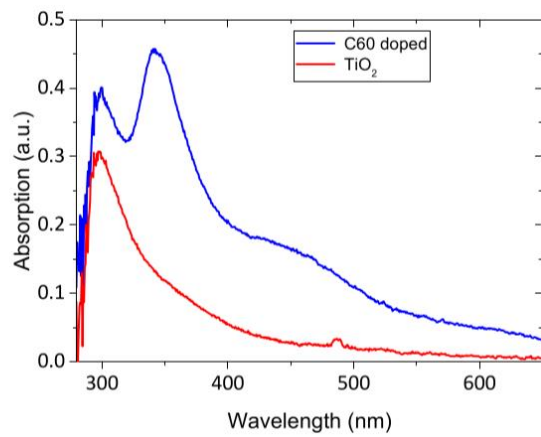


Figure S8: Absorption spectra of C60 doped and TiO<sub>2</sub>

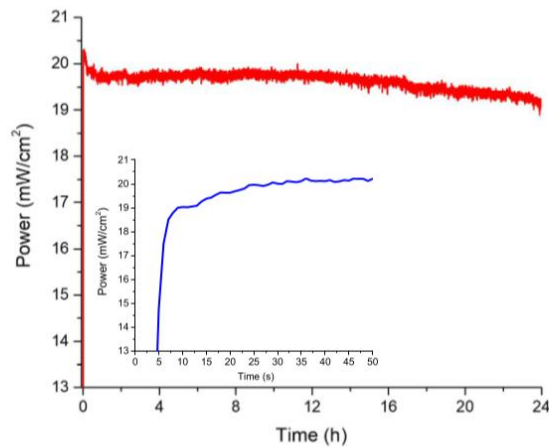


Figure S9: Maximum power point tracking. The inset shows the TiO<sub>2</sub> activation during the first seconds.

# **Chapter 4:**

## **Molecular Passivation of MoO<sub>3</sub>:**

### **Band Alignment and Protection of**

### **Charge Transport Layers in Vacuum-**

### **Deposited Perovskite Solar Cells**

*“Extraordinary claims require extraordinary evidence.”*

Carl Sagan



## 4. Molecular Passivation of MoO<sub>3</sub>: Band Alignment and Protection of Charge Transport Layers in Vacuum-Deposited Perovskite Solar Cells

The process developed in the previous chapter allowed us to successfully implement a metal oxide as the N material in the N-i-P structure. In this chapter, I targeted the P side, substituting the molecular P doped layer also for a metal oxide. To achieve this, I first optimized the deposition of MoO<sub>3</sub> in the P-i-N structure with efficiencies higher than 18% and then implemented it on top of the N-i-P stack developed in chapter 3, leading to the first configuration with two metal oxides in high efficiency vacuum-deposited perovskite solar cells.

### 4.1 Introduction

As discussed in the previous chapters, metal oxides are a promising alternative for doped organic layers in perovskite solar cells. Even though the record solution-processed N-i-P configurations employ a metal oxide on the N-side, they still rely on doped organic-based materials, such as Spiro-OMeTAD, for hole injection.<sup>57</sup> Similarly, high efficiency P-i-N solar cells commonly use polymers such as PEDOT:PSS or PTAA as hole transporting organic layers.<sup>90</sup>

For the substitution of doped organic layers, transition metal oxides (TMOs) are excellent candidates. This family of metal oxides has attracted interest in the field of optoelectronic devices since their first applications in OLEDs in the late 1990's.<sup>91</sup> They stand out due to their excellent charge transport properties, variable work function, and low parasitic absorption. TMOs can be prepared in thin films using a large variety of deposition techniques and they have a wide range of WF values, ranging from 3.5 eV for defective ZrO<sub>2</sub> to 7 eV for stoichiometric V<sub>2</sub>O<sub>5</sub> (figure 19).

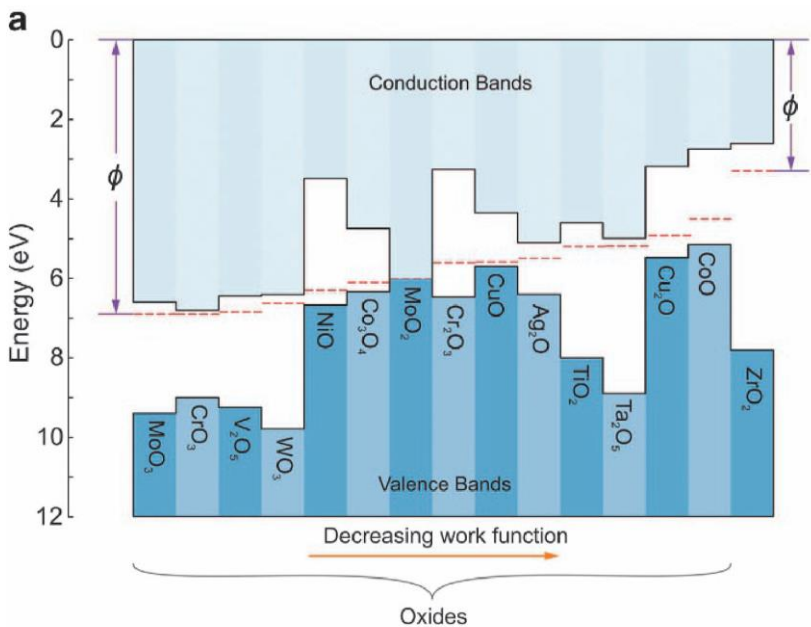


**Figure 19:** Energy levels of the main TMOs for optoelectronic applications (figure from reference 92).

As a result, an increasing number of studies have reported their use as hole transporting materials for perovskite solar cells. For example, P-i-N solar cells using NiO reached remarkable efficiencies higher than 21% and displayed long-term stability.<sup>93</sup> One negative aspect of NiO is that it generally needs a high temperature annealing, which has a negative impact on the N-i-P configuration.

On the other hand, high WF N-type TMOs are also interesting candidates for hole-injection. Some examples are MoO<sub>3</sub>, V<sub>2</sub>O<sub>5</sub> and WO<sub>3</sub>, where the N-type character arises from a slightly non-stoichiometric composition with an oxygen deficiency.<sup>94</sup> Despite being N-type materials, their deep conduction band, and their ionization energies higher than 6 eV, makes them very good hole injecting materials. As a consequence, these materials become potential alternatives for organic materials such as PEDOT:PSS, widely used in OLEDs<sup>91,95–97</sup> and solar cells.<sup>98,99</sup>

As a particular case, MoO<sub>3</sub> is an interesting candidate for the N-i-P configuration due to the possibility of being sublimed, avoiding the use of solvents that could damage the layers previously deposited. This material

cannot directly act as electron blocker due to its deep conduction band, which overlaps with the conduction and valence bands of MAPI. However, the band bending resulting from its high WF, can lead to an energetic alignment which enhances hole extraction.<sup>100</sup> Despite this, an organic HTL with a low LUMO is still required for a complete electron blocking behaviour and for the proper growth of vacuum deposited perovskites in the P-i-N configuration, as we discussed in the previous chapter. A simplified band diagram of a MoO<sub>3</sub>/HTL junction is shown in figure 20. Here, the hole injection is mediated from a charge transfer between a hole from the HOMO of the organic material and an electron at the conduction band of the metal oxide, thus converting hole current into electron current. A photo-generated hole from the perovskite is transported through the HTL and recombines with the electron at the MoO<sub>3</sub> interface, acting as a charge recombination or buffer layer. For MoO<sub>3</sub> specifically, it has also been suggested a charge transport via sub-gap states under some circumstances<sup>61,94,101</sup> (figure 20, right). Some interfaces such as ITO/MoO<sub>3</sub> display a high density of gap states when thin layers are used, which can contribute to charge transport reducing the energy barrier for holes. These empty states can also be induced by annealing or by organic molecules through a chemical charge transfer at the interface inducing on them a P-doped character in exchange.<sup>102</sup>

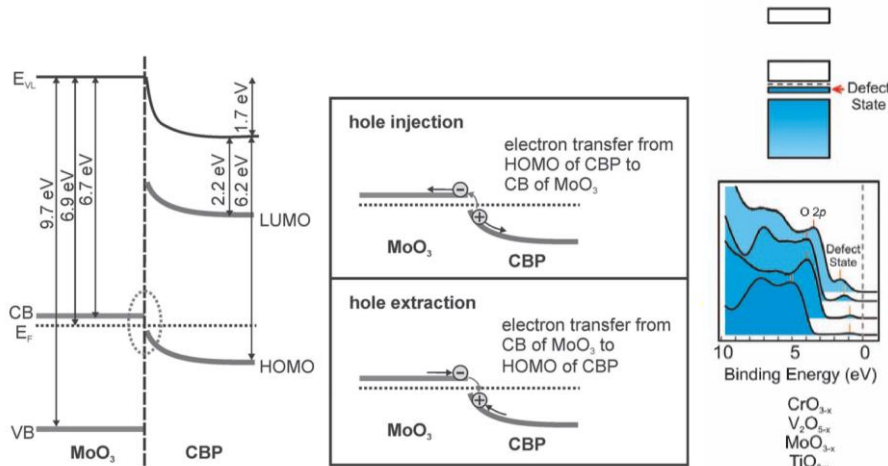


**Figure 20:** Energy level alignment and band bending between MoO<sub>3</sub> and an organic HTL and sub-gap defect states of MoO<sub>3</sub> (figures from references 102 and 92).

For these reasons, in this chapter I aim for the implementation of MoO<sub>3</sub> first on the P-i-N configuration and, once optimized, on the N-i-P stack developed in the previous chapter. By doing this, we achieved the first dual oxide configuration with high efficiencies on vacuum-deposited perovskite solar cells.

## 4.2 Experimental and methodology

The device structure for P-i-N is: ITO / MoO<sub>3</sub> (7 nm) / TaTm (10 nm) / CH<sub>3</sub>NH<sub>3</sub>PbI<sub>3</sub> (590 nm) / C<sub>60</sub> (25 nm) / BCP (7 nm) / Ag (100 nm) (figure 21, a).

In this architecture the MoO<sub>3</sub> layer acts as hole injection layer, TaTm as electron blocking layer, the perovskite is the photoactive material, C<sub>60</sub> is the hole blocking layer and BCP was found to be a proper electron injection layer when Ag is evaporated on top of it, following the trends in literature at that time. The thickness of the C<sub>60</sub> layer was increased from 10 to 25 nm compared to the N-i-P configuration in the previous chapter due to its high electron mobility and diffusion length, being less problematic the parasitic absorption role on the top side of the device.

A MoO<sub>3</sub> layer is sublimed on top of the ITO and then annealed at 100 °C for 10 minutes in nitrogen atmosphere in order to induce defects that will contribute to the hole transport. For the rest of the layers the experimental procedure and characterization is equal as the one described in the chapters 2 and 3.

For the N-i-P configuration the device structure is: ITO / TiO<sub>2</sub> (30 nm) / C<sub>60</sub> (10 nm) / CH<sub>3</sub>NH<sub>3</sub>PbI<sub>3</sub> (590 nm) / TaTm (10 nm) / TPBi (2 nm) / MoO<sub>3</sub> (7 nm) / Au (100 nm) (figure 23, a)

In this case the N side is equal to the one developed in the previous chapter. The doped TaTm is substituted for the combination of TPBi/MoO<sub>3</sub>, which is explained in the following section. In this case, C<sub>60</sub> thickness is kept at 10 nm to avoid parasitic absorption.

### 4.3 Results and discussion

Initially, we aimed for the substitution of the doped HTL for a metal oxide in the P-i-N architecture.  $\text{MoO}_3$  was a direct candidate due to its ease of deposition, proper band alignment, low parasitic absorption, and chemical stability. We found that a short annealing in nitrogen atmosphere was required after its deposition and prior to depositing the rest of the stack in order to achieve proper hole transport characteristics. The devices with the  $\text{MoO}_3$  layer annealed at 100 °C for 10 minutes showed an increase in FF and  $V_{oc}$  under illumination and current density at forward bias in the dark curve (Figure 21, b and c). Without annealing, the cells showed an energy barrier that was hindering the hole injection, thus increasing the recombination due to a charge accumulation, which led to lower  $V_{oc}$  and FF. This phenomenon has been previously reported, and it is attributed to the formation of defect states in the band gap of the  $\text{MoO}_3$  layer due to oxygen vacancies.<sup>101,103</sup> Although the annealing step is not a problem in the P-i-N configuration, if we want to implement this layer in N-i-P it might be negative for the already deposited layers. Therefore, we aimed for an alternative for the annealing step by depositing an interlayer between the  $\text{MoO}_3$  and the HTL. We used TPBi, a molecule with a HOMO level deep enough to pin the fermi level of the  $\text{MoO}_3$  with the HOMO of the TaTm which should improve the hole injection according to other works.<sup>104</sup> By using TPBi we reach almost the same performance as for the annealed sample, with the advantage of avoiding this treatment, reaching a PCE of 19% (table 3).

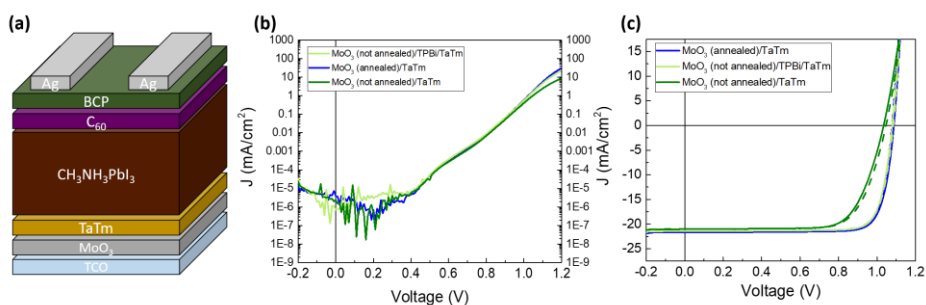


**Figure 21:** P-i-N device architecture (a), dark J-V curve in semilogarithmic scale (b) and illuminated J-V curve in linear scale (c) of devices comparing the effects of annealing and TPBi on the  $\text{MoO}_3$  layer.

**Table 3:** Average solar cell parameters for P-i-N solar cells with the MoO<sub>3</sub> layer at the front contact.

Samples	PCE (%)	V <sub>oc</sub> (V)	J <sub>sc</sub> (mA/cm <sup>2</sup> )	FF (%)
MoO <sub>3</sub> (not annealed)	15.8	1.034	21.0	73.0
MoO <sub>3</sub> (annealed)	19.3	1.077	21.7	82.5
MoO <sub>3</sub> (not annealed)/TPBi	19.0	1.080	21.4	82.0

We ascribe this improvement in performance not only to the deeper HOMO level of TPBi, but also to the presence of pyridinic nitrogen atoms, that are known to react with MoO<sub>3</sub> through a charge transfer from the lone electron pairs in the nitrogen, which would chemically induce the required gap states to improve the hole injection.<sup>105,106</sup> To proof this, we used other molecules without pyridinic nitrogen atoms but with a similar HOMO energy, which should also improve the band alignment and pin the Fermi level (figure 22). We found that these molecules also improve the FF and V<sub>oc</sub> but do not reach the same performance as the sample with annealing or the one with TPBi. This shows that, although the band alignment can contribute to reduce charge accumulation and recombination at the interface, the presence of MoO<sub>3</sub> sub-gap states, induced either chemically with TPBi or by annealing, remains very important to achieve higher FF values.

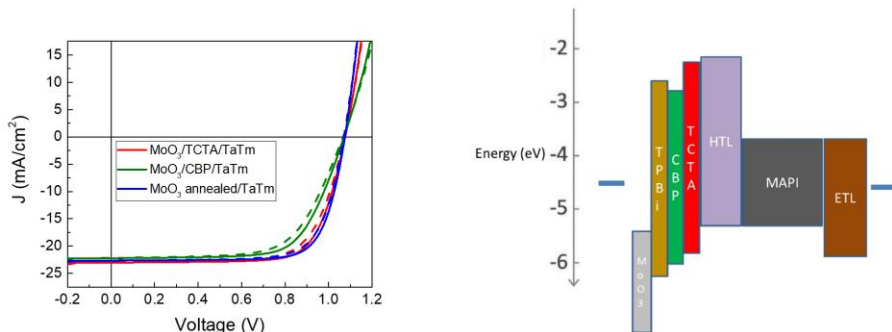


**Figure 22:** J-V curves under AM1.5G illumination and energy levels of P-i-N solar cells using molecules with different HOMO energies on top of MoO<sub>3</sub> not annealed. The sample of MoO<sub>3</sub> annealed works as a reference. Dashed lines stand for reverse scan.

Once we found a way to use  $\text{MoO}_3$  without annealing by chemical passivation, we implemented it into the N-i-P architecture developed in the previous chapter, leading to a double-oxide structure depicted in figure 23. The structure is ITO /  $\text{TiO}_2$  (50 nm) /  $\text{C}_{60}$  (10 nm) /  $\text{CH}_3\text{NH}_3\text{PbI}_3$  (590 nm) / TaTm (10 nm) / TPBi (0, 2 or 5 nm) /  $\text{MoO}_3$  (7 nm) / Au (100 nm). When TPBi is not present we observe a different behaviour than in P-i-N. Although here the hole injection is not hindered, there is an increase in charge carrier recombination, with the subsequent reduction in  $V_{oc}$ . This is attributed to the infiltration of  $\text{MoO}_3$  into TaTm, reducing its electron-blocking behaviour (figure 23, b). The high kinetic energy of  $\text{MoO}_3$  sublimed onto soft organic molecules enhances its diffusion into the organic material, inducing a P-doping by forming charge transfer states.<sup>107</sup> Interestingly, when we incorporated a 2 nm thick layer of TPBi onto the TaTm, this penetration is prevented. As a result, solar cells based on this stack present a full recovery in  $V_{oc}$  while maintaining a high FF, leading to more than 18% PCE. Increasing the thickness of TPBi to 5 nm completely hinders the charge transport, reducing the FF due to a series resistance enhancement (table 4 and figure 23, c). This strong dependence between the conductivity and TPBi thickness indicates that  $\text{MoO}_3$  interacts only with the surface of the layer and does not penetrate beyond, emerging the insulating behaviour of TPBi when its thickness is higher than 2 nm.

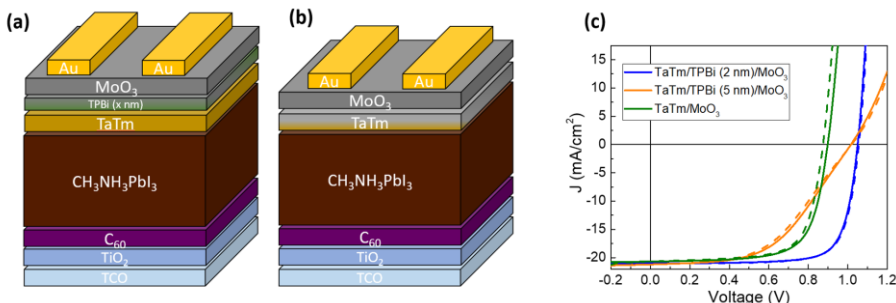


**Figure 23:** Schematic device architectures of n-i-p devices with (a) and without (b) TPBi interlayer. (c) J-V curves under AM1.5G illumination corresponding to devices with 0, 2, and 5 nm-thick TPBi interlayers. Dashed lines stand for reverse scan.

**Table 4:** Average PV parameters of N-i-P solar cells with  $\text{MoO}_3$  on top of TaTm and on top of TaTm/TPBi.

Sample	PCE (%)	$V_{oc}$ (V)	$J_{sc}$ (mA/cm <sup>2</sup> )	FF (%)
TaTm/ $\text{MoO}_3$	13.0	0.898	20.7	70.0
TaTm/TPBi (2 nm)/ $\text{MoO}_3$	18.8	1.084	21.3	81.4
TaTm/TPBi (5 nm)/ $\text{MoO}_3$	11.0	1.015	21.2	51.0

To demonstrate this protective behaviour based on the chemical interaction of TPBi and  $\text{MoO}_3$  we performed 2 experiments, explained in detail in the complete publication after this section. In the first experiment, the total thickness of TaTm was varied from 12 to 25 nm instead of using 10 nm of TaTm + 2 nm of TPBi. At least 20 nm were required to compensate the effect of the  $\text{MoO}_3$  diffusion, showing that the protection of TPBi is not coming from just the increase in total thickness. Secondly, to proof that the protective behaviour is coming from the pyridinic nitrogen atoms, we deposited on top of TaTm two molecules that are similar to TPBi in terms of energy levels, BCP (2,9-Dimethyl-4,7-diphenyl-1,10-phenanthroline) and TCTA (Tris(4-carbazoyl-9-ylphenyl)amine), where the first one has the same characteristic nitrogen chemistry, but the latter does not (figure 24, right). Again, depositing just 2 nm of BCP on top of TaTm was enough to protect it from the diffusion of  $\text{MoO}_3$ , reproducing the best photovoltaic results obtained with the TPBi. In contrast, cells with 2 nm of TCTA still showed an increased recombination, slightly reduced by the increased thickness, but confirming the importance of the molecule's chemistry (figure 24 and table 5).

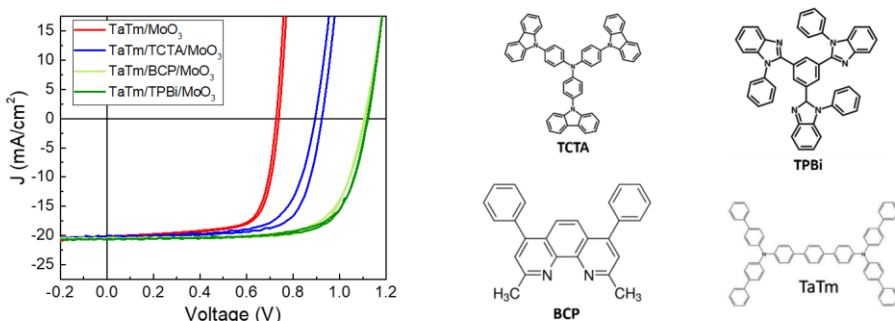


**Figure 24:** J-V curves of N-i-P solar cells under AM1.5G illumination with different molecules on top of TaTm and their chemical structures.

**Table 5:** Photovoltaic parameters of N-i-P solar cells with different interlayers between TaTm and MoO<sub>3</sub>.

Sample	PCE (%)	V <sub>oc</sub> (V)	J <sub>sc</sub> (mA/cm <sup>2</sup> )	FF (%)
TaTm/MoO <sub>3</sub>	10.7	0.727	20.1	73.0
TaTm/TCTA/MoO <sub>3</sub>	13.6	0.920	20.3	72.5
TaTm/BCP/MoO <sub>3</sub>	16.7	1.106	20.4	74.0
TaTm/TPBi/MoO <sub>3</sub>	17.2	1.121	20.5	75.0

#### 4.4 Conclusions

In conclusion, the insertion of an ultrathin layer of a molecule with high IE and pyridinic nitrogen atoms permits the use of MoO<sub>3</sub> as hole injection layer in the P-i-N structure without requiring an annealing step. This molecule chemically induces the charge states needed for hole injection/extraction and its deep HOMO level causes a band bending and Fermi level pinning that improves the band alignment between MoO<sub>3</sub> and TaTm. When using MoO<sub>3</sub> in the N-i-P configuration a different case is observed. The high kinetic energy of MoO<sub>3</sub> clusters causes the penetration into TaTm reducing its electron blocking character and increases the charge carrier recombination. Using just 2 nm of TPBi is enough to achieve a full protection of the underlying layers by forming a TPBi-MoO<sub>3</sub> surface species that stops the further diffusion of the metal oxide, leading to a double oxide architecture with PCEs close to 19%, the highest reported for vacuum deposited CH<sub>3</sub>NH<sub>3</sub>PbI<sub>3</sub> solar cells employing a double oxide structure.

## 4.5 Contribution of the author

The work developed in this chapter was entirely carried out in the Molecular Science Institute (ICMol) from the University of Valencia. The author developed the main experiments and characterization steps, along with the writing of the manuscript.

**Daniel Pérez-del-Rey**, Lidón Gil-Escríg, Kassio P. S. Zanoni, Chris Dreessen, Michele Sessolo, Pablo P. Boix, and Henk J. Bolink. “Molecular Passivation of MoO<sub>3</sub>: Band Alignment and Protection of Charge Transport Layers in Vacuum-Deposited Perovskite Solar Cells” *Chem. Mater.* 2019, 31, 17, 6945–6949.

## Molecular Passivation of $\text{MoO}_3$ : Band Alignment and Protection of Charge Transport Layers in Vacuum-Deposited Perovskite Solar Cells

Daniel Pérez-del-Rey,<sup>†</sup> Lidón Gil-Escríg,<sup>‡</sup> Kassio P. S. Zanoni,<sup>†,§</sup> Chris Dreessen,<sup>†</sup> Michele Sessolo,<sup>†,¶</sup> Pablo P. Boix,<sup>\*,†,||</sup> and Henk J. Bolink<sup>\*,†,¶</sup>

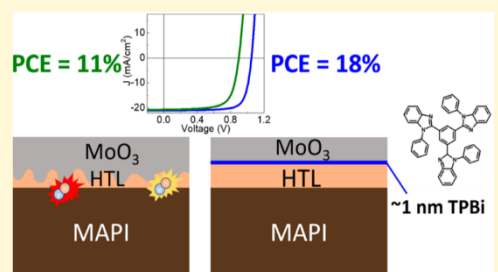
<sup>†</sup>Instituto de Ciencia Molecular, Universidad de Valencia, C/Catedrático J. Beltrán 2, 46980 Paterna, Spain

<sup>‡</sup>Helmholtz-Zentrum Berlin für Materialien und Energie GmbH, Kekuléstraße 5, 12489 Berlin, Germany

<sup>§</sup>Istituto de Física de São Carlos, Universidade de São Paulo, Av. Trab. São Carlense 400, 13566 São Carlos, Brazil

### Supporting Information

**ABSTRACT:** Vacuum deposition of perovskite solar cells can achieve efficiencies rivaling solution-based methods and allows for more complex device stacks.  $\text{MoO}_3$  has been used to enhance carrier extraction to the transparent bottom electrode in a p-i-n configuration; here, we show that by inserting an molecular interlayer with a lone pair nitrogen atom and low ionization potential, it can also be used on the top of a perovskite absorber in a n-i-p configuration. This strategy enables the first vacuum-deposited perovskite solar cells with metal oxides as charge transporting layers for both electrons and holes, leading to power conversion efficiency >19%.



### 1. INTRODUCTION

Halide perovskites have a wide range of chemical and physical properties that make them suitable for new generation photovoltaics.<sup>1</sup> These encompass long charge carrier diffusion lengths<sup>2</sup> and high absorption coefficients.<sup>3</sup> Furthermore, their compositional flexibility allows fine-tuning of the photophysical properties.<sup>4,5</sup> The use of perovskites in high efficiency devices requires directing charge carriers to the appropriate electrode. This is generally achieved by placing selective charge transport layers below and above the perovskite layer. Interfaces between the perovskite and the charge extraction material and between the charge extraction material and the electrodes are thus crucial for an efficient charge carrier collection.<sup>6</sup> In this aspect, perovskite-based solar cells can have two main device architectures depending on whether the photogenerated holes are extracted through the light incident side and photogenerated electrons extracted through the metal side (p-i-n) or vice versa (n-i-p), just by changing the deposition order of the transport layers.

Vacuum deposition is a widely adopted technique in the industry with proven scalability capabilities. More interestingly for perovskite optoelectronics, it is a solvent-free process, making it more environmentally friendly.<sup>7</sup> Vacuum processing also allows for an accurate control on multiple-layer stacks.<sup>8</sup> Vacuum-deposited high efficiency solar cells generally rely on a combination of intrinsic organic materials as charge selective layers and doped materials as charge transport/extraction

layers to ensure that the photogenerated charge carriers are efficiently extracted to an external circuit.<sup>9</sup>

Semiconducting metal oxides are widely studied in solution-processed perovskite devices and have also been recently applied as charge transport layers in highly efficient vacuum-deposited perovskite solar cells.<sup>10</sup> The use of  $\text{TiO}_2$  in n-i-p structure instead of doped  $\text{C}_{60}$  reduces parasitical absorption and has a positive impact on device stability and material costs.<sup>10</sup> However, the system still relies on organic doped materials as hole transport layer (HTL) in the top contact with the associated complexity and stability-related issues. Hence, it is important to find metal oxide alternatives that can reduce parasitic absorption in p-i-n devices and can be incorporated to a n-i-p stack without compromising the rest of the deposited layers.

Molybdenum(VI) oxide ( $\text{MoO}_3$ ) has been recurrently employed as hole injection/extraction layers in organic light-emitting diodes (OLEDs)<sup>11</sup> and in organic, quantum dot, and perovskite solar cells<sup>12,13</sup> due to its very deep work function and low-lying conduction band.<sup>14</sup>  $\text{MoO}_3$  has the advantage of creating an optimal ohmic contact with ITO. Its protective effect against moisture when used in this architecture has also been reported.<sup>15</sup> Together with its low parasitic absorption and

Special Issue: Jean-Luc Bredas Festschrift

Received: April 9, 2019

Revised: June 3, 2019

Published: June 4, 2019

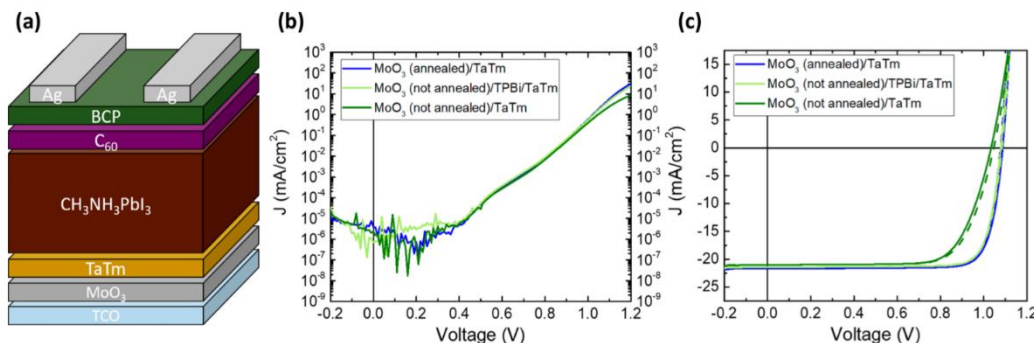


**Figure 1.** (a) Schematic device architecture, (b) dark and (c) illuminated  $J$ – $V$  curves (AM1.5G) of p-i-n devices according to panel a for three different hole extraction architectures: MoO<sub>3</sub> (not annealed)/TaTm, MoO<sub>3</sub> (annealed)/TaTm, and MoO<sub>3</sub> (not annealed)/TPBi/TaTm. Dashed lines in panel c stand for reverse scan.

the possibility of being sublimed, it appears to be a good candidate for use as a hole extraction material in our system. However, the low selectivity of MoO<sub>3</sub> requires it to be used in combination with more selective contacts.

Here, we developed a method to modify the MoO<sub>3</sub>/electron blocking layer interface, obtaining an improved ohmic contact suitable for p-i-n configuration, yet with the advantage of avoiding any annealing step. In the n-i-p structure, this interfacial modification also acts as a protection layer which prevents MoO<sub>3</sub> diffusion into the underlying layers. As a result, we fabricated the first high efficiency vacuum-deposited perovskite solar cell with both charge extraction layers based on metal oxides.

## 2. EXPERIMENTAL METHODS

Photolithographically patterned ITO coated glass substrates were purchased from Naranjo Substrates. N4,N4,N4',N4'-tetra-[1,1'-biphenyl]-4-yl)-[1,1':4',1'-terphenyl]-4,4'-diamine (TaTm) was provided by Novaled GmbH. TiO<sub>2</sub> nanoparticle suspensions were prepared in IMEC as previously reported.<sup>10</sup> Fullerene (C<sub>60</sub>) was purchased from Sigma Aldrich. PbI<sub>2</sub> was purchased from Tokyo Chemical Industry CO (TCI), while CH<sub>3</sub>NH<sub>3</sub>I (MAI), MoO<sub>3</sub>, and bathocuproine (BCP) were purchased from Lumtec.

ITO prepatterned substrates were cleaned following a standard procedure in which they are cleaned with soap, water, deionized water, and isopropanol in a sonication bath, followed by UV treatment for 20 min. The TiO<sub>2</sub> dispersion was deposited in air by spin-coating at 3000 rpm for 30 s and annealed at 100 °C for 30 min, leading to a 50–80 nm-thick compact layer. For the deposition of the other materials through vacuum deposition, the samples were transferred to a vacuum chamber integrated into a nitrogen-filled glovebox (H<sub>2</sub>O and O<sub>2</sub> < 0.1 ppm) and evacuated to a pressure of 10<sup>-6</sup> mbar. The vacuum chamber was equipped with six temperature-controlled evaporation sources (Creaphys) fitted with ceramic crucibles. The sources were directed upward with an angle of approximately 90° with respect to the bottom of the evaporator. The substrate holder to evaporation source distance was approximately 20 cm. Three quartz crystal microbalance (QCM) sensors were used: two monitoring the deposition rate of each evaporation source and a third one close to the substrate holder monitoring the total deposition rate. For thickness calibration, we individually sublimed the charge transport materials. A calibration factor was obtained by comparing the thickness inferred from the QCM sensors with that measured with a mechanical profilometer (Ambios XP1). Then, the materials were sublimed at temperatures ranging from 60 to >300 °C, and the evaporation rate was controlled by separate QCM sensors obtaining precisely the deposited thickness. In general, the deposition rate for

TaTm and C<sub>60</sub> was 0.5 Å s<sup>-1</sup> and 0.2–0.3 Å s<sup>-1</sup> for the thinner BCP, TPBi, CBP, and TCTA layers. For the perovskite deposition, MAI and PbI<sub>2</sub> were coevaporated by measuring the deposition rate of each material in a different sensor and obtaining the total perovskite thickness in a third one, leading to a 590 nm-thick perovskite. MoO<sub>3</sub>, Ag, and Au were evaporated in a second vacuum chamber using aluminum boats as sources by applying currents ranging from 2.0 to 4.5 Å. For the solar cell characterization, the  $J$ – $V$  characteristics were obtained using a solar simulator by Abet Technologies (model 10500 with an AM1.5G xenon lamp as the light source). Before each measurement, the exact light intensity was determined using a calibrated Si reference diode equipped with an infrared cutoff filter (KG-3, Schott). The  $J$ – $V$  curves were recorded between −0.2 and 1.2 V with 0.01 V steps, integrating the signal for 20 ms after a 10 ms delay. This corresponds to a speed of about 0.3 V s<sup>-1</sup>. The layout used to test the solar cells has four equal areas (0.0651 cm<sup>2</sup>, defined as the overlap between the ITO and the top metal contact) and measured through a shadow mask with 0.0264 cm<sup>2</sup> aperture. Absorption spectra were collected using a fiber optics-based Avantes Avaspec2048 Spectrometer. The work functions were determined by Kelvin probe measurements using an Ambient Pressure Photoemission Spectroscopy system from KP Technology.

## 3. RESULTS

To evaluate the overall capability of MoO<sub>3</sub> as a hole extraction layer, the following p-i-n configuration was selected as it is similar to a previously tested one with an organic charge extraction material (F<sub>6</sub>TCNNQ):<sup>9</sup> ITO/MoO<sub>3</sub> (7 nm)/TaTm (10 nm)/CH<sub>3</sub>NH<sub>3</sub>PbI<sub>3</sub> (590 nm)/C<sub>60</sub> (25 nm)/BCP (7 nm)/Ag, as represented in Figure 1.

In Figure 1b and 1c, respectively, the typical current–voltage curves in the dark and under AM1.5G are depicted for three different hole extraction layers. The devices with nonannealed (as deposited) MoO<sub>3</sub> show a high short circuit current density,  $J_{sc}$  (21 mA/cm<sup>2</sup>), a reasonable open circuit voltage,  $V_{oc}$  (1.03 V), but a rather poor fill factor, FF (73%). This may be due to either a low layer conductivity, to an energy level mismatch with the electron blocking material, or to a combination of both. It has been reported that annealing the MoO<sub>3</sub> layer increases the amount of oxygen vacancies and creates gap states which can contribute to the charge transport through a shift in the Fermi level.<sup>16,17</sup> We also find that an annealing process of the MoO<sub>3</sub> layers for 10 min at 100 °C in nitrogen leads to an increase in FF and also in  $J_{sc}$  and  $V_{oc}$  values. This is most likely the result of the work function (WF) closer to the vacuum level, as shown in Figure S1. Despite the higher power

conversion efficiencies obtained, the temperature requirement for this annealing step is undesired. Therefore, we also considered an alternative approach to interfacial tuning by adding an interlayer with a lower ionization energy (IE) than the WF of the  $\text{MoO}_3$ , as was recently reported for similar devices.<sup>18</sup> We used 2,2',2''-(1,3,5-benzenetriyl)-tris(1-phenyl-1-H-benzimidazole) (TPBi) in a 2 nm thin interlayer between the not annealed  $\text{MoO}_3$  and the hole transport/electron blocking molecule TaTm. These devices have performance very similar to that in the device with the annealed  $\text{MoO}_3$  (Figure 1 and Table 1). The insertion of this interlayer is confirmed by contact angle measurements and does not lead to additional absorption (Figures S2 and S3).

**Table 1.** Average Solar Cell Parameters for p-i-n Solar Cells with the  $\text{MoO}_3$  Layer at the Front Contact

samples	PCE (%)	$V_{oc}$ (V)	$J_{sc}$ ( $\text{mA}/\text{cm}^2$ )	FF (%)
$\text{MoO}_3$ (not annealed)	15.8	1.034	21.0	73.0
$\text{MoO}_3$ (annealed)	19.3	1.077	21.7	82.5
$\text{MoO}_3$ (not annealed)/TPBi	19.0	1.080	21.4	82.0

Some other molecules were also sublimed and evaluated as interlayers in between not annealed  $\text{MoO}_3$  and TaTm, namely, TCTA (tris(4-carbazoyl-9-ylphenyl)amine) and CBP (4,4'-bis(*N*-carbazolyl)-1,1'-biphenyl). These molecular layers also improve the device behavior but not to the extent that  $\text{MoO}_3$  annealing or TPBi insertion does (Figure S4), which is in agreement with a lower difference between their IE (CBP = 6.0 eV and  $\text{TcTa} = 5.7$  eV) and the HOMO level of TaTm, as was discussed also in ref 18.

Because the TPBi interlayer enables the use of  $\text{MoO}_3$  as hole extraction layer without the need for its annealing, this extraction layer can now be directly implemented in a n-i-p structure with both contacts based on metal oxides. The chosen device structure for the n-i-p devices is  $\text{TiO}_2$  (50–80 nm)/ $\text{C}_{60}$  (10 nm)/ $\text{CH}_3\text{NH}_3\text{PbI}_3$  (590 nm)/TaTm (10 nm)/(TPBi 2 nm, optional)/ $\text{MoO}_3$  (5 nm)/Au (Figures 2a and 2b).

In Figure 2c, the typical current–voltage curves in the dark and under AM1.5G are depicted for the n-i-p devices with three different hole extraction layers, and the parameters are listed in Table 2. The devices with TaTm and the not annealed (as deposited)  $\text{MoO}_3$  show a rather low  $V_{oc}$  but a decent FF.

**Table 2.** Average PV Parameters of n-i-p Solar Cells with  $\text{MoO}_3$  on Top of TaTm and TaTm/TPBi

sample	PCE (%)	$V_{oc}$ (V)	$J_{sc}$ ( $\text{mA}/\text{cm}^2$ )	FF (%)
TaTm/ $\text{MoO}_3$	13.0	0.898	20.7	70.0
TaTm/TPBi (2 nm)/ $\text{MoO}_3$	18.8	1.084	21.3	81.4
TaTm/TPBi (5 nm)/ $\text{MoO}_3$	11.0	1.015	21.2	51.0

This is most likely due to diffusion of  $\text{MoO}_3$  into TaTm, as previously reported for various organic materials.<sup>19</sup> While this diffusion of  $\text{MoO}_3$  has the potential to improve the band alignment without further annealing, it can also significantly increase recombination losses due to the partial or complete oxidation of the TaTm electron blocking layer. The much higher dark current (hence, high conductivity) observed for the TaTm/ $\text{MoO}_3$  containing device compared to the one with the TPBi thin interlayer (see Figure S5a) is in agreement with this hypothesis. Such a reduced electron blocking and hence increased charge recombination would indeed lead to a lower  $V_{oc}$  without affecting the FF too much, as we observe. The device with a 2 nm TPBi interlayer in between the TaTm layer and the  $\text{MoO}_3$  layer shows very good performance with high  $V_{oc}$ ,  $J_{sc}$ , and FF, leading to a power conversion efficiency of almost 19%. Although a similarly thin layer of TPBi also improved the performance of the p-i-n devices, it is rather surprising that such a thin layer is preventing the diffusion of  $\text{MoO}_3$  into the TaTm layer. Therefore, we also prepared a similar device but now with a slightly thicker TPBi layer of 5 nm. In these devices, the  $V_{oc}$  is similar to what is observed for the device with a 2 nm layer, but the FF is much worse, indicating a significant extraction barrier due to a strong increase in the series resistance. This seems to indicate that the  $\text{MoO}_3$  interacts only with the surface of the TPBi layer, as intrinsic TPBi is a poor hole transporter and undoped TPBi needs to be very thin to effectively tunnel holes through. To verify if  $\text{MoO}_3$  diffusion and the accompanied reduction in electron blocking behavior can also be reduced by using thicker TaTm layers, such devices were prepared as well. In these solar cells, the  $V_{oc}$  recovers, as displayed in Figure S5b. However, the  $\text{MoO}_3$  diffusion is a sensitive process and difficult to control, and thicker TaTm n-i-p solar cells suffer from poorer reproducibility and larger parasitic absorption. To evaluate this TPBi interaction with  $\text{MoO}_3$ , we substituted TPBi

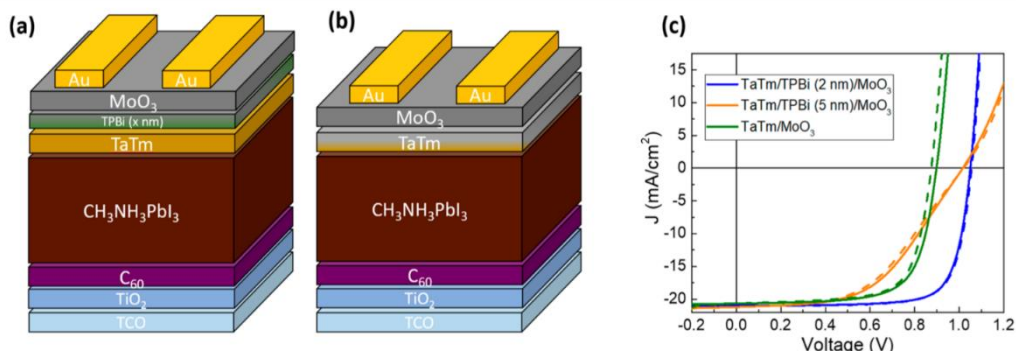


**Figure 2.** Schematic device architectures of n-i-p devices with (a) and without (b) TPBi interlayer. (c)  $J$ – $V$  curves under AM1.5G illumination corresponding to devices with 0, 1, and 5 nm-thick TPBi interlayers. Dashed lines stand for reverse scan.

with TCTA. As in the p-i-p devices, it leads to similar device performance (Figure S4). However, in the n-i-p configuration, devices with a 2 nm-thick TCTA interlayer have low  $V_{oc}$  values similar to the TPBi-free devices, which is attributed to the diffusion of MoO<sub>3</sub> into both TCTA and TaTm, increasing recombination and reducing the  $V_{oc}$  (Figure S6). The molecular weights of TCTA and TPBi are very similar, and therefore, it is unlikely that this is the reason for the observed difference in device performance. The reactivity of MoO<sub>3</sub> with organic compounds is well-known, particularly with a variety of pyridine-like nitrogen atoms with a lone pair such as bipyridine, where the ligand passivates MoO<sub>3</sub> surface and blocks further Mo–oxo bond formation or with triazole family molecules forming a different layered structure.<sup>20,21</sup> TPBi contains a lone pair which may lead to chemical modification of the MoO<sub>3</sub> surface, creating possibly the before mentioned oxygen vacancies that contribute to the charge transport, as other works have shown with pyridine-like nitrogen atoms.<sup>17,20,22</sup> For this reason, a 2 nm layer of bathocuproine (BCP, 2,9-dimethyl-4,7-diphenyl-1,10-phenanthroline) was also inserted in the n-i-p device stack. The performance of the resulting solar cells is very similar as in the case of the TPBi interlayers (Figure S6), indicating that there is an interaction between MoO<sub>3</sub> and these lone pair nitrogen containing molecules that prevents the diffusion of MoO<sub>3</sub>.

Considering both the p-i-n and n-i-p results, we hypothesize that TPBi reacts with the MoO<sub>3</sub> surface through an electron transfer, facilitating the charge transport. Not only that, but also this TPBi-MoO<sub>3</sub> surface species protects TaTm in the inverted structure from the diffusion of MoO<sub>3</sub> by forming a passivation layer, which makes it possible to use this material in n-i-p configuration without compromising the performance or reproducibility of the device.

#### 4. CONCLUSIONS

In conclusion, the insertion of a thin layer of a wide bandgap conjugated molecule containing lone pair nitrogen atoms leads to efficient hole extraction in p-i-n and n-i-p architectures, in part due to the decoupling of the dipole moment and additionally preventing evaporation damage of MoO<sub>3</sub> on the organic charge transporting molecules. The efficient charge extraction and resulting device efficiency in the n-i-p configuration is particularly promising as it can be used in tandem cells and low temperature demanding substrates.

#### ■ ASSOCIATED CONTENT

##### § Supporting Information

The Supporting Information is available free of charge on the ACS Publications website at DOI: [10.1021/acs.chemmater.9b01396](https://doi.org/10.1021/acs.chemmater.9b01396).

Kelvin probe and contact angle measurements of the MoO<sub>3</sub> films with and without TPBi and device data with alternative interfacial molecules ([PDF](#))

#### ■ AUTHOR INFORMATION

##### Corresponding Authors

\*E-mail: [Pablo.P.Boix@uv.es](mailto:Pablo.P.Boix@uv.es).

\*E-mail: [henk.bolink@uv.es](mailto:henk.bolink@uv.es).

##### ORCID

Kassio P. S. Zanoni: [0000-0003-4586-6126](https://orcid.org/0000-0003-4586-6126)

Michele Sessolo: [0000-0002-9189-3005](https://orcid.org/0000-0002-9189-3005)

Pablo P. Boix: [0000-0001-9518-7549](https://orcid.org/0000-0001-9518-7549)

Henk J. Bolink: [0000-0001-9784-6253](https://orcid.org/0000-0001-9784-6253)

#### Notes

The authors declare no competing financial interest.

#### ■ ACKNOWLEDGMENTS

The authors would like to thank Alicia Forment for the contact angle measurements. Financial support is acknowledged from the Spanish Ministry of Economy and Competitiveness (MINECO) via the Unidad de Excelencia María de Maeztu MDM-2015-0538, MAT2017-88821-R, PCIN-2015-255, PCIN-2017-014, and the Generalitat Valenciana (Prometeo/2016/135). K.P.S.Z. acknowledges the financial support from Fundação de Amparo à Pesquisa do Estado de São Paulo (FAPESP 2018/05152-7). P.B. and M.S. thank the MINECO for their RyC contracts. P.B. acknowledges the financial support from the Conselleria d'Educació, Investigació, Cultura i Esport Valenciana (SEJ12017/2017/012).

#### ■ REFERENCES

- (1) Xu, W.; Cho, H.; Kim, Y.-H.; Kim, Y.-T.; Wolf, C.; Park, C.-G.; Lee, T.-W. Organometal Halide Perovskite Artificial Synapses. *Adv. Mater.* **2016**, *28* (28), 5916–5922.
- (2) Shi, D.; Adinolfi, V.; Comin, R.; Yuan, M.; Alarousu, E.; Buin, A.; Chen, Y.; Hoogland, S.; Rothenberger, A.; Katsiev, K.; et al. Low Trap-State Density and Long Carrier Diffusion in Organolead Trihalide Perovskite Single Crystals. *Science (Washington, DC, U. S.)* **2015**, *347* (6221), 519–522.
- (3) De Wolf, S.; Holovsky, J.; Moon, S.-J.; Löper, P.; Niesen, B.; Ledinsky, M.; Haug, F.-J.; Yum, J.-H.; Ballif, C. Organometallic Halide Perovskites: Sharp Optical Absorption Edge and Its Relation to Photovoltaic Performance. *J. Phys. Chem. Lett.* **2014**, *5* (6), 1035–1039.
- (4) Cheetham, A. K.; Rao, C. N. R.; Feller, R. K. Structural Diversity and Chemical Trends in Hybrid Inorganic/Organic Framework Materials. *Chem. Commun.* **2006**, No. 46, 4780.
- (5) Li, W.; Wang, Z.; Deschler, F.; Gao, S.; Friend, R. H.; Cheetham, A. K. Chemically Diverse and Multifunctional Hybrid Organic-Inorganic Perovskites. *Nat. Rev. Mater.* **2017**, *2* (3), 16099.
- (6) Fakhruddin, A.; Schmidt-Mende, L.; Garcia-Belmonte, G.; Jose, R.; Mora-Sero, I. Interfaces in Perovskite Solar Cells. *Adv. Energy Mater.* **2017**, *7* (22), 1700623.
- (7) Ávila, J.; Momblona, C.; Boix, P. P.; Sessolo, M.; Bolink, H. J. Vapor-Deposited Perovskites: The Route to High-Performance Solar Cell Production? *Joule* **2017**, *1* (3), 431–442.
- (8) Ávila, J.; Momblona, C.; Boix, P.; Sessolo, M.; Anaya, M.; Lozano, G.; Vandewal, K.; Míguez, H.; Bolink, H. J. High Voltage Vacuum-Deposited CH 3 NH 3 PbI 3 – CH 3 NH 3 PbI 3 Tandem Solar Cells. *Energy Environ. Sci.* **2018**, *11* (11), 3292–3297.
- (9) Momblona, C.; Gil-Escríg, L. L.; Bandiello, E.; Sessolo, M.; Hutter, E. M.; Lederer, K.; Blochwitz-Nimoth, J. B.-N.; Bolink, H. J.; et al. Efficient Vacuum Deposited P-i-n and n-i-p Perovskite Solar Cells Employing Doped Charge Transport Layers. *Energy Environ. Sci.* **2016**, *9* (11), 3456–3463.
- (10) Pérez-del-Rey, D.; Boix, P. P.; Sessolo, M.; Hadipour, A.; Bolink, H. J. Interfacial Modification for High-Efficiency Vapor-Phase-Deposited Perovskite Solar Cells Based on a Metal Oxide Buffer Layer. *J. Phys. Chem. Lett.* **2018**, *9* (5), 1041–1046.
- (11) You, H.; Dai, Y.; Zhang, Z.; Ma, D. Improved Performances of Organic Light-Emitting Diodes with Metal Oxide as Anode Buffer. *J. Appl. Phys.* **2007**, *101* (2), 26105.
- (12) Shrotriya, V.; Li, G.; Yao, Y.; Chu, C.-W.; Yang, Y. Transition Metal Oxides as the Buffer Layer for Polymer Photovoltaic Cells. *Appl. Phys. Lett.* **2006**, *88* (7), 73508.
- (13) Gao, J.; Perkins, C. L.; Luther, J. M.; Hanna, M. C.; Chen, H.-Y.; Semonin, O. E.; Nozik, A. J.; Ellingson, R. J.; Beard, M. C. N-Type

- Transition Metal Oxide as a Hole Extraction Layer in PbS Quantum Dot Solar Cells. *Nano Lett.* **2011**, *11* (8), 3263–3266.
- (14) Meyer, J.; Hamwi, S.; Kröger, M.; Kowalsky, W.; Riedl, T.; Kahn, A. Transition Metal Oxides for Organic Electronics: Energetics, Device Physics and Applications. *Adv. Mater.* **2012**, *24* (40), 5408–5427.
- (15) Sanehira, E. M.; Tremolet de Villers, B. J.; Schulz, P.; Reese, M. O.; Ferrere, S.; Zhu, K.; Lin, L. Y.; Berry, J. J.; Luther, J. M. Influence of Electrode Interfaces on the Stability of Perovskite Solar Cells: Reduced Degradation Using MoO<sub>x</sub>/Al for Hole Collection. *ACS Energy Lett.* **2016**, *1* (1), 38–45.
- (16) Dasgupta, B.; Goh, W. P.; Ooi, Z. E.; Wong, L. M.; Jiang, C. Y.; Ren, Y.; Tok, E. S.; Pan, J.; Zhang, J.; Chiam, S. Y. Enhanced Extraction Rates through Gap States of Molybdenum Oxide Anode Buffer. *J. Phys. Chem. C* **2013**, *117* (18), 9206–9211.
- (17) Greiner, M. T.; Helander, M. G.; Tang, W.-M.; Wang, Z.-B.; Qiu, J.; Lu, Z.-H. Universal Energy-Level Alignment of Molecules on Metal Oxides. *Nat. Mater.* **2012**, *11*, 76.
- (18) Kotadiya, N. B.; Lu, H.; Mondal, A.; Ie, Y.; Andrienko, D.; Blom, P. W. M.; Wetzelaer, G.-J. A. H. Publisher Correction: Universal Strategy for Ohmic Hole Injection into Organic Semiconductors with High Ionization Energies. *Nat. Mater.* **2018**, *17* (6), 563.
- (19) White, R. T.; Thibau, E. S.; Lu, Z.-H. Interface Structure of MoO<sub>3</sub> on Organic Semiconductors. *Sci. Rep.* **2016**, *6*, 21109.
- (20) Zapf, P. J.; Haushalter, R. C.; Zubietta, J. Hydrothermal Synthesis and Structural Characterization of a Series of One-Dimensional Organic/Inorganic Hybrid Materials of the [(MoO<sub>3</sub>)-n(2,2'-Bipy)m] Family: [MoO<sub>3</sub>(2,2'-Bipy)], [Mo<sub>2</sub>O<sub>6</sub>(2,2'-Bipy)], and [Mo<sub>3</sub>O<sub>9</sub>(2,2'-Bipy)]<sub>2</sub>. *Chem. Mater.* **1997**, *9* (9), 2019–2024.
- (21) Hagman, P. J.; LaDuka, R. L.; Koo, H.-J.; Rarig, R.; Haushalter, R. C.; Whangbo, M.-H.; Zubietta, J. Ligand Influences on the Structures of Molybdenum Oxide Networks. *Inorg. Chem.* **2000**, *39* (19), 4311–4317.
- (22) Vasilopoulou, M.; Douvas, A. M.; Georgiadou, D. G.; Palilis, L. C.; Kennou, S.; Sygellou, L.; Soultati, A.; Kostis, I.; Papadimitropoulos, G.; Davazoglou, D.; et al. The Influence of Hydrogenation and Oxygen Vacancies on Molybdenum Oxides Work Function and Gap States for Application in Organic Optoelectronics. *J. Am. Chem. Soc.* **2012**, *134* (39), 16178–16187.

*Supporting Information*

## Molecular Passivation of MoO<sub>3</sub>: Band Alignment and Protection of Charge Transport Layers in Vacuum-Deposited Perovskite Solar Cells

Daniel Pérez-del-Rey<sup>1</sup>, Lidón Gil-Escrig<sup>2</sup>, Kassio P.S. Zanoni<sup>1,3</sup>, Chris Dreessen<sup>1</sup>, Michele Sessolo<sup>1</sup>, Pablo P. Boix<sup>1,\*</sup>, Henk J. Bolink<sup>1,\*</sup>

<sup>1</sup>Instituto de Ciencia Molecular, Universidad de Valencia, C/ Catedrático J. Beltrán 2, 46980 Paterna, Spain

<sup>2</sup>Helmholtz-Zentrum Berlin für Materialien und Energie GmbH, Kekuléstraße 5, 12489 Berlin, Germany

<sup>3</sup>Istituto de Física de São Carlos, Universidade de São Paulo, Av. Trab. São Carlense 400, 13566 São Carlos, Brazil

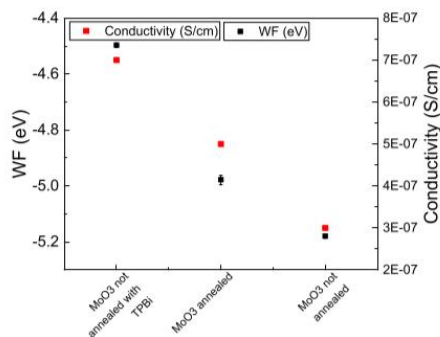


Figure S1. Work function (measured by Kelvin probe) and conductivity of MoO<sub>3</sub> thin films in different conditions.

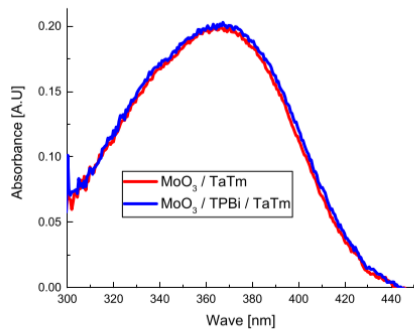


Figure S2. Absorption spectra of MoO<sub>3</sub>/TaTm layers with and without a TPBi interlayer.



Figure S3. Contact angle measurements of a MoO<sub>3</sub> thin film (left) and a MoO<sub>3</sub> thin film with 2 nm of TPBi on top (right).

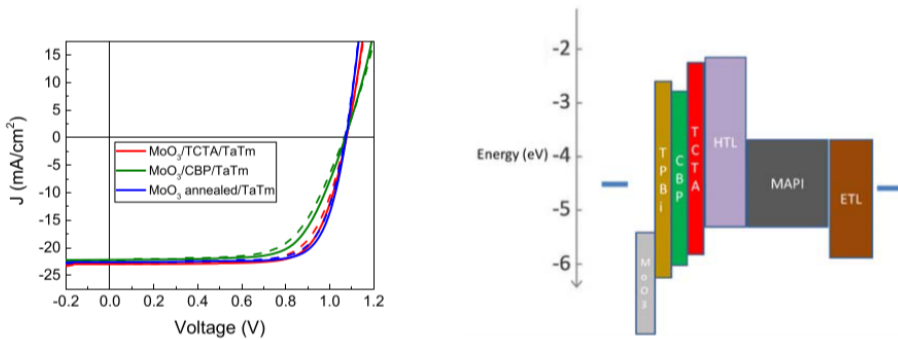


Figure S4. p-i-n solar cells with MoO<sub>3</sub> not annealed using interlayers with different ionization energies. (a) J-V characteristics under AM1.5G and (b) schematic representation of the device energy levels.

**Table S1:** Photovoltaic parameters of p-i-n devices with TCTA or CBP on top of as-deposited (not annealed) MoO<sub>3</sub>, displayed in figure S4. Annealed MoO<sub>3</sub>-based device used as a reference.

Sample	PCE (%)	Voc (V)	Jsc (mA/cm <sup>2</sup> )	FF (%)
MoO <sub>3</sub> /TCTA/TaTm	17.8	1.078	22.4	73.8
MoO <sub>3</sub> /CBP/TaTm	16.1	1.070	22.0	68.3
MoO <sub>3</sub> annealed/TaTm	17.9	1.066	21.9	76.6

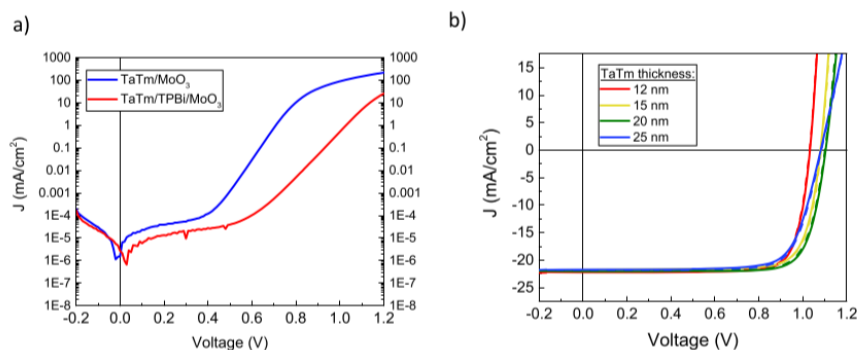


Figure S5. (a) Dark J-V curves of n-i-p solar cells using MoO<sub>3</sub> as HTL with and without TPBi interlayer. (b) n-i-p solar cells with different thicknesses of TaTm with MoO<sub>3</sub> as HTL.

**Table S2: Photovoltaic parameters corresponding to the best NiP solar cells with  $\text{MoO}_3$  on top of TaTm with increasing thickness, displayed in figure S5.**

Sample (TaTm thickness)	PCE (%)	Voc (V)	Jsc (mA/cm <sup>2</sup> )	FF (%)
12 nm TaTm	18.3	1.031	22.2	79.6
15 nm TaTm	18.5	1.083	21.8	78.6
20 nm TaTm	19.3	1.104	22.0	79.3
25 nm TaTm	18.0	1.086	21.7	76.3

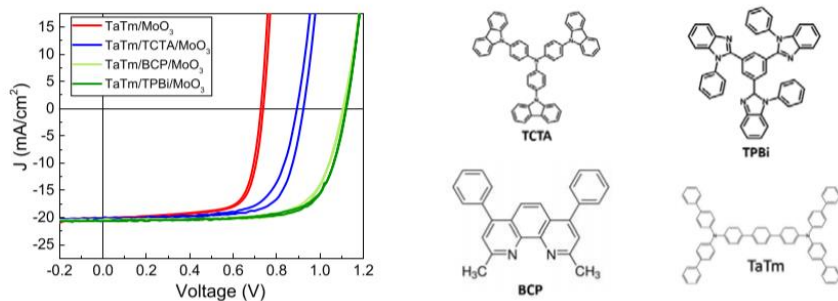


Figure S6. J-V curves of n-i-p devices using TaTm/ $\text{MoO}_3$  as HTL with TCTA, BCP or TPBi as protective interlayers. Chemical structure of the different materials is also shown.

**Table S3: Photovoltaic parameters of n-i-p solar cells with different interlayers between TaTm and  $\text{MoO}_3$ . Measurements displayed in figure S6.**

Sample (TaTm thickness)	PCE (%)	Voc (V)	Jsc (mA/cm <sup>2</sup> )	FF (%)
TaTm/ $\text{MoO}_3$	10.7	0.727	20.1	73.0
TaTm/TCTA/ $\text{MoO}_3$	13.6	0.920	20.3	72.5
TaTm/BCP/ $\text{MoO}_3$	16.7	1.106	20.4	74.0
TaTm/TPBi/ $\text{MoO}_3$	17.2	1.121	20.5	75.0



# **Chapter 5:**

## **Perovskite Solar Cells: Stable under Space Conditions**

*“The cosmos is within us. We are made of star-stuff. We are a way for the universe to know itself.”*

Carl Sagan



## 5. Perovskite Solar Cells: Stable under Space Conditions

The development of vacuum-deposited perovskite solar cells based on metal oxide transport layers presented in previous chapters is a valuable tool to expand the stability of these devices. In this work, our target was testing the P-i-N structure developed in chapter 4 under space conditions. The P-i-N architecture was chosen due to its better compatibility with a P-N silicon solar cell in a tandem configuration, increasing the overall efficiency, key for space applications. We exposed more than 60 cells to high doses of 1 MeV electron radiation simulating high altitude and space conditions. Under these conditions, even up to an accumulated fluence of  $10^{16}$  e/cm<sup>2</sup>, no significant changes in the solar cell performances were observed. Within the statistical spreading of the devices, I noticed that the below average performing devices would improve after the electron beam exposure, indicating that some “self-healing” effects occur under the influence of the high energy electron irradiation. The use of a metal oxide as the front layer was found to be fundamental for the device robustness, with virtually no changes in the injection and extraction of charge carriers after irradiation.

### 5.1 Introduction

Over the last years, perovskites have evolved from simply being a raw mineral on earth’s crust as calcium titanate ( $\text{CaTiO}_3$ ) to becoming the photoactive material in advanced solar cells as methylammonium lead triiodide ( $\text{CH}_3\text{NH}_3\text{PbI}_3$ ), with power conversion efficiencies higher than 25%.<sup>20,108,109</sup> The rapid efficiency evolution combined with the very thin complete stack (< 1 micrometer) situates this photovoltaic technology as a promising candidate for space applications. As such it may have the potential to meet the requirements to provide safe and durable energy, for satellites and space stations. The main solar cell technologies used in space to-date are III-V compound and crystalline silicon solar cells, which need to resist high-energy cosmic radiation due to the reduction of earth’s magnetic field at high altitudes.<sup>110</sup> Although these technologies have proven to be very efficient, their main drawbacks are the low power to weight ratio, the cost of production, and their durability in the harsh conditions of space.<sup>111,112</sup>

Perovskites can result in efficient and lightweight solar cells due to their high absorption coefficient,<sup>20</sup> and their long charge carrier diffusion lengths<sup>31</sup> which leads to an impressive high power to weight ratio of 26 W/g<sup>113</sup> with a thickness in general below 1 micrometre.<sup>15</sup> More interestingly, vacuum-deposited solar cells can stand out thanks to their specific advantages, most importantly the complete lack of volatile solvents in the finished stack. Additionally, there are reports mentioning that some fundamental properties, such as their even longer charge carrier diffusion lengths of more than 1 μm are better than in solution processed analogous.<sup>114</sup> It is expected that perovskite can dissipate the high generation of carriers due to cosmic electrons and Cerenkov radiation. Metal halide perovskites' low defect density<sup>115</sup> is also useful for space applications, as it has been demonstrated to be a key factor for radiation hardness when perovskite single crystals were exposed to electron beams.<sup>116,117</sup> Additionally, the versatility of vacuum processes is appealing, for instance, in the possibility of flexible substrate deposition, the high purity of the material and its high robustness due to the stable cubic structure at room temperature.<sup>14</sup>

According to the standard space solar cell qualification and quality requirements, AIAA S-111A-2014/A1-2019, the tests to predict degradation in space require the use of high energy electron irradiation. Seminal reports have shown a moderate to high impact of electron radiation on the general performance of perovskite solar cells, yet they never start from high efficiency devices.<sup>116,118,119</sup> Additionally, several of these studies used lower energy (keV) electron beams, in general those used in scanning electron microscopy, showing structural changes in solution processed perovskite films.<sup>120</sup> Recently, highly efficient solution processed PSCs were tested under electron irradiation.<sup>121</sup> In that study, the initial PCE was around 20 %, and upon exposure to 1 MeV e-beam with an accumulated fluence up to  $10^{15}$  e<sup>-</sup>/cm<sup>2</sup>, a significant reduction in the PCE of the solar cells was observed. This was caused by a strong reduction in the short circuit current ( $J_{sc}$ ), caused by a combination of irradiation induced darkening of the substrate (soda lime glass) and perovskite degradation.

Additional FF deficits observed for the highest electron doses might be attributed to the presence of a doped system as front layer for the irradiation. Metal oxides are known to be more robust than doped organic materials under electron beams. Knock-on damage, ionization, and inelastic scattering are the main damage effects of high energy electrons. Exposing metal oxides to different electron doses leads to defects in the metal oxide crystal structure, generally beneficial for the charge transport, increasing their

conductivity.<sup>122,123</sup> Moreover, doped systems tend to suffer more damage from electron exposure, according to several works testing both organic and inorganic materials for electron microscopy.<sup>124</sup>

For these reasons, in this work I tested the effects of electron irradiation on vacuum-deposited perovskite solar cells employing a metal oxide as front layer, showing the robustness of the P-i-N structure developed in chapter 4. The electron irradiation was performed in TU Delft, in the Netherlands, by the group of Prof. Ferdinand Grozema following a procedure described in the following section. I prepared the devices and characterized them before and after the electron exposure. As a result, the combination of a TMO as front layer and vacuum-deposited perovskites as light absorber led to a very robust system which displayed minimal changes upon the electron exposure for the first time in literature. As a result, new applications for PSCs are currently being tested, with several space flights scheduled for the coming years.

## 5.2 Experimental and methodology

The preparation and characterization of the samples in this chapter follows a similar procedure than the one reported in chapter 4, being the only difference the type of substrate used. Here, we employed ITO-coated quartz substrates to avoid the darkening of the substrate under the electron beam, which happened when using standard soda lime glass due to the presence of impurities. The ITO on the quartz substrate was patterned using HCl gas as etching agent. The devices were encapsulated using an aluminium plate coated with a UV-curable resin on the edges as encapsulant. The irradiation experiments were performed at Delft university using 1 MeV electrons from a Van de Graaf electron accelerator, at 20 °C, for approximately 200 and 2000 s ( $5 \times 10^{11} \text{ e}^- \text{ s}^{-1} \text{ cm}^{-2}$ ), for the  $10^{14}$  and  $10^{15} \text{ e}^-/\text{cm}^2$ , respectively. The device structure is: Glass or quartz / ITO / MoO<sub>3</sub> (7 nm) / TaTm (10 nm) / CH<sub>3</sub>NH<sub>3</sub>PbI<sub>3</sub> (600 nm) / C<sub>60</sub> (25 nm) / BCP (7 nm) / Ag (100 nm).

### 5.3 Results and discussion

The first irradiation experiments were performed on our standard device stack, which used ITO coated soda lime glass as substrate. As it was said before, the material turned into a dark brown colour due to the presence of impurities, which act as traps for electrons, leading to colour centres in the material.<sup>125</sup> As a consequence,  $J_{sc}$  was reduced due to the parasitic absorption of the glass and therefore the overall efficiency, going from 18% to 12 and 10% for fluences of  $10^{14}$  and  $10^{15} \text{ e}^-/\text{cm}^2$ , respectively.

To reliably measure the  $J_{sc}$  of the devices I used ITO-coated quartz substrates, which do not react under the electron flux. This second batch of cells was irradiated under fluences of  $10^{14}$ ,  $10^{15}$  and  $10^{16} \text{ e}^-/\text{cm}^2$ .  $10^{14} \text{ e}^-/\text{cm}^2$  is equal to 10 years in low orbit conditions. More than 20 cells were irradiated at each fluence to have enough data points. In figure 25 all the results are summarized. We show, for each fluence, the solar cell parameters measured before (dark colour and closed symbol) and after irradiation (light colour and open symbol). On average, the solar cell parameters after irradiation are:  $J_{sc}$  of  $21.5 \text{ mA/cm}^2$ ,  $V_{oc}$  of  $1.105 \text{ V}$  and FF of 80%, leading to a PCE of  $\sim 19\%$ . It was found that, even for the highest dose, the solar cell parameters remained unchanged, which is surprising and shows how robust these devices are. Only the FF shows a general decrease for all the doses, but independent on the electron fluence, which discards a possible degradation coming from the irradiation and points more towards general ageing of the devices.

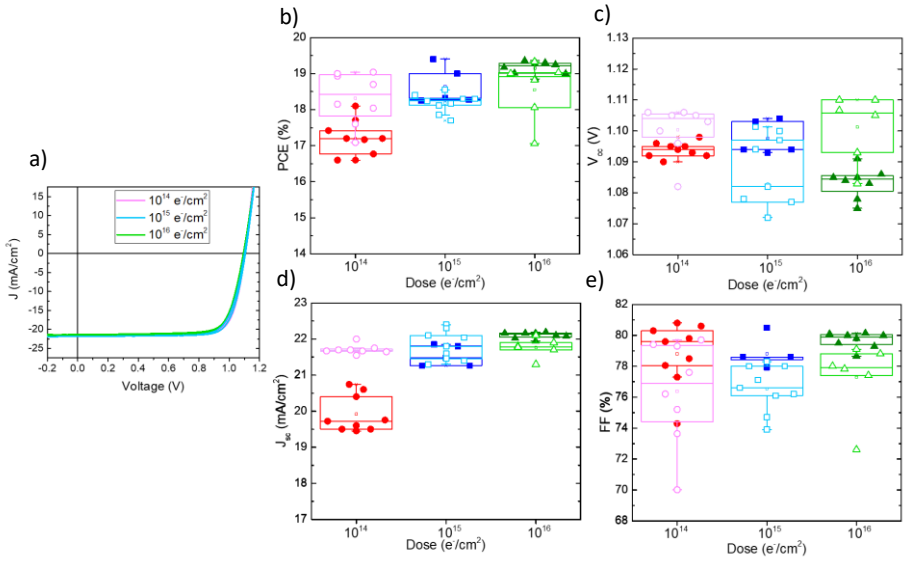


**Figure 25:** Quartz substrate-based PSCs. a) Representative J-V curves obtained under 1 sun illumination for solar cells exposed to different accumulated fluences. b-e) PCE,  $J_{sc}$ ,  $V_{oc}$ , and FF versus accumulated electron fluence, respectively, of the quartz substrate-based solar cells. Closed symbols are the values before irradiation and open symbols are after irradiation

We found that samples with the initial performance below the average displayed a recovery after irradiation (figure 25, red). All of them have very similar performances after irradiation. This healing effect was observed mainly in  $V_{oc}$  and  $J_{sc}$  and we ascribe it to the passivation of possible traps in the perovskite. To confirm this, we measured the photoluminescence of the irradiated devices. The steady state photoluminescence was measured using an excitation wavelength of 350 nm with a bandwidth of 7 nm and a wide emission range from 380 to 910 nm (Figure 26). The photoluminescence signal of the HTL used, TaTm, appears around 450 nm and is identical in shape for all irradiation doses. Hence, no detectable damage can be observed for this layer. The typical photoluminescence of MAPI is observed at 769 nm. When plotted in a logarithmic scale (figure 26, b) an additional emission can be observed at 650 nm for the cells irradiated with accumulated fluences of  $10^{15}$  and  $10^{16}$  e<sup>-</sup>/cm<sup>2</sup>. A similar higher energy emission was observed by Xiao et al., after exposing solution processed  $\text{MAPbI}_3$  films to electron beams with keV energies. They attributed that emission to the formation of perovskite phases with an excess of  $\text{PbI}_2$ .<sup>120</sup> We hypothesize that these perovskite phases may passivate the traps in the defective samples, increasing charge collection and reducing recombination, therefore increasing  $J_{sc}$  and  $V_{oc}$ . We found that the

intensity of that higher energy emission is two orders of magnitude lower than the primary emission from MAPI and hence, this is only a marginal effect in our sublimed perovskite films. As it was said before, electron-beam damage observed on solution processed films was much higher compared with single crystal samples.<sup>116,117</sup> This would indicate that the vacuum sublimed perovskite are more stable under high energy irradiation due to their lower trap density.<sup>115</sup>

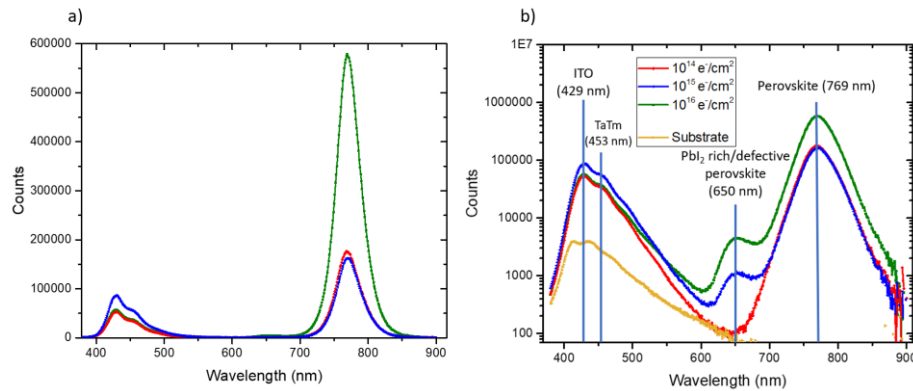


**Figure 26:** Fluorescence spectrum of devices irradiated at different electron doses in linear (a) and logarithmic scale (b). An excitation wavelength of 350 nm was used.

Analysis of the irradiated MAPI films using XRD and SEM did not reveal any significant change in the crystallinity or grain morphology (Figure 27). Other characterization techniques were done in Delft university, such as time resolved microwave conductivity (TRMC), explained in detail in the complete publication after this section. These measurements, again, only showed a minimal impact of the irradiation on the perovskite charge carriers' lifetime.

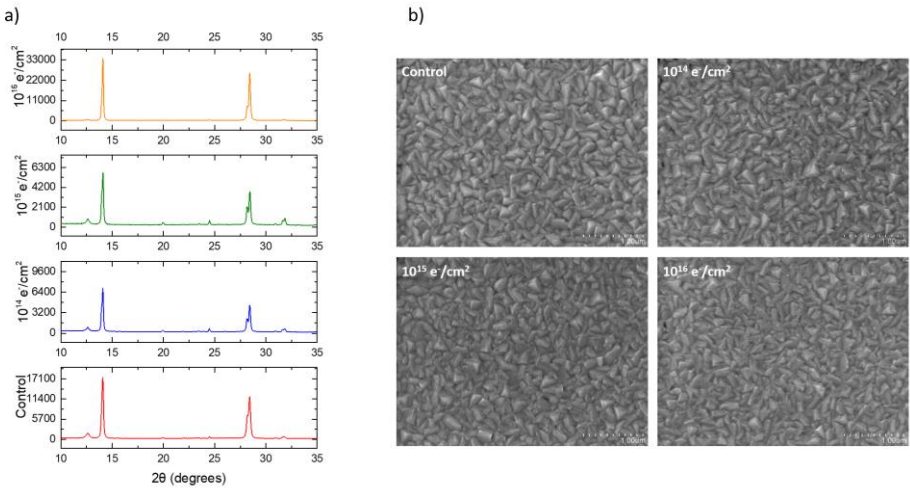


**Figure 27:** XRD spectra (a) and SEM images (b) of perovskite samples deposited on glass and capped with PMMA as encapsulation, which were exposed to different electron doses.

## 5.4 Conclusions

In conclusion, we expose vacuum-deposited perovskite solar cells developed in the previous chapter to high doses of 1 MeV electrons, we chose this configuration which use a metal oxide in the front side for hole injection to check the robustness of these PSCs in conditions that simulate in an accelerated way the exposure to cosmic electrons. Such an analysis is fundamental for future space applications. We demonstrate beyond any doubt that these samples can survive high doses of 1 MeV electrons, which simulate decades in low orbit. The samples can retain power conversion efficiencies of more than 18% for the first time, and even improve their performance when the values are lower than the average. We attribute this to a passivation of defects by the formation of rich  $\text{PbI}_2$  phases in the perovskite induced by the electron's kinetic energy, demonstrated by photoluminescence and TRMC experiments.

## 5.5 Contribution of the author

The work developed in this chapter was carried out in collaboration with Dr. Claus Zimmermann from Airbus Space and Defence and Dr. Ferdinand Grozema from Delft University. The electron irradiation and TRMC measurements were performed in Delft University and the fabrication and characterization of the devices was performed in the Molecular Science Institute (ICMol) from the university of Valencia. The author developed the main fabrication and characterization tasks along with the writing of the manuscript.

**Daniel Pérez-del-Rey**, Chris Dreessen, Ana M. Igual-Muñoz, Lennart van den Hengel, María C. Gélvez-Rueda, Tom J. Savenije, Ferdinand C. Grozema, Claus Zimmermann, Henk J. Bolink. “Perovskite Solar Cells: Stable under Space Conditions” Sol. RRL, 4: 2000447

## Perovskite Solar Cells: Stable under Space Conditions

Daniel Pérez-del-Rey, Chris Dreessen, Ana M. Igual-Muñoz, Lennart van den Hengel, María C. Gélvez-Rueda, Tom J. Savenije, Ferdinand C. Grozema,\* Claus Zimmermann, and Henk J. Bolink\*

**Metal halide perovskite solar cells (PSCs) are of interest for high altitude and space applications due to their lightweight and versatile form factor. However, their resilience toward the particle spectrum encountered in space is still of concern. For space cells, the effect of these particles is condensed into an equivalent 1 MeV electron fluence. The effect of high doses of 1 MeV e-beam radiation up to an accumulated fluence to  $10^{16} \text{ e}^- \text{ cm}^{-2}$  on methylammonium lead iodide perovskite thin films and solar cells is probed. By using substrate and encapsulation materials that are stable under the high energy e-beam radiation, its net effect on the perovskite film and solar cells can be studied. The quartz substrate-based PSCs are stable under the high doses of 1 MeV e-beam irradiation. Time-resolved microwave conductivity analysis on pristine and irradiated films indicates that there is a small reduction in the charge carrier diffusion length upon irradiation. Nevertheless, this diffusion length remains larger than the perovskite film thickness used in the solar cells, even for the highest accumulated fluence of  $10^{16} \text{ e}^- \text{ cm}^{-2}$ . This demonstrates that PSCs are promising candidates for space applications.**

Thin film metal halide perovskite solar cells (PSCs) have reached power conversion efficiencies as high as 25% for single-junction solar cells.<sup>[1–3]</sup> Similar efficiencies have been reached for multijunction cells using two different perovskite absorbers.<sup>[4,5]</sup> For these multijunction cells, it is expected that much higher efficiencies can be reached by reducing losses from the wide bandgap subcell.<sup>[6–8]</sup> Due to the high absorption coefficient and direct bandgap, the perovskite films are rather thin, in the range of

0.5 μm.<sup>[9]</sup> This implies that the complete solar cell stack is generally less than 1 μm thick if we exclude the substrate. Therefore, when used on a thin and lightweight substrate, their power to weight ratio can be very high ( $26 \text{ W g}^{-1}$ ) for a 4 μm-thick polyester substrate.<sup>[10]</sup> These properties make PSC very appealing for high altitude and space applications. In space applications the solar cells are exposed to high energy radiation and it is therefore crucial to evaluate their stability under such conditions. In one case PSCs were tested in the stratosphere by elevating them using a balloon flight. The power conversion efficiency (PCE) dropped with 36% after the balloon flight.<sup>[11]</sup> Several accelerated tests exposing the solar cells to high doses of high energy radiation using electrons,<sup>[12]</sup> protons,<sup>[13,14]</sup> neutrons,<sup>[15]</sup> and gamma-rays<sup>[16]</sup> have also been performed in PSCs. In all but one case, the initial PCE of the used cells was in between 5% and 14%, which may not be representative as only high-efficiency PSCs will eventually be used in space missions. Even though the results on these cells are in general positive, there are still considerable uncertainties. In addition, a number of studies using lower energy (keV) electron beams, in general those used in scanning electron microscopy (SEM), have shown structural changes in solution-processed perovskite films.<sup>[12,17,18]</sup> The damage in these experiments is caused by the high accumulated dose rates, in the order of  $1 \times 10^{18}$  to  $1 \times 10^{20} \text{ e}^- \text{ cm}^{-2}$ . In addition, the energy deposition for keV electron beams is very different from 1 MeV electrons. At these low energies the penetration depth is much less, which is likely to lead to more direct damage in the perovskite layer. According to the standard space solar cell qualification and quality requirements, AIAA S-111A-2014/AI-2019, the tests to predict degradation in space require the use of high energy electron irradiation. These conditions were used recently to evaluate solution-processed PSC with a high PCE.<sup>[19]</sup> In that study the initial PCE was around 20% and thus significantly above that of previously studied PSCs which were studied under various irradiation conditions. Upon exposure to 1 MeV e-beam with an accumulated fluence up to  $10^{15} \text{ e} \text{ cm}^{-2}$ , a significant reduction in the PCE of the solar cells was observed. This was caused by a modest reduction in the open-circuit voltage ( $V_{oc}$ ) and fill factor (FF), but primarily by a strong reduction in the short-circuit current ( $J_{sc}$ ). The strong decrease in the  $J_{sc}$  upon irradiation was a combination of irradiation-induced darkening of the soda lime glass used as the substrate and perovskite degradation.

D. Pérez-del-Rey, C. Dreessen, A. M. Igual-Muñoz, Prof. H. J. Bolink  
Instituto de Ciencia Molecular  
Universidad de Valencia  
C/ Catedrático J. Beltrán 2, Paterna 46980, Spain  
E-mail: henk.bolink@uv.es

L. van den Hengel, Dr. M. C. Gélvez-Rueda, Dr. T. J. Savenije,  
Prof. F. C. Grozema  
Department of Chemical Engineering  
Delft University of Technology  
Van der Maasweg 9, Delft 2629 HZ, The Netherlands  
E-mail: F.C.Grozema@tudelft.nl

Dr. C. Zimmermann  
Solar Array Department  
Airbus DS  
Munich 81663, Germany

 The ORCID identification number(s) for the author(s) of this article can be found under <https://doi.org/10.1002/solr.202000447>.

DOI: 10.1002/solr.202000447

In this work we demonstrate beyond any doubt that PSCs are stable under high doses of 1 MeV e-beam radiation conditions. We do this by investigating high efficiency vacuum-deposited methyl ammonium lead iodide ( $\text{MAPbI}_3$ )-based PSCs on both soda lime and quartz substrates and by extending the accumulated fluence to  $10^{16} \text{ e}^- \text{ cm}^{-2}$ . Under these conditions, the quartz substrate-based PSC shows virtually no degradation. Surprisingly, we find in our study of more than 60 cells that those show initially slightly lower performance improves after e-beam exposure, whereas top performing cells remain unchanged.

The  $\text{MAPbI}_3$  films were characterized using X-ray diffraction (XRD), SEM upon preparation. In Figure 1, the typical X-ray diffractogram is depicted for the pristine film. The reference sample has the typical diffraction patterns for this perovskite, highly oriented along the 001 direction (Figure 1a). The  $\text{MAPbI}_3$  also exhibited the typical grain structures (Figure 1b) and spectroscopic features (Figure S1, Supporting Information).<sup>[20]</sup>

The typical performance of the solar cells using the films is similar as previously reported,<sup>[21]</sup> and the current density ( $J$ ) versus voltage ( $V$ ) curves when illuminated with 1 sun of AM1.5 spectrum are shown in Figure 1d. The key performance parameters derived from the  $J-V$  curve are as follows:  $J_{sc}$  of  $20.6 \text{ mA cm}^{-2}$ ,  $V_{oc}$  of  $1.16 \text{ V}$ , and FF of 78% leading to a PCE of 18.6%.

The first irradiation experiments were done using solar cells that were deposited on ITO-coated glass substrates. These were irradiated (radiation incident on the glass ITO side of the device) with 1 MeV electrons reaching fluences of  $10^{14}$  and  $10^{15} \text{ e cm}^{-2}$ . To ensure that the encapsulation is robust enough and sample shipment from Valencia to Delft and back is not affecting the performance, control devices were also included in the experiments.

The irradiation experiments were performed using 1 MeV electrons from a Van de Graaf electron accelerator, at  $20^\circ\text{C}$ , for approximately 200 and 2000 s ( $5 \times 10^{11} \text{ e s}^{-1} \text{ cm}^{-2}$ ), for the  $10^{14}$  and  $10^{15} \text{ e cm}^{-2}$ , respectively. The use of soda lime glass as the substrate introduces a complication because it contains impurities. These impurities act as traps for electrons and holes in the materials generated by the high energy electron irradiation, leading to color centers in the material.<sup>[22]</sup> These are long-lived trapped charges that absorb in the visible and therefore leads to a progressive darkening of the substrate with higher accumulated fluences (Figure 2a). This led to a reduction in the  $J_{sc}$  going from 20 to 14 and  $12 \text{ mA cm}^{-2}$ , respectively, for the two fluences used. Interestingly, the FF is virtually unaffected by the irradiation or, if anything, it leads to an increase in FF (Figure 2c).

The  $V_{oc}$  is slightly reduced, from  $1.14$  to  $1.11 \text{ V}$  upon irradiation (Figure 2b,c). This minor decrease can be accounted for by the reduction of the  $J_{sc}$ . As a result of the strong reduction in  $J_{sc}$ , the PCE of the solar cells drops from an average value of 18% to 12% and 10% for the cells exposed to e-beam radiation of fluences reaching  $10^{14}$  and  $10^{15} \text{ e cm}^{-2}$ , respectively. The variation in the performance parameters for the different cells is very small as can be observed from Figure 2c with most of the cells that were evaluated showing a similar performance as a function of irradiation dose.

For confirmation of the suspected darkening of the glass substrates as cause of the reduction in  $J_{sc}$  and, more importantly, for the study of PSC without this artifact, a second series of devices was prepared on ITO-coated quartz substrates. The initial performance is similar, yet the best performing cells had a PCE of 19%, therefore slightly higher than those prepared on glass substrates. This slight increase is not the effect of the substrate but rather

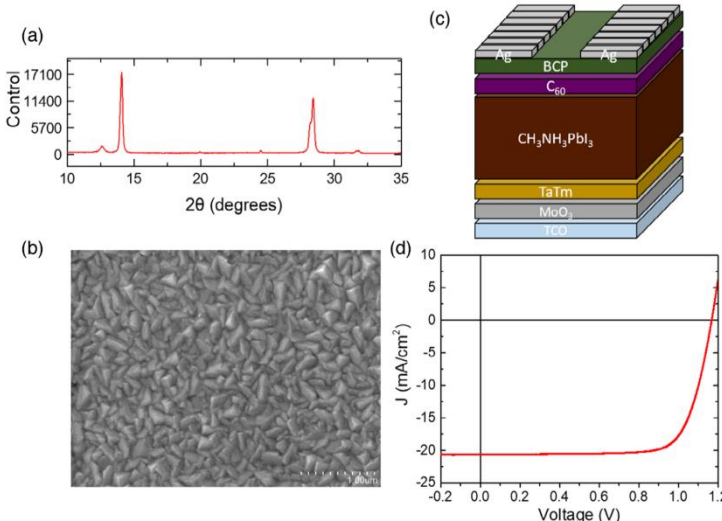


**Figure 1.** a) XRD diffraction pattern of the sublimed  $\text{MAPbI}_3$  film capped with 50 nm of PMMA. b) Scanning electron microscope image of perovskite deposited on glass. c) Schematic of the used solar cell layout: ITO/MoO<sub>3</sub> (5 nm)/TaTm (10 nm)/ $\text{CH}_3\text{NH}_3\text{PbI}_3$  (600 nm)/C<sub>60</sub> (25 nm)/BCP (7 nm)/Ag. d)  $J-V$  curve under AM1.5 illumination at 1 sun intensity.

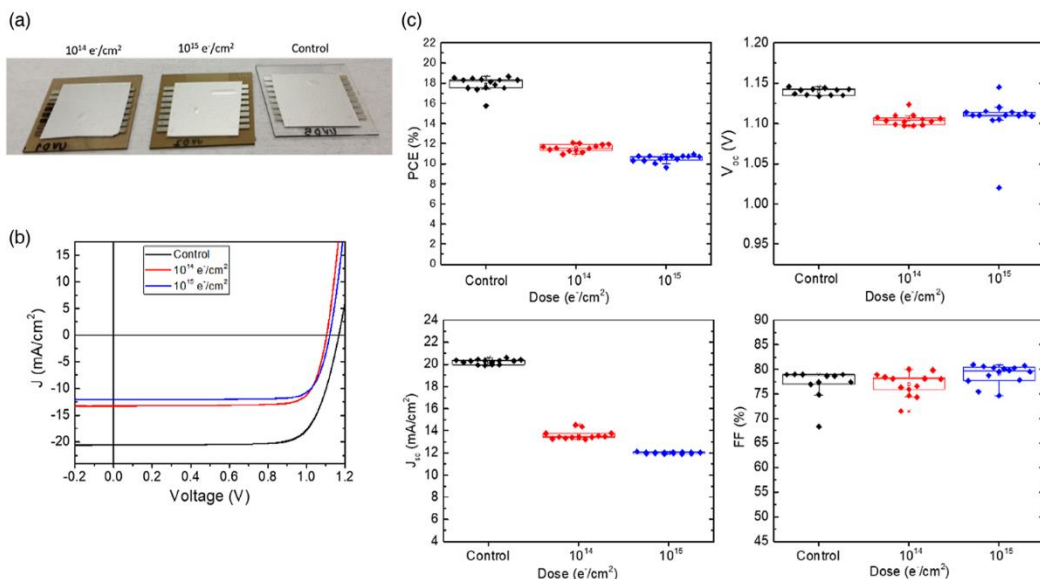


**Figure 2.** Performances for devices on soda lime glass a) images of the reference and e-beam exposed solar cells, b)  $J$ - $V$  curves under AM1.5 illumination at 1 sun intensity, and c) PCE,  $J_{sc}$ ,  $V_{oc}$ , and FF derived from the  $J$ - $V$  curves and plotted as a function of electron beam fluence. The control devices were also shipped and kept in air for the same duration as the longest e-beam irradiation experiment.

some small fluctuation in device performance over time. We attribute these slight changes to the use of different batches of  $\text{PbI}_2$  and MAI as the second series of e-beam experiments was performed several months after the first set of experiments. For this second batch of cells, we extended the accumulated electron fluence up to  $10^{16} \text{ e}^- \text{ cm}^{-2}$ . The radiation was again incident on the ITO side (now on the quartz substrates) of the devices. As the control devices on glass substrates did not show degradation during shipping and exposure to air, they were omitted in this second batch of PSCs on quartz substrates. Compared with the previous batch, the variation in performance of the as-prepared cells is slightly increased. The PCE varies from 16% to 19%. The origin of the increased variation is not fully understood but is in part due to the patterning of the ITO which was done manually instead of using industrial photolithography as in the case of the ITO on glass substrates.

Several substrates and a multitude of cells were irradiated with 1 MeV electrons reaching fluences of  $10^{14}$ ,  $10^{15}$ , and  $10^{16} \text{ e}^- \text{ cm}^{-2}$ . The  $J$ - $V$  curves (under 1 sun illumination) of a control cell and irradiated cells are shown in Figure 3a. Both forward and reverse scans are virtually the same for all accumulated fluences; the key performance parameters for these curves differ only marginally leading to a PCE of 18–18.5% (see Table S1, Supporting Information, for the averages of the performance indicators for each accumulated fluence). Therefore, the performance of the devices remains virtually identical even when irradiated with the highest accumulated fluence of  $10^{16} \text{ e}^- \text{ cm}^{-2}$ . For the actual particle spectrum in space consists of protons and electrons with a broad range of energies. For III–V space cells,

the effect of these particles is condensed into one equivalent 1 MeV electron fluence, based on the nonionizing energy loss deposited in the material. For typical space missions, this results in equivalent fluences around  $10^{15} \text{ e}^- \text{ cm}^{-2}$ , with fluences around  $10^{14} \text{ e}^- \text{ cm}^{-2}$  encountered in low earth orbit missions, and  $10^{16} \text{ e}^- \text{ cm}^{-2}$  for missions in the inner radiation belts. For PSCs, these relative damage coefficients, correlating the effect of different energies of one particle type as well as the relative effect between electron and protons, still need to be determined. Nevertheless, the fact that no degradation is observed for a dose of  $10^{16} \text{ e}^- \text{ cm}^{-2}$  implies that PSCs are promising candidates for space applications. These findings compare favorably with results obtained under similar conditions for Si,<sup>[23]</sup> GaAs,<sup>[24]</sup> and InGaP/InGaAs/Ge,<sup>[25]</sup> single and triple junction cells that show a larger decrease in the overall efficiency (10–30%). Other thin film technologies such as CdTe and Cu<sub>(In,Ga)Se</sub> (CIGS) show similar stability than our PSCs. CdTe solar cells showed 4% degradation in overall efficiency when irradiated by 1 MeV electrons with an accumulated fluence of at  $2 \times 10^{16} \text{ e}^- \text{ cm}^{-2}$ .<sup>[26]</sup> And CIGS cells on glass have been found to be stable up to  $1 \times 10^{17} \text{ e}^- \text{ cm}^{-2}$  1 MeV electron irradiation.<sup>[27]</sup>

All the irradiation doses shown were tested on two equal devices with more than ten pixels each to discard any effect of the encapsulation and have reliable data (see Table S1, Supporting Information, for average data). As mentioned, for the quartz-based PSCs the variation in performance was larger than for the first batch on glass substrates, there were also a number of pixels with large leakage currents that were discarded from the analysis. Another result of this variation is that not all

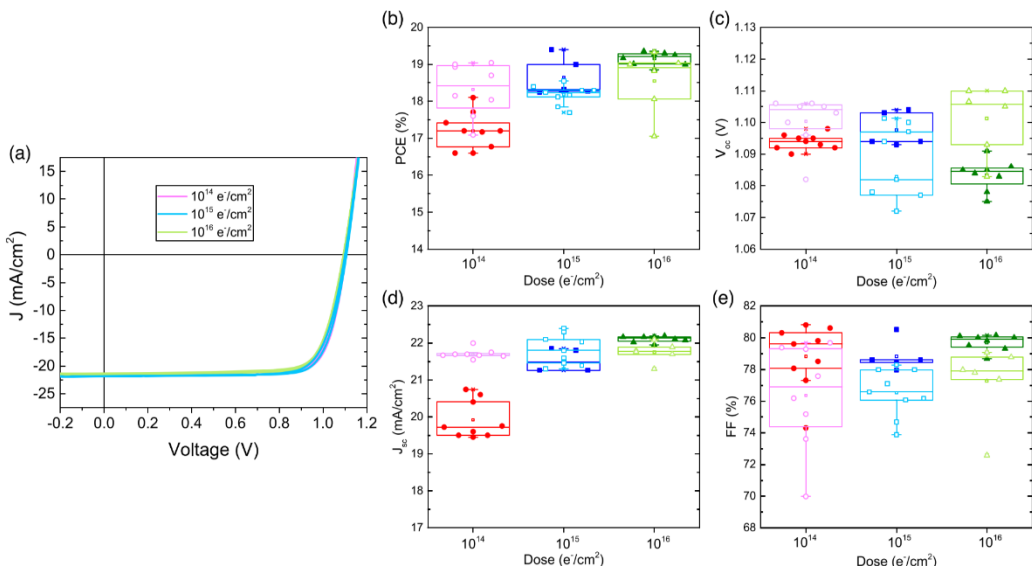


**Figure 3.** Quartz substrate-based PSCs. a)  $J$ - $V$  curves obtained under 1 sun illumination for solar cells exposed to different accumulated high energy eV fluences. b–e) PCE,  $J_{sc}$ ,  $V_{oc}$ , and FF versus accumulated electron fluence, respectively, of the quartz substrate-based solar cells. Closed symbols are the values before irradiation and open symbols are after irradiation.

cells had the same PCE prior to the irradiation experiments. This variation, although undesired, has allowed us to observe an unexpected behavior of the PSCs. Namely, the PSC with a lower initial performance become better after irradiated with MeV electrons. This effect can be clearly observed for the cells irradiated with an accumulated dose of  $10^{14} \text{ e}^- \text{ cm}^{-2}$ . For these cells, both the  $J_{sc}$  and  $V_{oc}$  increase, whereas the FF slightly decreases.

A decrease in the FF is generally observed for all cells exposed to different irradiation doses. The  $J_{sc}$  when initially in between  $21$  and  $22 \text{ mA cm}^{-2}$  is not significantly affected by the irradiation, independent on the accumulated fluence reached. Only when the  $J_{sc}$  is low on the pristine cells, it increases upon irradiation. There is also a notable increase in the  $V_{oc}$  for the cells exposed to accumulated fluences of  $10^{14}$  and  $10^{16} \text{ e}^- \text{ cm}^{-2}$ . Unfortunately, the variation of data for the cells exposed to accumulated fluences of  $10^{15} \text{ e}^- \text{ cm}^{-2}$  is too large to draw conclusions from it. However, for the other two accumulated fluences, below and above  $10^{15} \text{ e}^- \text{ cm}^{-2}$  the effect is clear, which we therefore assume to be a general trend for all accumulated fluences. Due to this “healing” effect on  $J_{sc}$  which compensates for the loss in FF, the overall PCE of the solar cells remains unchanged upon irradiation.

The penetration depth of the high energy electrons is much larger than the thickness of the used quartz plates ( $0.7 \text{ mm}$ ) and therefore eventually all electrons reach the perovskite layer. The effect of radiation can actually only be related to the cell as a whole. The perovskite layer is so thin ( $0.6 \mu\text{m}$ ) that almost no direct ionizations will take place for  $1 \text{ MeV}$  electrons. However, there are indirect effects; the passing of the electrons through quartz will generate Cerenkov radiation (wide range of

wavelengths peaking in the UV) which will be absorbed in the perovskite and can lead to damage. In addition, backscattering from the aluminum back electrode will result in some low-energy electrons that will deposit energy (ionizations) in the perovskite. Therefore, on the cell level we can only see the overall effect of the irradiation dose and cannot link it to one particular section or layer within the device stack. We performed some additional experiments on irradiated devices and on the perovskite films to try and elucidate if some evidence for high energy radiation-related structural degradation in the perovskite layer can be found. Analysis of the irradiated  $\text{MAPbI}_3$  films using XRD and SEM did not reveal any significant change in the crystallinity or grain morphology (Figure 2 and 3). The steady-state photoluminescence spectra of the irradiated devices were measured using an excitation wavelength of  $350 \text{ nm}$  with a bandwidth of  $7 \text{ nm}$  and a wide emission range from  $380$  to  $910 \text{ nm}$ . The photoluminescence signal of the HTL used, TaTm, appears around  $450 \text{ nm}$  and is identical in shape for all irradiation doses (Figure S1, Supporting Information, for a typical curve). The typical photoluminescence of  $\text{MAPbI}_3$  is observed at  $769 \text{ nm}$  and also does not change significantly with irradiation dose. Therefore, no detectable damage can be observed from the PL spectra. A sensitive external quantum efficiency (EQE) measurement in the bandgap region for solar cells exposed to different irradiation fluences did not show any additional trap states (Figure S5, Supporting Information). Therefore, even though these are sensitive techniques we were unable to determine significant changes upon irradiation. By taking the first derivative of the EQE spectrum, an accurate determination of the perovskite

bandgap is obtained which is 1.60 eV in agreement with previous reports (Figure S6, Supporting Information).

In an attempt to gain more insight in the effect of exposure to 1 MeV electron on the electronic properties of the intrinsic perovskite layer, we have performed time-resolved microwave conductivity (TRMC) measurements. The perovskite samples were deposited on quartz substrates by vacuum deposition in the same way as for the solar cells discussed earlier, and subsequently sealed with a poly(methyl methacrylate) (PMMA) layer by spin-coating. This sealing is done to prevent degradation due to exposure to oxygen and water under ambient conditions. Figure 4 shows a comparison of the photoinduced conductivity in perovskite samples using the TRMC technique for different doses of irradiation with 1 MeV electrons. The samples were excited with a 3.5 ns laser pulse ( $\lambda = 650$  nm), resulting in an increase in conductivity upon photogeneration of charges. After the excitation pulse, the conductivity decays due to a recombination and trapping of charges. The difference in the decay of the photoconductivities for different irradiation doses is relatively small; however, there is a clear trend, showing slightly faster decay for the highest doses. Exponential fits of decays show a small but gradual decrease in the decay time from  $\approx 55$  ns for the unirradiated samples to  $\approx 40$  ns for the sample irradiated with  $10^{16}$  e<sup>-</sup> cm<sup>-2</sup>. This points to the formation of trapping sites in the perovskite material itself. This trap formation is supported by additional TRMC measurements for varying laser excitation densities (see Figure S7, Supporting Information). These show that for the nonirradiated sample, there is a clear higher order recombination effect, leading to faster decay for higher initial charge densities. For the sample irradiated with  $10^{16}$  e<sup>-</sup> cm<sup>-2</sup>, this second-order effect is significantly less pronounced, indicating more first-order decay by trapping. From the carrier mobility and lifetime obtained from the TRMC measurements, the carrier diffusion length can be derived, as shown in Table S2, Supporting Information. The estimated carrier diffusion lengths range from  $\approx 0.8$   $\mu$ m for the nonirradiated sample, down to

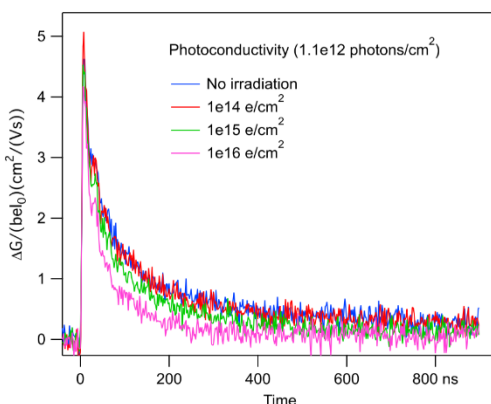


**Figure 4.** Photoinduced conductivity of perovskite samples on quartz capped with PMMA from time-resolved microwave photoconductivity measurements for the control film and those exposed with the indicated electron irradiation doses.

$\approx 0.65$   $\mu$ m for the  $10^{16}$  e<sup>-</sup> cm<sup>-2</sup> sample. The latter diffusion length is still well above the thickness of the perovskite layer in the solar cells studied here, consistent with the small effect of irradiation on the solar cells efficiency.

In conclusion, we have prepared two sets of thin film perovskite-based solar cells using vacuum sublimation for all the materials. The first set used glass-based substrates, whereas the second set was prepared using quartz substrates. The glass-based PSCs darkened significantly during irradiation experiments. This leads to a decrease in solar cells performance, but it is not clear if this originates solely from the darkened substrate or also from degradation of the solar cells themselves. The quartz substrate-based cells do not darken upon irradiation and allow for a careful analysis of the effect of the irradiation fluences on the solar cell performance. The main finding is that these fully vacuum-deposited PSCs maintain their high PCE of 19% after irradiation with high energy electrons up to very high accumulated fluence ( $10^{16}$  e<sup>-</sup> cm<sup>-2</sup>). This implies that PSCs are promising candidates for space applications. Detailed studies do show that there is a slight reduction in the FF which is compensated by an increase in the open-circuit voltage. Surprisingly, we find that cells that exhibit performances at the bottom of the distribution are improved after having been irradiated. This improvement is primarily due to an increase in open-circuit voltage. TRMC analysis on pristine and irradiated films indicates that there is a small reduction in the charge carrier diffusion length upon irradiation. Nevertheless, this diffusion length remains larger than the perovskite film thickness used in the solar cells, even for the highest accumulated fluence of  $10^{16}$  e<sup>-</sup> cm<sup>-2</sup>. This explains why no reduction in solar cells performance is observed under these conditions.

## Experimental Section

Photolithographically patterned ITO-coated glass substrates were purchased from Naranjo Substrates. N,N,N',N'-tetra[1,1'-biphenyl]-4-yl-[1,1':4',1'-terphenyl]-4,4'-diamine (TaTrm) was provided by Novaled GmbH. Fullerene (C<sub>60</sub>) was purchased from sigma-Aldrich. PbI<sub>2</sub> was purchased from Tokyo Chemical Industry CO (TCI), while CH<sub>3</sub>NH<sub>3</sub>I (MAI), MoO<sub>3</sub> and bathocuproine (BCP) were purchased from Lumtac. ITO on quartz substrate was purchased from Präzisions Glas & Optik GmbH and patterned in-house using a soft etching process.

Thin (600 nm) MAPbI<sub>3</sub> films were formed by dual-source vacuum deposition of MAI and PbI<sub>2</sub> following the procedure used to obtain high efficiency solar cells reported previously.<sup>[28]</sup> These MAPbI<sub>3</sub> films were integrated in p-i-n-type planar solar cells, by depositing them onto an ITO-coated substrates of 3 × 3 cm covered with 5 nm of MoO<sub>3</sub> and 10 nm of TaTrm. Following the perovskite deposition, the devices were completed by depositing 25 nm of C<sub>60</sub>, 7 nm of BCP, and 100 nm of Ag (Figure 1c). All layers were deposited using thermal sublimation in an inert atmosphere-integrated vacuum chamber (see Experimental Section for more details). After preparation, the cells were encapsulated using a thin (0.8 mm) aluminum sheet and an adhesive (Figure 2a). To allow evaluating just the 600 nm MAPbI<sub>3</sub> films without degrading them during the irradiation test, they were covered with a thin (50 nm) PMMA film. The PMMA was deposited by spin-coating at 3000 rpm from a toluene solution of  $\approx 40$  mg mL<sup>-1</sup>. Prior to the SEM analysis of the irradiated films, the PMMA film was removed by washing with toluene.

The solar cells were characterized through a shadow mask with 0.05 cm<sup>2</sup> aperture using a WaveLabs Sinus 50 solar simulator with spectral response matching AM1.5G illumination. High energy electron beam radiation (1 MeV) experiments were performed Van de Graaf electron accelerator facility at Delft University of Technology. Therefore, after

preparation of the cells, they were transported from Valencia to Delft in a nitrogen-filled sealed transport container. The solar cells are irradiated from the top quartz side to the bottom aluminum side of the device stack. The cells are placed on an irradiation table covered with a frame with Kapton foil window (50 µm) for irradiation under inert gas conditions (nitrogen flow at 10 L min<sup>-1</sup>). The irradiation dose and time of exposure depend on the accumulated dose desired. For the accumulated doses of  $1 \times 10^{14}$  e<sup>-</sup> cm<sup>-2</sup> and  $1 \times 10^{15}$  e<sup>-</sup> cm<sup>-2</sup>, the solar cells and perovskite films were exposed to an irradiation dose of  $5 \times 10^{11}$  e<sup>-</sup> s<sup>-1</sup> cm<sup>-2</sup> for 200–2000 s, respectively. For the accumulated dose of  $1 \times 10^{16}$  e<sup>-</sup> cm<sup>-2</sup>, the irradiation dose was  $1 \times 10^{12}$  e<sup>-</sup> s<sup>-1</sup> cm<sup>-2</sup> for 10 000 s. The perovskite thin films were irradiated through the encapsulating PMMA layer. After the irradiation experiments, the solar cells were shipped back to Valencia and characterized again.

## Supporting Information

Supporting Information is available from the Wiley Online Library or from the author.

## Acknowledgements

The research leading to these results has received funding from the European Research Council (ERC) under the European Union's Horizon 2020 research and innovation program (grant agreement nos. 834431 and 648433), the Spanish Ministry of Science, Innovation and Universities (MINECO), MAT2017-88821-R, PCI2019-111829-2, and EQC2018-004888-P, and the Comunitat Valenciana IDIFEDER/2018/061 and Prometeu/2020/077. The project that gave rise to these results received the support of a fellowship from "la Caixa" Foundation (ID 100010434). The fellowship code is LCF/BQ/DI19/11730020.

## Conflict of Interest

The authors declare no conflict of interest.

## Keywords

1 MeV irradiation, perovskite solar cells, space applications

Received: August 1, 2020

Revised: September 12, 2020

Published online: October 7, 2020

- [1] A. Kojima, K. Teshima, Y. Shirai, T. Miyasaka, *J. Am. Chem. Soc.* **2009**, *131*, 6050.
- [2] N.-G. Park, K. Zhu, *Nat. Rev. Mater.* **2020**, *5*, 333.
- [3] T. Miyasaka, *Bull. Chem. Soc. Jpn.* **2018**, *91*, 1058.
- [4] D. Forgács, L. Gil-Escríg, D. Perez-Del-Rey, C. Momblona, J. Werner, B. Niesen, C. Ballif, M. Sessolo, H. J. Bolink, *Adv. Energy Mater.* **2017**, *7*, 1602121.
- [5] J. Tong, Z. Song, D. H. Kim, X. Chen, C. Chen, A. F. Palmstrom, P. F. Ndione, M. O. Reese, S. P. Dunfield, O. G. Reid, J. Liu, F. Zhang, S. P. Harvey, Z. Li, S. T. Christensen, G. Teeter,
- [6] D. Zhao, M. M. Al-Jassim, M. F. A. M. Van Hest, M. C. Beard, S. E. Shaheen, J. J. Berry, Y. Yan, K. Zhu, *Science* **2019**, *364*, 475LP.
- [7] X. Wang, Y. Ling, X. Lian, Y. Xin, K. B. Dhungana, F. Perez-Orive, J. Knox, Z. Chen, Y. Zhou, D. Beery, K. Hanson, *Nat. Commun.* **2019**, *10*, 695.
- [8] D. Luo, R. Su, W. Zhang, Q. Gong, R. Zhu, *Nat. Rev. Mater.* **2020**, *5*, 44.
- [9] W.-J. Yin, T. Shi, Y. Yan, *Adv. Mater.* **2014**, *26*, 4653.
- [10] M. Kaltenbrunner, G. Adam, E. D. Głowacki, M. Drack, R. Schwödiauer, L. Leonat, D. H. Apaydin, H. Groiss, M. C. Scharber, M. S. White, N. S. Sariciftci, *Nat. Mater.* **2015**, *14*, 1032.
- [11] I. Cardinaletti, T. Vangerven, S. Nagels, R. Cornelissen, D. Schreurs, J. Hruby, J. Vodnik, D. Devisscher, J. Kesters, J. D'Haen, A. Franquet, V. Spampinato, T. Conard, W. Maes, W. Deferme, J. V. Manca, *Sol. Energy Mater. Sol. Cells* **2018**, *182*, 121.
- [12] N. Klein-Kedem, D. Cahen, G. Hodes, *Acc. Chem. Res.* **2016**, *49*, 347.
- [13] J. Huang, M. D. Kelzenberg, P. Espinet-González, C. Mann, D. Walker, A. Naqavi, N. Vaidya, E. Warmann, H. A. Atwater, in *2017 IEEE 44th Photovoltaic Specialist Conf. (PVSC)*, **2017**, IEEE pp. 1248–1252.
- [14] Y. Miyazawa, M. Ikegami, H.-W. Chen, T. Ohshima, M. Imaizumi, K. Hirose, T. Miyasaka, *iScience* **2018**, *2*, 148.
- [15] G. M. Paternò, V. Robbiani, L. Santarelli, A. Zampetti, C. Cazzaniga, V. Garcia Sakai, F. Cacialli, *Sustainable Energy Fuels* **2019**, *3*, 2561.
- [16] S. Yang, Z. Xu, S. Xue, P. Kandlakunta, L. Cao, J. Huang, *Adv. Mater.* **2019**, *31*, 1805547.
- [17] O. Hentz, Z. Zhao, S. Gradečák, *Nano Lett.* **2016**, *16*, 1485.
- [18] C. Xiao, Z. Li, H. Guthrey, J. Moseley, Y. Yang, S. Wozny, H. Moutinho, B. To, J. J. Berry, B. Gorman, Y. Yan, *J. Phys. Chem. C* **2015**, *119*, 26904.
- [19] Z. Song, C. Li, C. Chen, J. McNatt, W. Yoon, D. Scheiman, P. P. Jenkins, R. J. Ellingson, M. J. Heben, Y. Yan, *J. Phys. Chem. C* **2020**, *124*, 1330.
- [20] O. Malinkiewicz, A. Yella, Y. H. Lee, G. M. M. Espallargas, M. Graetzel, M. K. Nazeeruddin, H. J. Bolink, *Nat. Photonics* **2014**, *8*, 128.
- [21] D. Pérez-del-Rey, L. Gil-Escríg, K. P. S. Zanoni, C. Dreessen, M. Sessolo, P. P. Boix, H. J. Bolink, *Chem. Mater.* **2019**, *31*, 6945.
- [22] J. H. Schulman, W. D. Compton, *Color Centers in Solids*, Pergamon Press Macmillan, New York **1962**.
- [23] A. Hamache, N. Sengouga, A. Meftah, M. Henini, *Radiat. Phys. Chem.* **2016**, *123*, 103.
- [24] B. Danilchenko, A. Budnyk, L. Shpinar, D. Poplavskyy, S. E. Zelensky, K. W. J. Barnham, N. J. Edkins-Daukes, *Sol. Energy Mater. Sol. Cells* **2008**, *92*, 1336.
- [25] J. Parravicini, F. Arcadi, A. Le Donne, R. Campesato, M. Casale, E. Greco, S. Binetti, *Front. Phys.* **2019**, *7*, 169.
- [26] D. L. Bätzner, A. Romeo, M. Terheggen, M. Döbeli, H. Zogg, A. N. Tiwari, *Thin Solid Films* **2004**, *451*–452, 536.
- [27] U. Rau, A. Jaseneck, H. W. Schock, J. H. Werner, G. La Roche, A. Robben, K. Bogus, in *Conf. Record of the Twenty-Eighth IEEE Photovoltaic Specialists Conf.–2000 (Cat. No.00CH37036)*, Anchorage, AK **2000**, p. 1032.
- [28] C. Momblona, L. Gil-Escríg, E. Bandiello, E. M. Hutter, M. Sessolo, K. Lederer, J. Blochwitz-Nimoth, H. J. Bolink, *Energy Environ. Sci.* **2016**, *9*, 3456.

## Supporting information

### Perovskite Solar Cells: Stable under Space Conditions.

Daniel Pérez-del-Rey<sup>1</sup>, Chris Dreessen<sup>1</sup>, Ana M. Igual-Muñoz<sup>1</sup>, Lennart van den Hengel<sup>2</sup>, María C. Gélvez-Rueda<sup>2</sup>, Tom J. Savenije<sup>2</sup>, Ferdinand C. Grozema<sup>2</sup>, Claus Zimmermann<sup>3</sup> and Henk J. Bolink<sup>1,\*</sup>

1: Instituto de Ciencia Molecular, Universidad de Valencia, C/ Catedrático J. Beltrán 2, 46980 Paterna, Spain.

2: Department of Chemical Engineering, Delft University of Technology, Van der Maasweg 9, 2629 HZ, Delft, The Netherlands.

3: Airbus DS, 81663 Munich, Germany.

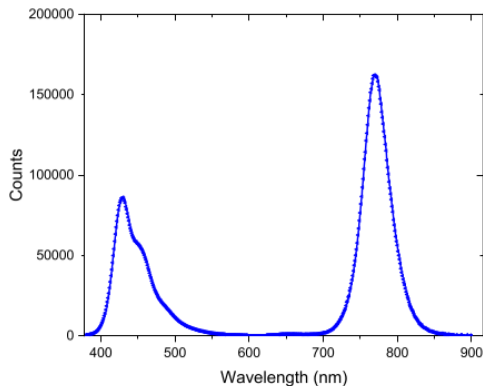


Figure S1: Fluorescence spectrum of an irradiated solar cells using an excitation wavelength of 350 nm.

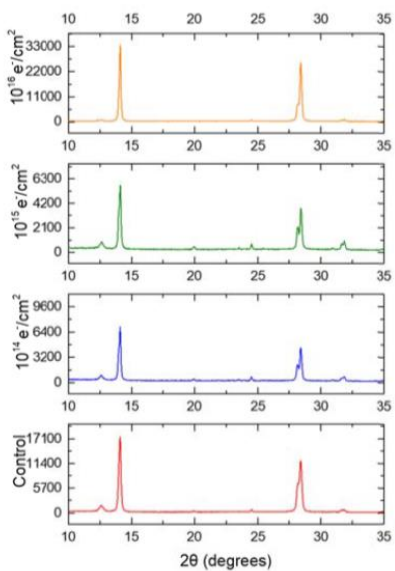


Figure S2: XRD spectra of perovskite samples deposited on glass and capped with PMMA exposed to different electron doses.

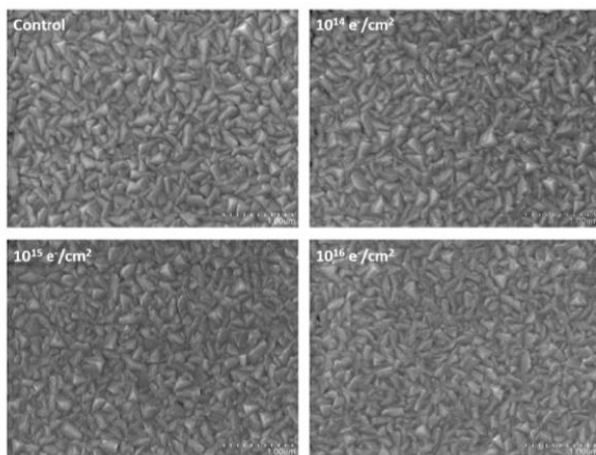


Figure S3: SEM images of perovskite layers deposited on glass irradiated under different electron doses. During irradiation the layers were covered with PMMA.

Table S1. Average performance indicators obtained from the data depicted in Figure 3 for the Quartz substrate based PSCs.

Irradiation dose		PCE (%)	Voc (V)	Jsc (mA/cm <sup>2</sup> )	FF (%)
$10^{14}$ e <sup>-</sup> /cm <sup>2</sup>	Before	17.2 + 0.5	1.094 + 0.002	19.9 + 0.5	79 + 2
	After	18.3 + 0.7	1.100 + 0.008	21.7 + 0.1	76 + 3
$10^{15}$ e <sup>-</sup> /cm <sup>2</sup>	Before	18.6 + 0.5	1.097 + 0.005	21.5 + 0.3	79 + 1
	After	18.2 + 0.3	1.082 + 0.020	21.8 + 0.4	77 + 2
$10^{16}$ e <sup>-</sup> /cm <sup>2</sup>	Before	19.1 + 0.2	1.083 + 0.005	22.1 + 0.1	80 + 1
	After	18.5 + 0.8	1.101 + 0.011	21.8 + 0.3	77 + 2

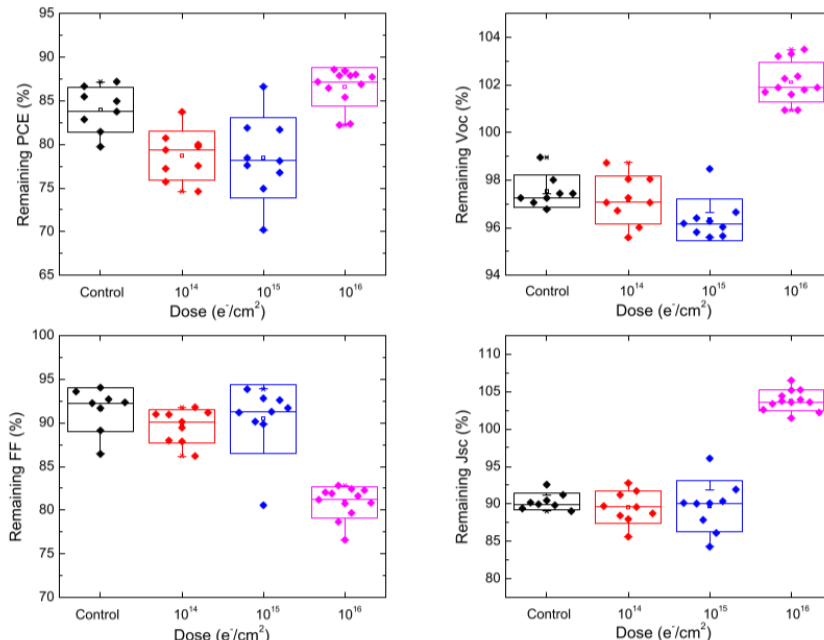


Figure S4. PCE, Jsc, Voc and FF for the slightly lower performing cells as a function of accumulated electron fluence. The data were obtained by performing J-V scans under 1 sun illumination. The control sample was not irradiated to serve as a reference. 100% would indicate no variation after irradiation.

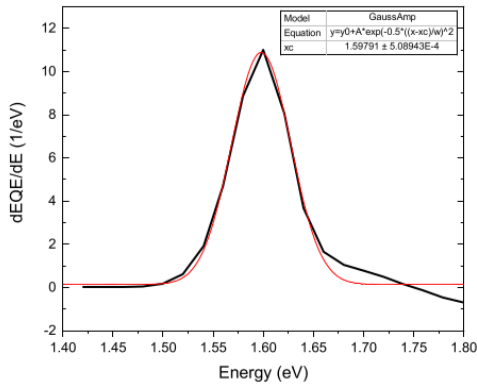


Figure S5: Bandgap determination due to the derivative of the EQE spectrum of a cell before irradiation.

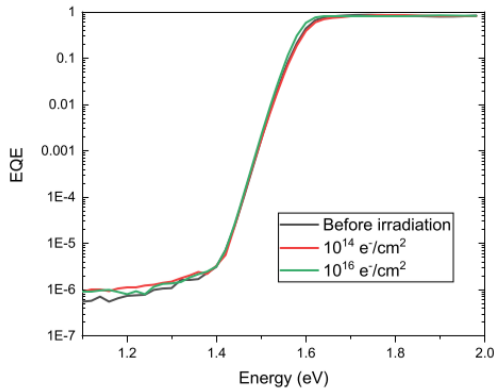


Figure S6: Sensitive EQE measurement in the bandgap region of the cells before and after irradiation.

Table S2: Charge carrier mobility ( $\mu$ ) and photoconductivity lifetime ( $\tau$ ) obtained from time-resolved microwave conductivity, together with the derived carrier diffusion coefficient ( $D$ ) and carrier diffusion length ( $L$ ) for perovskite samples on quartz substrates irradiated with different fluences.

	$\mu$ (cm <sup>2</sup> /Vs)	$\tau$ (ns)	$D$ (cm <sup>2</sup> /s)	$L$ (um)
Reference	3.98	55.9	0.10302444	0.759
1.00E+14	4.22	46	0.10942462	0.709
1.00E+15	3.73	44.97	0.09669333	0.659
1.00E+16	4.06	39	0.10507342	0.640

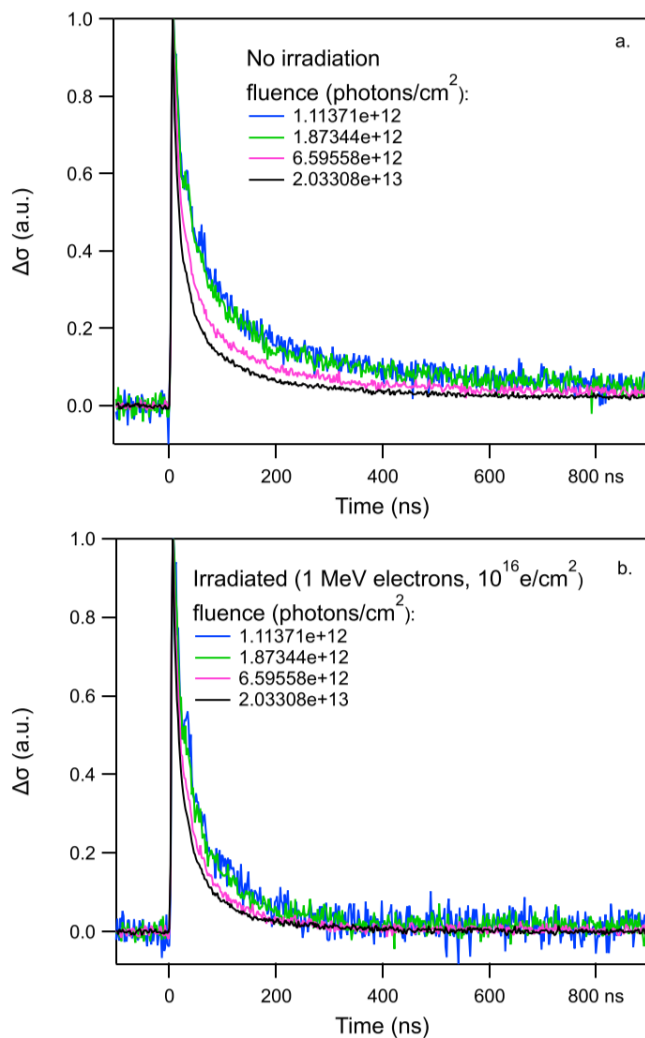


Figure S7: Normalized carrier decay for non-irradiated (a.) and irradiated (b.) vacuum deposited films of  $\text{CH}_3\text{NH}_3\text{PbI}_3$  from time-resolved microwave photoconductivity measurements for different laser fluences.

## **Chapter 6:**

## **Conclusions**

*“The good thing about science is that it is true, whether or not you believe in it.”*

Neil DeGrasse Tyson



## 6. Conclusions

This thesis aimed to substitute doped organic layers by transition metal oxides in highly efficient vacuum-deposited perovskite solar cells to increase their stability and performance. We achieved a functional and efficient N-i-P structure with metal oxides in both contacts and a stable and efficient P-i-N design under space conditions using a metal oxide as the front layer.

**In chapter 3**, I substitute the N layer, based on a doped organic material, for  $\text{TiO}_2$  in an N-i-P structure. Changing the thick doped  $\text{C}_{60}$  layer for a thin  $\text{TiO}_2$  layer reduced the parasitic absorption and the charge carrier recombination, which led to an overall increase in all the solar cell parameters. We achieved a PCE  $> 20\%$  and the highest  $V_{oc}$  for MAPI absorbers at that moment, close to the thermodynamical limit. We found an interesting activation behaviour magnified under certain simulated illumination regimes, attributed to an initial poor charge transport within the metal oxide layer. The small UV-component of AM1.5G illumination was enough to overcome this problem, adjusting the band alignment of the metal oxide with the perovskite and leading to FFs higher than 80%. Finally, by depositing a 1  $\mu\text{m}$ -thick perovskite layer, we achieved very high PCEs, close to 21%, a new record for vacuum-deposited MAPI perovskites.

**In chapter 4**, I continued this work, targeting the complete substitution of the doped organic layers in the newly developed N-i-P architecture. The substitution of the doped P layer for  $\text{MoO}_3$  was firstly optimized on the P-i-N standard configuration, with the main finding that an annealing step of the metal oxide layer was required to induce charge states that contribute to the charge transport. I developed a method to chemically induce those states by depositing on top a 1.5 nm layer of TPBi. This interlayer circumvents the need for any heat treatment, which might be detrimental in multilayer stacks such as the N-i-P configuration. By using this  $\text{MoO}_3/\text{TPBi}$  bilayer, we achieved a P-i-N design with a PCE  $> 19\%$ . When the  $\text{MoO}_3$  extraction layer was then implemented on N-i-P, the diffusion of  $\text{MoO}_3$  into the already deposited layers was causing a decrease in  $V_{oc}$ . A thin TPBi interlayer introduced prior to the  $\text{MoO}_3$  deposition protected the underlying layers, stopping the  $\text{MoO}_3$  diffusion completely with just 1.5 nm of TPBi due to this chemical interaction. Using  $\text{MoO}_3$  we achieved an N-i-P configuration with metal oxides on both sides of the device, with a PCE higher than 18%. This was the first double-oxide configuration in vacuum-deposited perovskite solar cells with high PCEs.

Finally, in **chapter 5** I tested the robustness of the P-i-N configuration developed in the previous chapter under different accumulated 1 MeV electron doses, simulating several decades in space conditions. We chose this configuration due to its future compatibility with a silicon-perovskite tandem cell. By using a quartz substrate I avoided the darkening of the material due to the high energy electrons, achieving PCEs of more than 18% after irradiation for fluences of  $10^{14}$ ,  $10^{15}$ , and even  $10^{16}$  e<sup>-</sup>/cm<sup>2</sup>. Besides the unaffected PCEs in the best pixels, those with performances below the average also displayed a “self-healing” effect, increasing their V<sub>oc</sub> and J<sub>sc</sub>. We attributed these improvements to the formation of PbI<sub>2</sub>-rich phases in the perovskite induced by the electron’s kinetic energy, which act as a passivator for defects and traps, as we confirmed by means of photoluminescence and TRMC. With this we demonstrated the potential of vacuum-deposited perovskite solar cells with a metal oxide as front layer for space applications.

In conclusion, in this thesis I have successfully implemented the use of transition metal oxides on vacuum-deposited solar cells with record power conversion efficiencies and proved their stability in harsh conditions such as space. For the first time, we achieved PCEs higher than 20% for sublimed MAPI perovskite using metal oxides as transport layers, with V<sub>ocs</sub> higher than 1.15V. I also found a novel method to deposit a metal oxide on top of the stack, leading to a double-oxide configuration, and tested the devices under extreme conditions with successful results for the first time in the perovskite field, opening the possibility of interesting space applications for vacuum-deposited perovskite solar cells with metal oxides.

## **Chapter 7:**

### **Resumen en castellano**

*“The Universe is under no obligation to make sense to you.”*

Neil DeGrasse Tyson



## 7. Resumen en castellano

### 7.1 Capítulo 1: Introducción

La humanidad precisa energía para vivir y evolucionar, como individuos y como sociedad. El 80% de la energía obtenida actualmente proviene de fuentes no renovables (figura 1), las cuales generan subproductos como el dióxido de carbono y el metano, los cuales contribuyen al efecto invernadero. La energía fotovoltaica es una gran candidata para sustituir estas fuentes de energía dada su versatilidad y adaptabilidad, dado que el sol ofrece una cantidad de energía por unidad de área muy grande. A través de la conversión de esta energía solar en electricidad a través del efecto fotoeléctrico mediante el uso de placas solares nos puede ayudar en esta transición hacia las energías limpias.

Actualmente el silicio domina el mercado de las placas solares, con más de un 80% de producción anual.<sup>3</sup> El silicio policristalino es barato y funciona adecuadamente, pero no es tan eficiente como el monocristalino, el cual tiene un mayor coste y complejidad de fabricación. Además, ambos coinciden en el inconveniente de tener un ancho de banda o *bandgap* indirecto, lo cual conlleva una peor absorción de la luz y consecuentemente la necesidad de fabricar capas de un grosor superior a otros materiales para absorber suficiente luz. Existen alternativas como el silicio amorfo, telururo de cadmio y CIGS (Seleniuro de Cobre Indio y Galio), preparadas en capas finas dados sus altos coeficientes de absorción. Las células solares de arseniuro de galio son las más eficientes de esta lista, aunque sus costes de producción son tan altos que su aplicación se ciñe a campos muy específicos como el espacial.

También existen tecnologías emergentes con propiedades interesantes como la versatilidad en la deposición, flexibilidad o bajo coste, aunque hoy en día la mayoría tienen eficiencias menores en comparación con las anteriores. Algunos ejemplos son las células de sulfuro de cobre estaño zinc (CZTS), las de colorantes sensibilizados, las células solares orgánicas, las de puntos cuánticos y las de perovskita.<sup>4</sup> Estas últimas destacan dadas sus ventajosas propiedades como el alto coeficiente de absorción, baja energía de unión de los excitones o facilidad para modificar la energía del *bandgap*. Además, los costes de producción son bajos y sus productos abundantes.<sup>5</sup> Por ello, en esta tesis nos centraremos en esta tecnología, explicada en profundidad en las siguientes secciones.

### 7.1.1 Células solares de perovskita

Cuando un fotón con una energía suficiente es absorbido en un semiconductor, un electrón de la banda de valencia pasa a la banda de conducción. La diferencia de energía entre estas dos bandas es lo que se conoce como *bandgap*. La ausencia de ese electrón en la banda de valencia es una partícula o entidad conocida formalmente como hueco. En función de la interacción coulombica entre el electrón y el hueco se puede o bien formar un excitón o electrones y huecos libres, lo cual depende de la energía de esta unión. Si esta energía es mayor a la energía térmica ( $kT$ ) se dice que el material es excitónico, lo cual no es ideal para una célula solar, ya que se requiere una energía extra para separar las cargas fotogeneradas.

En las células solares de perovskita (PSCs), los fotones son absorbidos en el material fotoactivo, la perovskita. Los pares de electrones-huecos generados pueden terminar recombiniendo o ser aprovechados en forma de trabajo si son extraídos a un circuito externo. La recombinación puede ser radiativa, generando un fotón, o no radiativa, generando calor. Una forma de reducir esta pérdida de energía es induciendo un gradiente para separar estas cargas. Esto se consigue colocando la perovskita entre dos materiales selectivos para electrones y huecos, los cuales dejan pasar los electrones mientras bloquean los huecos y viceversa, lo cual genera un gradiente que actúa como fuerza motriz para su transporte y separación. Estos materiales son generalmente semiconductores con un exceso de carga negativa (tipo N) o carga positiva (tipo P), la cual se induce químicamente o dopando los materiales. Al colocar la perovskita entre estos dos materiales se forma una estructura conocida como P-i-N. La concentración de cargas positivas o negativas en cada material determina la densidad de estados energéticos, y con ello el conocido nivel de Fermi ( $E_F$ ). En un material intrínseco este se encuentra en la mitad del *bandgap* mientras que en un material tipo P se encuentra más cercano a la banda de valencia, por ejemplo. La diferencia entre el  $E_F$  de los contactos genera una diferencia de potencial ( $V_{bi}$ ). El campo eléctrico inducido actúa como fuerza motriz que permite que los electrones y huecos sean extraídos separadamente gracias la selectividad de los materiales P y N (figura 2).

En circuito abierto, los electrones y huecos no tienen un circuito externo a donde ser extraídos y terminan recombiniendo. En cambio, en circuito cerrado y aplicando un voltaje externo menor que el  $V_{bi}$ , la difusión por diferencia de gradiente de los electrones y huecos fotogenerados y su flujo debido al campo eléctrico interno tiene el mismo signo, siendo extraídos al circuito externo. En

cambio, si el voltaje es superior al  $V_{bi}$ , la corriente de difusión es superada por la corriente del campo eléctrico inducido por el voltaje y los electrones y huecos son, en este caso, inyectados en la perovskita.

### 7.1.2 Perovskitas para uso fotovoltaico

Perovskita es cualquier mineral cuya estructura puede expresarse como  $ABX_3$ , donde A es un catión monovalente, B un catión divalente con coordinación octaédrica, y X un anión monovalente. Así, se forma una estructura octaédrica con un catión B coordinado por 6 aniones X y con aniones A llenando los intersticios de 8 octaedros (figura 3). Para determinar si un elemento podrá formar una estructura de perovskita se usa la fórmula del factor de tolerancia de Goldschmidt, el cual predice estructuras estables siempre que se encuentre entre 0.7 y 1.1 (figura 4).

Para que una perovskita tenga aplicaciones fotovoltaicas debe tener un catión 'A' orgánico y pequeño como el metilamonio ( $\text{CH}_3\text{NH}_3^+$ ), formamidinio ( $\text{NH}_2\text{CHNH}_2^+$ ) o un ion como el cesio ( $\text{Cs}^+$ ). El catión 'B' debe ser un ión metálico, generalmente  $\text{Pb}^{2+}$  o  $\text{Sn}^{2+}$ , y el anión 'X' debe ser un haluro, generalmente yoduro o bromuro, aunque también puede usarse el cloruro.

Variando estos elementos A, B y X se pueden modificar totalmente las propiedades ópticas y electrónicas del material. Modificar el haluro afecta principalmente a la banda de valencia y por ello se incrementa la energía del *bandgap* al pasar de yoduro a bromuro o cloruro. El catión A no participa directamente en la banda de valencia ni en la de conducción, pero afecta al volumen de la celda unidad de perovskita (figura 5).<sup>7-10</sup> Modificar el tamaño de este catión A reemplazando por ejemplo el  $\text{CH}_3\text{NH}_3^+$  por  $\text{Cs}^+$  conlleva a una disminución de los niveles energéticos del plomo de manera indirecta. Esto implica cambios menores en la energía del *bandgap*, pero puede tener un gran impacto en la estabilidad química de la perovskita, siendo por ejemplo más o menos estable a altas temperaturas.

La perovskita más empleada en usos fotovoltaicos es la de triyoduro de metilamonio y plomo ( $\text{CH}_3\text{NH}_3\text{PbI}_3$ ), también abreviada como MAPI. Su estructura puede pasar de tetragonal a cúbica sobre los 56 °C<sup>12,13</sup> aunque también se ha encontrado en fase cúbica a temperatura ambiente.<sup>14</sup> Es un material muy adecuado para su uso en células solares ya que posee propiedades tales como:

1. Alto coeficiente de absorción en un rango amplio de longitudes de onda, comparable con tecnologías usadas en células solares de alta eficiencia como las de GaAs o CdTe.<sup>20</sup>
2. Baja energía de unión del excitón. La energía necesaria para separar los electrones y huecos es inferior a la energía térmica, facilitando la generación de portadores de carga libres a temperatura ambiente.<sup>21-24</sup> Esto es debido a la alta constante dieléctrica de la perovskita, que tiene un efecto amortiguador en la interacción entre electrones y huecos.
3. Largas distancias de difusión de los portadores de carga. Los electrones y huecos pueden recorrer distancias superiores al propio grosor de la perovskita sin recombinar.<sup>25-27</sup> Esto permite usar grosores mayores sin reducir la eficiencia del dispositivo, incrementando así la recolección de fotones.<sup>28-30,32,33,126</sup>
4. Alta tolerancia a los defectos. Los defectos en la estructura cristalina de la perovskita tienen un impacto muy bajo en la eficiencia final del dispositivo. Aunque estos defectos pueden inducir estados electrónicos que derivarían en centros de recombinación, suelen estar localizados en las propias bandas electrónicas y no en el *bandgap*, teniendo así un impacto mínimo.

### 7.1.3 Técnicas de deposición

Existe una gran variedad de técnicas de deposición de bajo coste para las perovskitas (figura 6). Elegir la adecuada es importante, ya que tendrá un gran impacto en las propiedades finales de la capa, como la cristalinidad, tamaño de los granos o el grosor final.<sup>28,35</sup> Los métodos por disolución usan generalmente disolventes polares como la N,N dimetilformaamida (DMF), dimetil sulfóxido (DMSO) o  $\gamma$ -butirolactona (GBL) para disolver los componentes de la perovskita. Una vez disueltos, se deposita la disolución por blade-coating o spin-coating, controlando la velocidad de evaporación del disolvente para conseguir la cristalización deseada, además de seleccionar la velocidad de deposición, rotación y temperatura de secado.<sup>36</sup> También se puede promover la cristalización usando un anti-disolvente, o disolvente en el que la perovskita es insoluble. Si se añade antes del secado total una pequeña cantidad de este se puede controlar mejor la velocidad de cristalización, mejorando la calidad de las capas de perovskita. Existen también métodos en dos pasos, donde primero se deposita el haluro de plomo a partir de una

disolución de éste y a continuación se convierte a perovskita exponiéndolo al resto de los componentes. Esto se puede hacer depositando los componentes restantes por spin-coating o sumergiendo la capa de  $\text{PbX}_2$  en una disolución de estos. Finalmente se aplica temperatura para promover la reacción de los componentes y evaporar los restos de disolvente.<sup>42-45</sup> Este proceso se puede combinar con técnicas de disolución y de evaporación, donde por ejemplo se puede evaporar una capa de  $\text{PbX}_2$  y convertirla a perovskita depositando los demás componentes por disolución o viceversa.

#### 7.1.4 Deposición a vacío

La deposición a vacío consiste en sublimar en alto vacío los materiales necesarios para la formación de la perovskita con una composición concreta sobre un sustrato. Tiene ciertas ventajas con respecto a las técnicas ya descritas:

- Alta pureza de los materiales debido a la mayor temperatura de sublimación de las impurezas.
- Control preciso del grosor a través de microbalanzas de cristal de cuarzo (QCM), las cuales permiten un control nanométrico.
- Compatibilidad con multitud de sustratos, ya que si se usan condiciones estequiométricas no es necesario aplicar una temperatura para la conversión. Esto permite usar sustratos sensibles a la temperatura como plásticos.
- Intrínsecamente aditivo, siendo posible depositar materiales con polaridades similares consecutivamente dada la ausencia de disolventes en el proceso.

Podemos dividir la deposición a vacío en función del número de fuentes de evaporación empleadas:

- Deposición con 1 fuente de evaporación: Es el método más simple de obtener una capa compacta de un material dado. Se usa generalmente para depositar moléculas orgánicas, simplemente depositando el material en un crisol y aplicando temperatura hasta su evaporación o sublimación. Este método también permite preparar materiales multicomponente como la perovskita a través del método “evaporación flash”, donde se añade al crisol una mezcla de todos los componentes juntos.<sup>46-48</sup> Se incrementa la temperatura muy rápidamente para conseguir una evaporación homogénea.

-Deposición multi-fuente: Para preparar un material multicomponente lo ideal es poder controlar con precisión la cantidad de cada material evaporada. Este apartado se puede dividir en co-evaporación y deposición secuencial. En la primera (figura 6, c), se evaporan dos o más materiales al mismo tiempo controlando la cantidad de cada uno de ellos con QCMs. Este método se usa principalmente para la preparación de capas orgánicas dopadas, evaporando el material orgánico y el dopante al mismo tiempo, y para perovskitas, evaporando cada componente de manera controlada. En cambio, en la deposición secuencial se evaporan los distintos componentes uno detrás de otro en forma de capas finas (menos de 50 nm) y a través de calor y difusión se obtiene una capa homogénea e isotropa.

### 7.1.5 Óxidos metálicos como capas transportadoras

Algunos óxidos metálicos tienen excelentes propiedades transportadoras tanto para huecos como para electrones (figura 7). Son muy robustos químicamente, tienen poca absorción parásita de luz y se pueden depositar en una amplia variedad de métodos. Los óxidos de metales de transición concretamente forman un buen contacto óhmico con los cátodos y ánodos usados generalmente en las PSCs, lo cual implica una inyección de cargas más eficiente. Una de sus principales características es el auto-dopaje, donde a través de defectos en su estructura tridimensional (vacantes de metal o de oxígeno, por ejemplo), se da lugar a nuevos estados electrónicos ocupados y desocupados cerca de la banda de valencia o de conducción, dando así lugar a un dopaje de tipo N o tipo P.

### 7.1.6 Objetivos de la tesis

Esta tesis apunta hacia la mejora de las células solares de perovskitas preparadas por evaporación, mejorando su estabilidad y eficiencia. Para conseguirlo exploramos la sustitución de las capas orgánicas dopadas implementando como sustituyente óxidos de metales de transición. La tesis se estructura de la siguiente forma:

-**Capítulo 3:** Sustitución del C<sub>60</sub> dopado en las células solares N-i-P usando una dispersión de nanopartículas de TiO<sub>2</sub>, desarrollando así dispositivos de alta eficiencia y con mayor reproducibilidad.

-**Capítulo 4:** Sustitución del TaTm dopado por MoO<sub>3</sub> en células solares P-i-N y su posterior implementación en la configuración N-i-P del capítulo anterior, desarrollando así un diseño con óxidos metálicos en ambos contactos.

-**Capítulo 5:** Caracterización de la estructura P-i-N del capítulo anterior bajo condiciones espaciales, donde se demostró la alta estabilidad de estas células solares de perovskita a gran altitud.

## 7.2 Capítulo 2: Metodología experimental

Todo el trabajo experimental ha seguido el método científico y se ha desarrollado en una sala limpia de clase 10000 para reducir la presencia de polvo y otras partículas contaminantes, dado el fino grosor de los dispositivos (<1 μm).

### 7.2.1 Materiales

Los principales materiales empleados son el óxido de indio y estaño sobre un sustrato de cristal a modo de contacto transparente, sobre el cual se depositan el resto de materiales, los cuales son generalmente N4,N4,N4'',N4''-tetra([1,1'-biphenyl]-4-yl)[1,1':4',1''-terphenyl]-4,4''-diamine (TaTm) y MoO<sub>3</sub> como HTL, y TiO<sub>2</sub> y C<sub>60</sub> como ETL. Todos son comerciales y han sido previamente purificados (figura 8).

### 7.2.2 Fabricación de la perovskita de $\text{CH}_3\text{NH}_3\text{PbI}_3$

La perovskita se prepara por co-evaporación de sus dos precursores,  $\text{PbI}_2$  y  $\text{CH}_3\text{NH}_3\text{I}$  en una cámara de alto vacío (figura 9). Los materiales se depositan en crisoles cerámicos calentados con fuentes Creaphys. Estas se sitúan a 20 cm de los sustratos, los cuales se encuentran bocabajo en un ángulo de 90º. Se usan sensores de microbalanzas de cristal de cuarzo QCMs para monitorizar la cantidad de cada material que se evapora en cada fuente y otro sensor extra más arriba para la deposición total. Toda la evaporación se lleva a cabo a aproximadamente  $10^{-6}$  mbar. Las temperaturas para cada material son aproximadamente 80 °C para el  $\text{CH}_3\text{NH}_3\text{I}$  y 260 °C para el  $\text{PbI}_2$ . El  $\text{CH}_3\text{NH}_3\text{I}$  se mantiene a un ritmo de evaporación de 1 Å/s y se ajusta el  $\text{PbI}_2$  para tener condiciones estequiométricas. El grosor final de la perovskita es de unos 600 nm.

### 7.2.3 Fabricación de los dispositivos

La estructura general para una célula solar P-i-N se muestra en la figura 10 y consta de: Vidrio / ITO /  $\text{MoO}_3$  (7 nm) / TaTm (10 nm) /  $\text{CH}_3\text{NH}_3\text{PbI}_3$  (600 nm) /  $\text{C}_{60}$  (25 nm) / BCP (7 nm) / Ag (100 nm), donde el  $\text{C}_{60}$  y el TaTm actúan como capas transportadoras de electrones y huecos, respectivamente,  $\text{MoO}_3$  y BCP como capas inyectoras de huecos y electrones, respectivamente, y la plata es el contacto superior. TaTm y  $\text{C}_{60}$  se sublimaron a una velocidad de 0.5 Å/s y las temperaturas oscilaron entre 300-400 °C. BCP fue sublimado a una velocidad de 0.3 Å/s y a 150 °C.  $\text{MoO}_3$  y Ag fueron sublimados en una cámara de vacío distinta, la cual funciona aplicando una corriente muy alta (unos 4 A) para alcanzar la temperatura requerida.

Para la célula solar N-i-P la estructura es: Vidrio / ITO /  $\text{SnO}_2$  (30 nm) /  $\text{C}_{60}$  (10 nm) /  $\text{CH}_3\text{NH}_3\text{PbI}_3$  (600 nm) / TaTm (10 nm) / TPBi (1 nm) /  $\text{MoO}_3$  (7 nm) / Au (100 nm), donde la única diferencia con la P-i-N es el orden de deposición y que en este caso se usa  $\text{SnO}_2$  como capa inyectora de electrones y la combinación TPBi/ $\text{MoO}_3$  como capa inyectora de huecos. El TPBi fue sublimado de la misma manera que el TaTm y el  $\text{C}_{60}$ , pero a una velocidad menor al ser sólo 1 nm, sobre unos 0.2 Å/s y 170 °C.

#### 7.2.4 Caracterización de las células solares

-Eficiencia cuántica externa (EQE): Es el ratio entre el número de fotones que llegan al dispositivo y el número de pares electrón/hueco generados, representado en función de la longitud de onda de los fotones (figura 11).

-Curva de densidad de corriente-voltaje (J-V): Se basa en aplicar un barrido a distintos voltajes y medir la corriente que pasa por el dispositivo. Se puede realizar en oscuridad o en iluminación. En oscuridad se obtienen parámetros como la corriente de fuga o la resistencia en serie del diodo, mientras que en iluminación se obtienen los principales parámetros de la célula solar como son:

-Densidad de corriente en circuito cerrado ( $J_{sc}$ ): Es la corriente fotogenerada que fluye por el dispositivo cuando el voltaje aplicado es 0.

-Voltaje en circuito abierto ( $V_{oc}$ ): Es el máximo voltaje disponible en la célula solar cuando la corriente es 0.

-Factor de llenado (FF): Es un parámetro obtenido del ratio entre la potencia máxima de la célula solar y el producto de  $V_{oc}$  y  $J_{sc}$ . Da información acerca de la eficiencia de extracción de las cargas, la resistencia y la recombinación.

-Eficiencia de conversión energética (PCE): Se define como el ratio entre la energía incidente y la energía generada bajo unas condiciones de iluminación específicas.

### 7.3 Capítulo 3: Modificación interfacial en células solares de perovskita evaporadas basada en un óxido metálico

#### 7.3.1 Introducción

El uso de óxidos metálicos como capas de inyección está muy extendido en el campo de las células solares de perovskita por sus propiedades ventajosas tales como: baja absorción parásita, altas movilidades de electrones y huecos, buena estabilidad y facilidad de deposición. Óxidos metálicos como el  $TiO_2$  o el  $SnO_2$  son actualmente los más empleados debido a sus adecuados niveles

energéticos para el transporte de electrones y bloqueo de huecos (figura 16) y la gran variedad de métodos de deposición disponibles.

La deposición a vacío en perovskitas presenta un gran número de ventajas, citadas anteriormente. Células solares totalmente evaporadas han superado el 20% de eficiencia, compitiendo con los récords por disolución.<sup>127</sup> Una característica de este tipo de células solares es el uso de capas orgánicas dopadas para la inyección y extracción de electrones y huecos a los contactos. Este tipo de sistemas tiene un gran número de ventajas, ya que pueden formar contactos óhmicos con los electrodos y tienen una excelente movilidad de huecos y electrones junto con una resistencia en serie baja. Por otro lado, en ellas se produce una absorción parasítica de la luz y tienen una cierta inestabilidad química.<sup>83,84</sup>

Por ello, el uso de óxidos metálicos en sustitución de estas capas podría ser interesante en células solares de perovskita evaporada. Algunos estudios sugieren que la deposición de perovskita por evaporación sobre óxidos metálicos promueve una interfaz enriquecida en  $\text{PbI}_2$  debido al bajo coeficiente de adhesión del MAI, lo cual es negativo para el transporte de cargas dada la naturaleza aislante del  $\text{PbI}_2$ . Añadir capas finas autoensambladas (SAM) ha demostrado evitar este efecto de falta de estequiometría, aunque no se han llegado a fabricar dispositivos funcionales.<sup>85,86</sup>

Por todo ello y motivado por las tendencias de las células solares de perovskita depositadas por disolución, en este trabajo sustituyo la capa dopada de tipo N en la estructura N-i-P de las células solares evaporadas de alta eficiencia. Para ello, empleo una capa compacta de nanopartículas de  $\text{TiO}_2$  depositadas a baja temperatura, con la que consigo reducir la absorción parásita de la luz y reducir la recombinación de electrones y huecos. Una capa fina de  $\text{C}_{60}$  fue depositada entre el  $\text{TiO}_2$  y la perovskita para pasivar las trampas electrónicas superficiales y promover un crecimiento estequiométrico de la perovskita. Por todo ello, se pudo depositar la perovskita con un grosor cercano a 1  $\mu\text{m}$ , consiguiendo así una eficiencia superior al 20%, la mayor obtenida en células solares de perovskita MAPI evaporada en aquel momento.

### 7.3.2 Resultados y discusión

La estructura de los dispositivos de este capítulo consiste en: ITO / TiO<sub>2</sub> (30 nm) / CH<sub>3</sub>NH<sub>3</sub>PbI<sub>3</sub> (500-600 nm) / TaTm (10 nm) / TaTm:F<sub>6</sub>-TCNNQ (40 nm) / Au (100 nm). Donde el TiO<sub>2</sub> se depositó por *spin coating* siguiendo un proceso a baja temperatura (100 °C) y el resto de las capas se depositaron por evaporación a vacío, proceso descrito en el apartado 7.2.

Inicialmente, las eficiencias de los dispositivos revelaron un funcionamiento pobre de los dispositivos, siendo menores al 10% (figura 17, a). Atribuimos esto a una mala formación de la perovskita sobre el óxido como otros trabajos ya han demostrado anteriormente. Añadimos una capa fina de 10 nm de C<sub>60</sub> entre el TiO<sub>2</sub> y la perovskita para paliar este efecto negativo. Con ello conseguimos mejorar drásticamente todos los parámetros fotovoltaicos (figura 17, b), mostrando una menor recombinación y mejor transporte de cargas. Además, se observa en ambos casos un proceso de activación, mejorando la eficiencia tras sucesivas mediciones. Este proceso se vio acelerado cuando la lámpara empleada para las medidas en iluminación era de xenón, la cual posee una componente ultravioleta (tabla 1). Medidas de *Kelvin probe* e impedancia evidenciaron que la luz ultravioleta modifica la función de trabajo del TiO<sub>2</sub>, mejorando el alineamiento de las bandas y con ello el transporte de cargas con la perovskita.

Así, las células solares que empleaban TiO<sub>2</sub>/C<sub>60</sub> como capa selectiva de electrones alcanzaron eficiencias del 18-19%, mostrando una mejor reproducibilidad que los dispositivos con C<sub>60</sub> dopado (figura 18, izquierda). Se obtuvo voltajes de circuito abierto récord, de hasta 1.17 V, y cercanos al límite teórico. Esta baja recombinación fue una motivación para incrementar el grosor de la perovskita hasta 1 μm, maximizando así la absorción de la luz. Con ello obtuvimos un dispositivo récord cercano al 21% de eficiencia (figura 18, derecha).

En conclusión, en este trabajo se reporta la fabricación de células solares de perovskita evaporada de alta eficiencia, empleando TiO<sub>2</sub> como capa transportadora de electrones. Gracias al uso de un óxido metálico depositado a baja temperatura se obtienen eficiencias superiores al 20%, siendo las más altas de su momento para la perovskita CH<sub>3</sub>NH<sub>3</sub>PbI<sub>3</sub>. Una capa fina de C<sub>60</sub> es depositada sobre el TiO<sub>2</sub> para pasivar las trampas electrónicas y ofrecer un buen sustrato para la deposición de la perovskita evaporada. Se observa un proceso de activación acelerado por la luz UV presente en el espectro AM1.5G completo. Este trabajo abre nuevos caminos para el uso de óxidos metálicos

en dispositivos que emplean perovskitas evaporadas y además usa procesos de baja temperatura, lo cual es interesante para el uso de sustratos flexibles como láminas de PET o en células solares de tipo tandem.

## 7.4 Capítulo 4: Pasivación molecular del MoO<sub>3</sub>: Alineamiento de bandas y protección de las capas transportadoras en células solares de perovskitas evaporadas.

### 7.4.1 Introducción

Como ya discutimos en capítulos anteriores, los óxidos metálicos son alternativas muy prometedoras de las capas orgánicas en células solares de perovskita. A pesar de que los dispositivos récord de tipo N-i-P emplean un óxido metálico en la parte N, siguen dependiendo de una capa dopada en la parte P para la inyección de huecos, generalmente Spiro-OMeTAD.<sup>57</sup> De manera similar, las mejores células solares de tipo P-i-N usan polímeros como el PEDOT:PSS o PTAA en la parte P.<sup>90</sup>

Los óxidos de metales de transición (TMOs) son candidatos excelentes para sustituir a estos materiales moleculares dado su excelente transporte de cargas, facilidad de deposición, función de trabajo variable y baja absorción parasítica. Por ejemplo, el NiO es ampliamente utilizado en células solares P-i-N alcanzando eficiencias superiores al 21%,<sup>93</sup> aunque debido a la alta temperatura de sinterizado necesaria no es un buen candidato para la estructura N-i-P.

Por otra parte, TMOs de tipo N como el MoO<sub>3</sub> son también candidatos interesantes dada su alta función de trabajo que permite una inyección eficiente de huecos.<sup>100</sup> Al ser un material de tipo N, el MoO<sub>3</sub> no puede actuar como bloqueador de electrones y debe ir acompañado de un material orgánico con un LUMO bajo que, a su vez, permita un crecimiento adecuado de la perovskita en la estructura P-i-N, como ya discutimos en el capítulo anterior. Los huecos fotogenerados pasan al HTL y recombinan con un electrón en la banda de conducción del MoO<sub>3</sub>, actuando así como capa inyectora de huecos (figura 20). También se ha sugerido que el MoO<sub>3</sub> transporta las cargas a través de estados electrónicos en el *bandgap* que pueden ser inducidos mediante temperatura o químicamente.<sup>61,94,102</sup>

Por ello, en este capítulo implementamos el uso de  $\text{MoO}_3$  en células solares de perovskita evaporada. En primer lugar, en la estructura de tipo P-i-N y, una vez optimizada su deposición, en la N-i-P desarrollada en el capítulo anterior. Así, conseguimos la primera configuración de alta eficiencia que emplea óxidos metálicos en ambas capas N y P en células solares de perovskita evaporada.

#### 7.4.2 Detalles experimentales y metodología

La estructura de los dispositivos P-i-N es: ITO /  $\text{MoO}_3$  (7 nm) / TaTm (10 nm) /  $\text{CH}_3\text{NH}_3\text{PbI}_3$  (590 nm) /  $\text{C}_{60}$  (25 nm) / BCP (7 nm) / Ag (100 nm) (figura 21, a).

El  $\text{MoO}_3$  y el TaTm actúan como capas de inyección y transporte de huecos. El  $\text{C}_{60}$  y el BCP como transporte e inyección de electrones. La capa de  $\text{MoO}_3$  fue evaporada sobre el ITO y calentada a 100 °C durante 10 minutos en atmósfera inerte. El resto de capas se prepararon siguiendo los procesos descritos en las secciones 7.2 y 7.3.

La estructura N-i-P es: ITO /  $\text{TiO}_2$  (30 nm) /  $\text{C}_{60}$  (10 nm) /  $\text{CH}_3\text{NH}_3\text{PbI}_3$  (590 nm) / TaTm (10 nm) / TPBi (2 nm) /  $\text{MoO}_3$  (7 nm) / Au (100 nm) (figura 23, a)

La parte N es idéntica a la de la sección 7.3, mientras que el TaTm dopado es sustituido por la combinación TPBi/ $\text{MoO}_3$ .

#### 7.4.3 Resultados y discusión

En primer lugar, se optimizó la deposición de  $\text{MoO}_3$  en la estructura P-i-N. Se observó que era necesario aplicar un tratamiento térmico tras la deposición de la capa para aumentar el FF y el  $V_{oc}$  bajo iluminación y la densidad de corriente en voltajes positivos en la curva en oscuridad (figura 21, b y c). Esto está atribuido a la formación de estados electrónicos por debajo del *bandgap* fruto de la creación de defectos en la estructura del  $\text{MoO}_3$ .<sup>101,103</sup> Para tratar de evitar el tratamiento térmico de la capa, potencialmente perjudicial en la estructura N-i-P, depositamos TPBi entre el  $\text{MoO}_3$  y el TaTm. Su profundo nivel HOMO puede mejorar la inyección de huecos, como han mostrado otros trabajos.<sup>104</sup> Usando TPBi conseguimos eficiencias casi idénticas a los

dispositivos donde se ha tratado térmicamente la capa de MoO<sub>3</sub> (tabla 3), con eficiencias cercanas al 19%.

Se atribuye esta mejora, no solo la alta energía de ionización del TPBi, sino a la presencia de nitrógenos piridínicos, los cuales pueden reaccionar con el MoO<sub>3</sub> a través de una transferencia de carga de los electrones solitarios del nitrógeno, induciendo así químicamente los estados electrónicos antes descritos.<sup>105,106</sup> Para comprobar esto se usaron moléculas con un HOMO similar pero químicamente distintas al TPBi (figura 22). Se observó que, a pesar de que hay una mejora del FF y del V<sub>oc</sub>, no llegan a ser tan altos como con el uso de TPBi o con el tratamiento térmico del MoO<sub>3</sub>, mostrando así la importancia de la naturaleza química de la molécula usada y no sólo sus niveles energéticos.

Una vez optimizada la deposición sin tratamiento térmico en la arquitectura P-i-N, se implementó el uso de MoO<sub>3</sub> en N-i-P. Cuando no se usa TPBi se observa una recombinación muy elevada, disminuyendo el V<sub>oc</sub> drásticamente. Esto se atribuye a la penetración del MoO<sub>3</sub> en el TaTm, acabando así con su selectividad a los huecos y el bloqueo de electrones. Al incorporar tan sólo 2 nm de TPBi se previene esta penetración del MoO<sub>3</sub>, obteniendo valores normales de V<sub>oc</sub> y FF, con eficiencias superiores al 18%. Aumentar el grosor del TPBi de 2 a 5 nm aumenta considerablemente la resistencia en serie y reduce drásticamente el FF, mostrando que el MoO<sub>3</sub> parece reaccionar solamente con la superficie del TPBi (figura 23 y tabla 4).

Para demostrar el efecto protector del TPBi a través de esta interacción química con el MoO<sub>3</sub> se llevaron a cabo dos experimentos. En uno se aumentó el grosor total del TaTm, variándolo de 12 a 25 nm en lugar de usar 10 nm + 2 nm de TPBi. Fueron necesarios al menos 20 nm totales de TaTm para conseguir el mismo efecto protector que 2 nm de TPBi, mostrando que la protección no proviene del aumento de grosor total. En el segundo experimento, se depositó sobre el MoO<sub>3</sub> dos moléculas similares al TPBi en términos de niveles energéticos, BCP y TCTA, donde la primera posee nitrógenos piridínicos mientras que la segunda no. Se observó que al usar 2 nm de BCP se obtiene el mismo efecto protector que con TPBi, aumentando el V<sub>oc</sub> y el FF, mientras que con TCTA se sigue observando un aumento en la recombinación al no bloquear la penetración del MoO<sub>3</sub>, mostrando así la importancia de la naturaleza química de la molécula usada (figura 24 y tabla 5).

En conclusión, la inserción de una capa ultrafina de una molécula con alta energía de ionización y nitrógenos piridínicos nos ha permitido el uso de un óxido metálico, particularmente MoO<sub>3</sub>, como capa inyectora de huecos en la

estructura P-i-N sin la necesidad de tratamiento térmico. Esta molécula induce químicamente estados electrónicos en el *bandgap* del MoO<sub>3</sub> necesarios para el correcto transporte de huecos y su alta energía de ionización permite un mejor alineamiento en las bandas electrónicas. Cuando el MoO<sub>3</sub> se usa en la configuración N-i-P se observa como éste penetra en las capas depositadas previamente dada la alta energía cinética de la evaporación. Con tan sólo 2 nm de TPBi se previene esta penetración gracias a la formación de especies TPBi-MoO<sub>3</sub> en la superficie que protegen las capas subyacentes, consiguiendo así una eficiencia cercana al 19%, siendo ésta la primera estructura con dos óxidos metálicos de alta eficiencia usada en células solares de perovskita evaporada.

## 7.5 Capítulo 5: Células solares de perovskita: estables en condiciones espaciales

En este trabajo se pone a prueba la estructura de tipo P-i-N desarrollada en el capítulo anterior en condiciones espaciales. Elegimos esta configuración dada su compatibilidad con dispositivos tandem silicio-perovskita, fundamental para futuras aplicaciones espaciales. Exponemos más de 60 células solares a dosis de radiación electrónica de 1 MeV, simulando condiciones de gran altitud. No se observan cambios en la eficiencia de las células solares incluso usando dosis acumuladas de  $10^{16}$  e<sup>-</sup>/cm<sup>2</sup>. Además, si los dispositivos presentan un funcionamiento por debajo de la media, se observa una mejora tras la irradiación. El uso de un óxido metálico como capa frontal fue fundamental para conseguir una robustez superior, sin prácticamente cambios observados en la inyección y extracción de cargas tras la irradiación.

### 7.5.1 Introducción

La rápida evolución en la eficiencia de las células solares de perovskita las sitúa como prometedoras candidatas para el uso espacial. Actualmente, las principales tecnologías usadas en el espacio son los compuestos de los grupos III-V y las células solares de silicio cristalino, las cuales deben resistir radiación cósmica de alta energía debido a la reducción del campo magnético terrestre con la altura.<sup>110</sup> A pesar de ello, estas tecnologías tienen inconvenientes, como

el bajo ratio de potencia/peso, el coste de producción, y su durabilidad en el espacio.<sup>111,112</sup>

El uso de perovskitas permite la fabricación de células solares ligeras gracias a su alto coeficiente de absorción<sup>20</sup> y la gran distancia de difusión de los portadores de carga,<sup>126</sup> consiguiendo así un impresionante ratio de potencia por peso de 26 W/g<sup>128</sup> con un grosor en general menor a 1 micrómetro.<sup>15</sup> Además, las células solares de perovskita evaporada destacan gracias a la ausencia de disolventes volátiles y su aun mayor distancia de difusión de los portadores de carga<sup>114</sup> y han demostrado cuán importante es la baja densidad de defectos de la perovskita para una mayor resistencia a los electrones de alta energía.<sup>117,119</sup>

Por todo ello, en este trabajo pongo a prueba las células solares de perovskita de tipo P-i-N desarrolladas en el capítulo anterior bajo irradiación de electrones, simulando condiciones espaciales. La combinación de un óxido metálico como capa frontal y perovskita evaporada lleva a la creación de un sistema muy robusto con mínimos cambios en la eficiencia tras ser expuesto a dosis altas de electrones de 1 MeV, por primera vez en la literatura científica.

### 7.5.2 Detalles experimentales y metodología

La preparación y caracterización de los dispositivos se hizo siguiendo un método análogo al de la sección 7.4, con la única diferencia del sustrato empleado. Usamos sustratos de cuarzo con ITO depositado para evitar el oscurecimiento de este por el efecto de los electrones. Se realizó el patrón de ITO deseado usando HCl gas como agente de grabado químico. Los dispositivos se encapsularon usando una placa de aluminio con una resina curable con luz ultravioleta en los bordes a modo de agente encapsulante. Los experimentos de irradiación se llevaron a cabo en la universidad de Delft usando electrones de 1 MeV generados en un acelerador de Van de Graaf, a 20 °C. Así, se generaron dosis acumuladas de  $10^{14}$  a  $10^{16}$  e<sup>-</sup>/cm<sup>2</sup>. La estructura de los dispositivos es: Vidrio o cuarzo / ITO / MoO<sub>3</sub> (7 nm) / TaTm (10 mn) / CH<sub>3</sub>NH<sub>3</sub>PbI<sub>3</sub> (600 nm) / C<sub>60</sub> (25 nm) / BCP (7 nm) / Ag (100 nm).

### 7.5.3 Resultados y discusión

Los primeros experimentos de irradiación se realizaron en la configuración clásica con vidrio como substrato. Los electrones de alta energía indujeron una coloración marrón debido a la presencia de impurezas.<sup>125</sup> Ello conllevó a una reducción de la corriente del dispositivo por absorción parásita. Por ello usamos sustratos de cuarzo para evitar este inconveniente. Este segundo grupo de células se irradió con dosis acumuladas de  $10^{14}$ ,  $10^{15}$  y  $10^{16}$  e<sup>-</sup>/cm<sup>2</sup>. En la figura 25 se muestran los resultados obtenidos para cada dosis de electrones. De media, tras la irradiación se obtuvieron los siguientes resultados:  $J_{sc}$  de 21.5 mA/cm<sup>2</sup>,  $V_{oc}$  de 1.105 V y FF de 80%, dando una PCE de ~19 %.

Los dispositivos con un funcionamiento por debajo de la media mostraron una mejora significativa tras la irradiación, aumentando el voltaje y la corriente. Esto se atribuye a la pasivación de trampas en la perovskita. Esto se confirmó mediante medidas de fotoluminiscencia, mostrando una señal de emisión extra a 650 nm dependiente de la dosis de irradiación (figura 26, b). Otros trabajos ya han reportado anteriormente que se debe a la formación de fases ricas en PbI<sub>2</sub> por la energía cinética de los electrones.<sup>120</sup> Nuestra hipótesis es que estas fases son las que pasivan las trampas electrónicas en la perovskita, incrementando así la recolección de cargas y reduciendo la recombinación.

Análisis de la superficie de la perovskita y de la cristalinidad también muestran que no hay cambios en la perovskita tras la irradiación (figura 27). Otras técnicas se llevaron a cabo en la universidad de Delft, como medidas de conductividad por microondas en el tiempo (TRMC), mostrando cambios mínimos en el tiempo de vida de los portadores de carga.

En conclusión, en este trabajo exponemos las células solares de perovskita evaporada desarrolladas en el capítulo anterior a dosis altas de electrones de 1 MeV. Demostramos sin ninguna duda que esta configuración con un óxido metálico como capa frontal es muy robusta ante estas condiciones extremas, alcanzando eficiencias superiores al 18% e incluso mejorando el funcionamiento y recuperándose tras la irradiación. Esto se atribuye a la pasivación de defectos y trampas por la formación de fases ricas en PbI<sub>2</sub> inducidas por la energía cinética de los electrones, demostrado mediante medidas de fotoluminiscencia y TRMC.

## 7.6 Capítulo 6: Conclusiones

El trabajo desarrollado en esta tesis persigue la sustitución de las capas orgánicas dopadas por óxidos de metales de transición en células solares de perovskita evaporada de alta eficiencia, con el fin de aumentar su estabilidad y eficiencia. Así, conseguimos una estructura N-i-P funcional y eficiente basada en óxidos metálicos en ambos contactos y una estructura P-i-N estable y eficiente diseñada para sobrevivir a condiciones espaciales gracias al uso de un óxido metálico como capa frontal.

En el **capítulo 3** sustituyo la capa dopada de tipo N por  $\text{TiO}_2$  en la estructura N-i-P. Ello reduce la absorción parásita y la recombinación de los portadores de carga, incrementando así la eficiencia a valores superiores al 20%, con uno de los voltajes más altos para la perovskita MAPI. Se encontró un proceso de activación, acelerado bajo iluminación AM1.5G con una ligera componente UV, mejorando el alineamiento de las bandas entre el óxido metálico y la perovskita. Gracias a ello y depositando la perovskita con un grosor aproximado de 1 micrómetro se consiguen eficiencias cercanas al 21%.

En el **capítulo 4** continúo este trabajo buscando la sustitución total de las capas orgánicas dopadas en la estructura N-i-P. El uso de  $\text{MoO}_3$  se optimizó primero en la estructura P-i-N, encontrando la necesidad de aplicar un tratamiento térmico a este óxido para conseguir un transporte de huecos óptimo a través de la formación de estados electrónicos. Desarrollé un método para inducir estos estados químicamente depositando 1.5 nm de TPBi encima del  $\text{MoO}_3$ . Así, consigo evitar el tratamiento térmico, que puede ser perjudicial para la estructura N-i-P, obteniendo así eficiencias superiores al 19%. Al implementar el  $\text{MoO}_3$  en la estructura N-i-P se observa que este difunde sobre las capas ya depositadas, disminuyendo el  $V_{oc}$ . El uso de TPBi, antes de depositar el  $\text{MoO}_3$  frena la difusión de éste debido a la interacción química antes descrita. Así, se consigue una estructura N-i-P con óxidos metálicos en ambos contactos con eficiencias superiores al 18% por primera vez en perovskita evaporada.

Finalmente, en el **capítulo 5** pongo a prueba la estabilidad de la estructura P-i-N desarrollada en el capítulo anterior bajo distintas dosis acumuladas de electrones de 1 MeV, simulando décadas en el espacio. Usando sustratos de cuarzo resistentes a altas dosis de electrones se obtuvieron eficiencias superiores al 18% tras la irradiación bajo dosis acumuladas de  $10^{14}$ ,  $10^{15}$ , e incluso  $10^{16} \text{ e}^-/\text{cm}^2$ . También se observó un efecto de recuperación de las

células solares con eficiencias por debajo de la media. Esto se atribuye a la formación de fases ricas en  $\text{PbI}_2$  por el efecto de la energía cinética de los electrones, actuando como agente pasivante de defectos electrónicos y trampas, confirmado por TRMC y PL. Así, demostramos el potencial de las células solares de perovskita evaporada con un óxido metálico como capa frontal en condiciones espaciales.



## 8. Bibliography

- (1) Hannah Ritchie and Max Roser. Electricity Mix <https://ourworldindata.org/electricity-mix>.
- (2) J., D. F. Search for Artificial Stellar Sources of Infrared Radiation. *Science* (80-. ). **1960**, *131* (3414), 1667–1668. <https://doi.org/10.1126/science.131.3414.1667>.
- (3) Photovoltaics report, Fraunhofer Institute for Solar Energy Systems, ISE <https://www.ise.fraunhofer.de/content/dam/ise/de/documents/publications/studies/Photovoltaics-Report.pdf>.
- (4) Green, M.; Dunlop, E.; Hohl-Ebinger, J.; Yoshita, M.; Kopidakis, N.; Hao, X. Solar Cell Efficiency Tables (Version 57). *Prog. Photovoltaics Res. Appl.* **2021**, *29* (1), 3–15. <https://doi.org/https://doi.org/10.1002/pip.3371>.
- (5) Rolston, N.; Scheideler, W. J.; Flick, A. C.; Chen, J. P.; Elmaraghi, H.; Sleugh, A.; Zhao, O.; Woodhouse, M.; Dauskardt, R. H. Rapid Open-Air Fabrication of Perovskite Solar Modules. *Joule* **2020**, *4* (12), 2675–2692. <https://doi.org/10.1016/j.joule.2020.11.001>.
- (6) Zhao, X.; Wang, M. Organic Hole-Transporting Materials for Efficient Perovskite Solar Cells. *Mater. Today Energy* **2018**, *7*, 208–220. <https://doi.org/https://doi.org/10.1016/j.mtener.2017.09.011>.
- (7) Umebayashi, T.; Asai, K.; Kondo, T.; Nakao, A. Electronic Structures of Lead Iodide Based Low-Dimensional Crystals. *Phys. Rev. B* **2003**, *67* (15), 155405. <https://doi.org/10.1103/PhysRevB.67.155405>.
- (8) Chang, Y. H.; Park, C. H.; Matsuishi, K. First-Principles Study of the Structural and the Electronic Properties of the Lead-Halide-Based Inorganic-Organic Perovskites (CH<sub>3</sub>NH<sub>3</sub>)PbX<sub>3</sub> and CsPbX<sub>3</sub> (X = Cl, Br, I). *J. Korean Phys. Soc.* **2004**, *44* (4), 889–893.
- (9) Brivio, F.; Walker, A. B.; Walsh, A. Structural and Electronic Properties of Hybrid Perovskites for High-Efficiency Thin-Film Photovoltaics from First-Principles. *APL Mater.* **2013**, *1* (4), 42111. <https://doi.org/10.1063/1.4824147>.
- (10) Tao, S.; Schmidt, I.; Brocks, G.; Jiang, J.; Tranca, I.; Meerholz, K.; Olthof, S. Absolute Energy Level Positions in Tin- and Lead-Based Halide Perovskites. *Nat. Commun.* **2019**, *10* (1), 2560. <https://doi.org/10.1038/s41467-019-10468-7>.

- (11) Filip, M. R.; Eperon, G. E.; Snaith, H. J.; Giustino, F. Steric Engineering of Metal-Halide Perovskites with Tunable Optical Band Gaps. *Nat. Commun.* **2014**, 5 (1), 5757. <https://doi.org/10.1038/ncomms6757>.
- (12) Kawamura, Y.; Mashiyama, H.; Hasebe, K. Structural Study on Cubic-Tetragonal Transition of CH<sub>3</sub>NH<sub>3</sub>PbI<sub>3</sub>. *J. Phys. Soc. Japan* **2002**, 71 (7), 1694–1697. <https://doi.org/10.1143/JPSJ.71.1694>.
- (13) Baikie, T.; Barrow, N. S.; Fang, Y.; Keenan, P. J.; Slater, P. R.; Piltz, R. O.; Gutmann, M.; Mhaisalkar, S. G.; White, T. J. A Combined Single Crystal Neutron/X-Ray Diffraction and Solid-State Nuclear Magnetic Resonance Study of the Hybrid Perovskites CH<sub>3</sub>NH<sub>3</sub>PbX<sub>3</sub> (X = I, Br and Cl). *J. Mater. Chem. A* **2015**, 3 (17), 9298–9307. <https://doi.org/10.1039/C5TA01125F>.
- (14) Palazon, F.; Pérez-del-Rey, D.; Dänekamp, B.; Dreessen, C.; Sessolo, M.; Boix, P. P.; Bolink, H. J. Room-Temperature Cubic Phase Crystallization and High Stability of Vacuum-Deposited Methylammonium Lead Triiodide Thin Films for High-Efficiency Solar Cells. *Adv. Mater.* **2019**, 31 (39). <https://doi.org/10.1002/adma.201902692>.
- (15) Yin, W.-J.; Shi, T.; Yan, Y. Unique Properties of Halide Perovskites as Possible Origins of the Superior Solar Cell Performance. *Adv. Mater.* **2014**, 26 (27), 4653–4658. <https://doi.org/https://doi.org/10.1002/adma.201306281>.
- (16) Yin, W.-J.; Shi, T.; Yan, Y. Unusual Defect Physics in CH<sub>3</sub>NH<sub>3</sub>PbI<sub>3</sub> Perovskite Solar Cell Absorber. *Appl. Phys. Lett.* **2014**, 104 (6), 63903. <https://doi.org/10.1063/1.4864778>.
- (17) Sun, S.; Salim, T.; Mathews, N.; Duchamp, M.; Boothroyd, C.; Xing, G.; Sum, T. C.; Lam, Y. M. The Origin of High Efficiency in Low-Temperature Solution-Processable Bilayer Organometal Halide Hybrid Solar Cells. *Energy Environ. Sci.* **2014**, 7 (1), 399–407. <https://doi.org/10.1039/C3EE43161D>.
- (18) Aharon, S.; Gamliel, S.; Cohen, B. El; Etgar, L. Depletion Region Effect of Highly Efficient Hole Conductor Free CH<sub>3</sub>NH<sub>3</sub>PbI<sub>3</sub> Perovskite Solar Cells. *Phys. Chem. Chem. Phys.* **2014**, 16 (22), 10512–10518. <https://doi.org/10.1039/C4CP00460D>.
- (19) Schulz, P.; Edri, E.; Kirmayer, S.; Hodes, G.; Cahen, D.; Kahn, A. Interface Energetics in Organo-Metal Halide Perovskite-Based Photovoltaic Cells. *Energy Environ. Sci.* **2014**, 7 (4), 1377–1381. <https://doi.org/10.1039/C4EE00168K>.
- (20) De Wolf, S.; Holovsky, J.; Moon, S.-J.; Löper, P.; Niesen, B.; Ledinsky,

- M.; Haug, F.-J.; Yum, J.-H.; Ballif, C. Organometallic Halide Perovskites: Sharp Optical Absorption Edge and Its Relation to Photovoltaic Performance. *J. Phys. Chem. Lett.* **2014**, 5 (6), 1035–1039. <https://doi.org/10.1021/jz500279b>.
- (21) Lin, Q.; Armin, A.; Nagiri, R. C. R.; Burn, P. L.; Meredith, P. Electro-Optics of Perovskite Solar Cells. *Nat. Photonics* **2015**, 9 (2), 106–112. <https://doi.org/10.1038/nphoton.2014.284>.
- (22) D’Innocenzo, V.; Grancini, G.; Alcocer, M. J. P.; Kandada, A. R. S.; Stranks, S. D.; Lee, M. M.; Lanzani, G.; Snaith, H. J.; Petrozza, A. Excitons versus Free Charges in Organo-Lead Tri-Halide Perovskites. *Nat. Commun.* **2014**, 5 (1), 3586. <https://doi.org/10.1038/ncomms4586>.
- (23) Sapori, D.; Kepenekian, M.; Pedesseau, L.; Katan, C.; Even, J. Quantum Confinement and Dielectric Profiles of Colloidal Nanoplatelets of Halide Inorganic and Hybrid Organic–Inorganic Perovskites. *Nanoscale* **2016**, 8 (12), 6369–6378. <https://doi.org/10.1039/C5NR07175E>.
- (24) Fang, H.-H.; Raissa, R.; Abdu-Aguye, M.; Adjokatse, S.; Blake, G. R.; Even, J.; Loi, M. A. Photophysics of Organic–Inorganic Hybrid Lead Iodide Perovskite Single Crystals. *Adv. Funct. Mater.* **2015**, 25 (16), 2378–2385. <https://doi.org/https://doi.org/10.1002/adfm.201404421>.
- (25) Stoumpos, C. C.; Malliakas, C. D.; Kanatzidis, M. G. Semiconducting Tin and Lead Iodide Perovskites with Organic Cations: Phase Transitions, High Mobilities, and Near-Infrared Photoluminescent Properties. *Inorg. Chem.* **2013**, 52 (15), 9019–9038. <https://doi.org/10.1021/ic401215x>.
- (26) Herz, L. M. Charge-Carrier Mobilities in Metal Halide Perovskites: Fundamental Mechanisms and Limits. *ACS Energy Lett.* **2017**, 2 (7), 1539–1548. <https://doi.org/10.1021/acsenergylett.7b00276>.
- (27) Coropceanu, V.; Cornil, J.; da Silva Filho, D. A.; Olivier, Y.; Silbey, R.; Brédas, J.-L. Charge Transport in Organic Semiconductors. *Chem. Rev.* **2007**, 107 (4), 926–952. <https://doi.org/10.1021/cr050140x>.
- (28) Guichuan, X.; Nripan, M.; Shuangyong, S.; Sien, L. S.; Ming, L. Y.; Michael, G.; Subodh, M.; Chien, S. T. Long-Range Balanced Electron- and Hole-Transport Lengths in Organic-Inorganic CH<sub>3</sub>NH<sub>3</sub>PbI<sub>3</sub>. *Science* (80-. .). **2013**, 342 (6156), 344–347. <https://doi.org/10.1126/science.1243167>.
- (29) D., S. S.; E., E. G.; Giulia, G.; Christopher, M.; P., A. M. J.; Tomas, L.; M., H. L.; Annamaria, P.; J., S. H. Electron-Hole Diffusion Lengths Exceeding 1 Micrometer in an Organometal Trihalide Perovskite Absorber.

- Science* (80-. ). **2013**, 342 (6156), 341–344. <https://doi.org/10.1126/science.1243982>.
- (30) Gonzalez-Pedro, V.; Juarez-Perez, E. J.; Arsyad, W.-S.; Barea, E. M.; Fabregat-Santiago, F.; Mora-Sero, I.; Bisquert, J. General Working Principles of CH<sub>3</sub>NH<sub>3</sub>PbX<sub>3</sub> Perovskite Solar Cells. *Nano Lett.* **2014**, 14 (2), 888–893. <https://doi.org/10.1021/nl404252e>.
- (31) Shi, D.; Adinolfi, V.; Comin, R.; Yuan, M.; Alarousu, E.; Buin, A.; Chen, Y.; Hoogland, S.; Rothenberger, A.; Katsiev, K.; et al. Low Trap-State Density and Long Carrier Diffusion in Organolead Trihalide Perovskite Single Crystals. *Science* (80-. ). **2015**, 347 (6221), 519–522. <https://doi.org/10.1126/science.aaa2725>.
- (32) Pérez-Del-Rey, D.; Boix, P. P.; Sessolo, M.; Hadipour, A.; Bolink, H. J. Interfacial Modification for High-Efficiency Vapor-Phase-Deposited Perovskite Solar Cells Based on a Metal Oxide Buffer Layer. *J. Phys. Chem. Lett.* **2018**, 9 (5). <https://doi.org/10.1021/acs.jpclett.7b03361>.
- (33) Qingfeng, D.; Yanjun, F.; Yuchuan, S.; Padhraic, M.; Jie, Q.; Lei, C.; Jinsong, H. Electron-Hole Diffusion Lengths > 175 Mm in Solution-Grown CH<sub>3</sub>NH<sub>3</sub>PbI<sub>3</sub> Single Crystals. *Science* (80-. ). **2015**, 347 (6225), 967–970. <https://doi.org/10.1126/science.aaa5760>.
- (34) Ran, C.; Xu, J.; Gao, W.; Huang, C.; Dou, S. Defects in Metal Triiodide Perovskite Materials towards High-Performance Solar Cells: Origin, Impact, Characterization, and Engineering. *Chem. Soc. Rev.* **2018**, 47 (12), 4581–4610. <https://doi.org/10.1039/C7CS00868F>.
- (35) Eperon, G. E.; Stranks, S. D.; Menelaou, C.; Johnston, M. B.; Herz, L. M.; Snaith, H. J. Formamidinium Lead Trihalide: A Broadly Tunable Perovskite for Efficient Planar Heterojunction Solar Cells. *Energy Environ. Sci.* **2014**, 7 (3), 982–988. <https://doi.org/10.1039/C3EE43822H>.
- (36) Moore, D. T.; Sai, H.; Tan, K. W.; Smilgies, D.-M.; Zhang, W.; Snaith, H. J.; Wiesner, U.; Estroff, L. A. Crystallization Kinetics of Organic-Inorganic Trihalide Perovskites and the Role of the Lead Anion in Crystal Growth. *J. Am. Chem. Soc.* **2015**, 137 (6), 2350–2358. <https://doi.org/10.1021/ja512117e>.
- (37) Jeon, N. J.; Noh, J. H.; Kim, Y. C.; Yang, W. S.; Ryu, S.; Seok, S. Il. Solvent Engineering for High-Performance Inorganic–Organic Hybrid Perovskite Solar Cells. *Nat. Mater.* **2014**, 13 (9), 897–903. <https://doi.org/10.1038/nmat4014>.
- (38) Himchan, C.; Su-Hun, J.; Min-Ho, P.; Young-Hoon, K.; Christoph, W.;

- Chang-Lyoul, L.; Hyuck, H. J.; Aditya, S.; NoSoung, M.; Seunghyup, Y.; et al. Overcoming the Electroluminescence Efficiency Limitations of Perovskite Light-Emitting Diodes. *Science (80-. ).* **2015**, *350* (6265), 1222–1225. <https://doi.org/10.1126/science.aad1818>.
- (39) Jung, J. W.; Williams, S. T.; Jen, A. K.-Y. Low-Temperature Processed High-Performance Flexible Perovskite Solar Cells via Rationally Optimized Solvent Washing Treatments. *RSC Adv.* **2014**, *4* (108), 62971–62977. <https://doi.org/10.1039/C4RA13212B>.
- (40) Xiao, M.; Huang, F.; Huang, W.; Dkhissi, Y.; Zhu, Y.; Etheridge, J.; Gray-Weale, A.; Bach, U.; Cheng, Y.-B.; Spiccia, L. A Fast Deposition-Crystallization Procedure for Highly Efficient Lead Iodide Perovskite Thin-Film Solar Cells. *Angew. Chemie Int. Ed.* **2014**, *53* (37), 9898–9903. <https://doi.org/https://doi.org/10.1002/anie.201405334>.
- (41) Zhou, Y.; Yang, M.; Wu, W.; Vasiliev, A. L.; Zhu, K.; Padture, N. P. Room-Temperature Crystallization of Hybrid-Perovskite Thin Films via Solvent–Solvent Extraction for High-Performance Solar Cells. *J. Mater. Chem. A* **2015**, *3* (15), 8178–8184. <https://doi.org/10.1039/C5TA00477B>.
- (42) Burschka, J.; Pellet, N.; Moon, S.-J.; Humphry-Baker, R.; Gao, P.; Nazeeruddin, M. K.; Grätzel, M. Sequential Deposition as a Route to High-Performance Perovskite-Sensitized Solar Cells. *Nature* **2013**, *499* (7458), 316–319. <https://doi.org/10.1038/nature12340>.
- (43) Liang, K.; Mitzi, D. B.; Prikas, M. T. Synthesis and Characterization of Organic-Inorganic Perovskite Thin Films Prepared Using a Versatile Two-Step Dipping Technique. *Chem. Mater.* **1998**, *10* (1), 403–411. <https://doi.org/10.1021/cm970568f>.
- (44) Im, J.-H.; Jang, I.-H.; Pellet, N.; Grätzel, M.; Park, N.-G. Growth of CH<sub>3</sub>NH<sub>3</sub>PbI<sub>3</sub> Cuboids with Controlled Size for High-Efficiency Perovskite Solar Cells. *Nat. Nanotechnol.* **2014**, *9* (11), 927–932. <https://doi.org/10.1038/nnano.2014.181>.
- (45) Im, J.-H.; Kim, H.-S.; Park, N.-G. Morphology-Photovoltaic Property Correlation in Perovskite Solar Cells: One-Step versus Two-Step Deposition of CH<sub>3</sub>NH<sub>3</sub>PbI<sub>3</sub>. *APL Mater.* **2014**, *2* (8), 81510. <https://doi.org/10.1063/1.4891275>.
- (46) Mitzi, D. B.; Prikas, M. T.; Chondroudis, K. Thin Film Deposition of Organic-Inorganic Hybrid Materials Using a Single Source Thermal Ablation Technique. *Chem. Mater.* **1999**, *11* (3), 542–544. <https://doi.org/10.1021/cm9811139>.

- (47) Ahmad, S.; Hanmandlu, C.; Kanaujia, P. K.; Prakash, G. V. Direct Deposition Strategy for Highly Ordered Inorganic Organic Perovskite Thin Films and Their Optoelectronic Applications. *Opt. Mater. Express* **2014**, *4* (7), 1313–1323. <https://doi.org/10.1364/OME.4.001313>.
- (48) Longo, G.; Gil-Escrig, L.; Degen, M. J.; Sessolo, M.; Bolink, H. J. Perovskite Solar Cells Prepared by Flash Evaporation. *Chem. Commun.* **2015**, *51* (34), 7376–7378. <https://doi.org/10.1039/C5CC01103E>.
- (49) Liu, M.; Johnston, M. B.; Snaith, H. J. Efficient Planar Heterojunction Perovskite Solar Cells by Vapour Deposition. *Nature* **2013**, *501* (7467), 395–398. <https://doi.org/10.1038/nature12509>.
- (50) Malinkiewicz, O.; Yella, A.; Lee, Y. H.; Espallargas, G. M.; Graetzel, M.; Nazeeruddin, M. K.; Bolink, H. J. Perovskite Solar Cells Employing Organic Charge-Transport Layers. *Nat. Photonics* **2014**, *8* (2), 128–132. <https://doi.org/10.1038/nphoton.2013.341>.
- (51) Im, J.-H.; Lee, C.-R.; Lee, J.-W.; Park, S.-W.; Park, N.-G. 6.5% Efficient Perovskite Quantum-Dot-Sensitized Solar Cell. *Nanoscale* **2011**, *3* (10), 4088–4093. <https://doi.org/10.1039/C1NR10867K>.
- (52) Li, H.; Shi, W.; Huang, W.; Yao, E.-P.; Han, J.; Chen, Z.; Liu, S.; Shen, Y.; Wang, M.; Yang, Y. Carbon Quantum Dots/TiO<sub>x</sub> Electron Transport Layer Boosts Efficiency of Planar Heterojunction Perovskite Solar Cells to 19%. *Nano Lett.* **2017**, *17* (4), 2328–2335. <https://doi.org/10.1021/acs.nanolett.6b05177>.
- (53) Wanyi, N.; Hsinhan, T.; Reza, A.; Jean-Christophe, B.; J., N. A.; Gautam, G.; J., C. J.; Manish, C.; Sergei, T.; A., A. M.; et al. High-Efficiency Solution-Processed Perovskite Solar Cells with Millimeter-Scale Grains. *Science* (80-. ). **2015**, *347* (6221), 522–525. <https://doi.org/10.1126/science.aaa0472>.
- (54) You, J.; Meng, L.; Song, T.-B.; Guo, T.-F.; Yang, Y. (Michael); Chang, W.-H.; Hong, Z.; Chen, H.; Zhou, H.; Chen, Q.; et al. Improved Air Stability of Perovskite Solar Cells via Solution-Processed Metal Oxide Transport Layers. *Nat. Nanotechnol.* **2016**, *11* (1), 75–81. <https://doi.org/10.1038/nnano.2015.230>.
- (55) Park, J. H.; Seo, J.; Park, S.; Shin, S. S.; Kim, Y. C.; Jeon, N. J.; Shin, H.-W.; Ahn, T. K.; Noh, J. H.; Yoon, S. C.; et al. Efficient CH<sub>3</sub>NH<sub>3</sub>PbI<sub>3</sub> Perovskite Solar Cells Employing Nanostructured P-Type NiO Electrode Formed by a Pulsed Laser Deposition. *Adv. Mater.* **2015**, *27* (27), 4013–4019. <https://doi.org/https://doi.org/10.1002/adma.201500523>.
- (56) Liang, P.-W.; Chueh, C.-C.; Williams, S. T.; Jen, A. K.-Y. Roles of

- Fullerene-Based Interlayers in Enhancing the Performance of Organometal Perovskite Thin-Film Solar Cells. *Adv. Energy Mater.* **2015**, *5* (10), 1402321. <https://doi.org/https://doi.org/10.1002/aenm.201402321>.
- (57) Jeong, J.; Kim, M.; Seo, J.; Lu, H.; Ahlawat, P.; Mishra, A.; Yang, Y.; Hope, M. A.; Eickemeyer, F. T.; Kim, M.; et al. Pseudo-Halide Anion Engineering for  $\alpha$ -FAPbI<sub>3</sub> Perovskite Solar Cells. *Nature* **2021**, *592* (7854), 381–385. <https://doi.org/10.1038/s41586-021-03406-5>.
- (58) Qiu, C.; Xie, Z.; Chen, H.; Wong, M.; Kwok, H. S. Comparative Study of Metal or Oxide Capped Indium–Tin Oxide Anodes for Organic Light-Emitting Diodes. *J. Appl. Phys.* **2003**, *93* (6), 3253–3258. <https://doi.org/10.1063/1.1556184>.
- (59) Shrotriya, V.; Li, G.; Yao, Y.; Chu, C.-W.; Yang, Y. Transition Metal Oxides as the Buffer Layer for Polymer Photovoltaic Cells. *Appl. Phys. Lett.* **2006**, *88* (7), 73508. <https://doi.org/10.1063/1.2174093>.
- (60) Young, K. J.; Kwanghee, L.; E., C. N.; Daniel, M.; Thuc-Quyen, N.; Mark, D.; J., H. A. Efficient Tandem Polymer Solar Cells Fabricated by All-Solution Processing. *Science (80-. ).* **2007**, *317* (5835), 222–225. <https://doi.org/10.1126/science.1141711>.
- (61) Hancox, I.; Rochford, L. A.; Clare, D.; Sullivan, P.; Jones, T. S. Utilizing N-Type Vanadium Oxide Films as Hole-Extracting Layers for Small Molecule Organic Photovoltaics. *Appl. Phys. Lett.* **2011**, *99* (1), 13304. <https://doi.org/10.1063/1.3607478>.
- (62) Tan, Z.; Li, L.; Cui, C.; Ding, Y.; Xu, Q.; Li, S.; Qian, D.; Li, Y. Solution-Processed Tungsten Oxide as an Effective Anode Buffer Layer for High-Performance Polymer Solar Cells. *J. Phys. Chem. C* **2012**, *116* (35), 18626–18632. <https://doi.org/10.1021/jp304878u>.
- (63) Tan, Z.; Zhang, W.; Cui, C.; Ding, Y.; Qian, D.; Xu, Q.; Li, L.; Li, S.; Li, Y. Solution-Processed Vanadium Oxide as a Hole Collection Layer on an ITO Electrode for High-Performance Polymer Solar Cells. *Phys. Chem. Chem. Phys.* **2012**, *14* (42), 14589–14595. <https://doi.org/10.1039/C2CP43125D>.
- (64) Chen, S.; Manders, J. R.; Tsang, S.-W.; So, F. Metal Oxides for Interface Engineering in Polymer Solar Cells. *J. Mater. Chem.* **2012**, *22* (46), 24202–24212. <https://doi.org/10.1039/C2JM33838F>.
- (65) Nie, G.; Peng, J.; Lan, L.; Xu, R.; Zou, J.; Cao, Y. Tuning on Threshold Voltage of Organic Field-Effect Transistor with a Copper Oxide Layer. *Org. Electron.* **2011**, *12* (3), 429–434.

- <https://doi.org/https://doi.org/10.1016/j.orgel.2010.12.012>.
- (66) Darmawan, P.; Minari, T.; Kumatani, A.; Li, Y.; Liu, C.; Tsukagoshi, K. Reduction of Charge Injection Barrier by 1-Nm Contact Oxide Interlayer in Organic Field Effect Transistors. *Appl. Phys. Lett.* **2012**, *100* (1), 13303. <https://doi.org/10.1063/1.3673842>.
- (67) Yu, X.; Yu, J.; Zhou, J.; Jiang, Y. Organic Field-Effect Transistors with Nearly Non-Injection Barrier from Source/Drain Electrodes to Pentacene. *Synth. Met.* **2012**, *162* (11), 936–940. <https://doi.org/https://doi.org/10.1016/j.synthmet.2012.03.012>.
- (68) Kumaki, D.; Umeda, T.; Tokito, S. Reducing the Contact Resistance of Bottom-Contact Pentacene Thin-Film Transistors by Employing a MoO<sub>x</sub> Carrier Injection Layer. *Appl. Phys. Lett.* **2008**, *92* (1), 13301. <https://doi.org/10.1063/1.2828711>.
- (69) Chu, C.-W.; Li, S.-H.; Chen, C.-W.; Shrotriya, V.; Yang, Y. High-Performance Organic Thin-Film Transistors with Metal Oxide/Metal Bilayer Electrode. *Appl. Phys. Lett.* **2005**, *87* (19), 193508. <https://doi.org/10.1063/1.2126140>.
- (70) Yao, Z. Q.; Liu, S. L.; Zhang, L.; He, B.; Kumar, A.; Jiang, X.; Zhang, W. J.; Shao, G. Room Temperature Fabrication of P-Channel Cu<sub>2</sub>O Thin-Film Transistors on Flexible Polyethylene Terephthalate Substrates. *Appl. Phys. Lett.* **2012**, *101* (4), 42114. <https://doi.org/10.1063/1.4739524>.
- (71) Gwinner, M. C.; Vaynzof, Y.; Banger, K. K.; Ho, P. K. H.; Friend, R. H.; Sirringhaus, H. Solution-Processed Zinc Oxide as High-Performance Air-Stable Electron Injector in Organic Ambipolar Light-Emitting Field-Effect Transistors. *Adv. Funct. Mater.* **2010**, *20* (20), 3457–3465. <https://doi.org/https://doi.org/10.1002/adfm.201000785>.
- (72) Wang, Z. B.; Helander, M. G.; Qiu, J.; Puzzo, D. P.; Greiner, M. T.; Hudson, Z. M.; Wang, S.; Liu, Z. W.; Lu, Z. H. Unlocking the Full Potential of Organic Light-Emitting Diodes on Flexible Plastic. *Nat. Photonics* **2011**, *5* (12), 753–757. <https://doi.org/10.1038/nphoton.2011.259>.
- (73) He, Z.; Zhong, C.; Su, S.; Xu, M.; Wu, H.; Cao, Y. Enhanced Power-Conversion Efficiency in Polymer Solar Cells Using an Inverted Device Structure. *Nat. Photonics* **2012**, *6* (9), 591–595. <https://doi.org/10.1038/nphoton.2012.190>.
- (74) Greiner, M. T.; Chai, L.; Helander, M. G.; Tang, W.-M.; Lu, Z.-H. Transition Metal Oxide Work Functions: The Influence of Cation Oxidation State and Oxygen Vacancies. *Adv. Funct. Mater.* **2012**, *22* (21), 4557–4568.

- <https://doi.org/https://doi.org/10.1002/adfm.201200615>.
- (75) Understanding How Excess Lead Iodide Precursor Improves Halide Perovskite Solar Cell Performance. *Nat. Commun.* <https://doi.org/10.1038/s41467-018-05583-w>.
- (76) Pérez-Del-Rey, D.; Gil-Escríg, L.; Zanoni, K. P. S.; Dreessen, C.; Sessolo, M.; Boix, P. P.; Bolink, H. J. Molecular Passivation of MoO<sub>3</sub>: Band Alignment and Protection of Charge Transport Layers in Vacuum-Deposited Perovskite Solar Cells. *Chem. Mater.* **2019**, *31* (17). <https://doi.org/10.1021/acs.chemmater.9b01396>.
- (77) Wang, S.; Wang, A.; Deng, X.; Xie, L.; Xiao, A.; Li, C.; Xiang, Y.; Li, T.; Ding, L.; Hao, F. Lewis Acid/Base Approach for Efficacious Defect Passivation in Perovskite Solar Cells. *J. Mater. Chem. A* **2020**, *8* (25), 12201–12225. <https://doi.org/10.1039/D0TA03957H>.
- (78) Yantara, N.; Sabba, D.; Yanan, F.; Kadro, J. M.; Moehl, T.; Boix, P. P.; Mhaisalkar, S.; Grätzel, M.; Grätzel, C. Loading of Mesoporous Titania Films by CH<sub>3</sub>NH<sub>3</sub>PbI<sub>3</sub> Perovskite, Single Step vs. Sequential Deposition. *Chem. Commun.* **2015**, *51* (22), 4603–4606. <https://doi.org/10.1039/C4CC09556A>.
- (79) Chandiran, A. K.; Yella, A.; Stefk, M.; Heiniger, L.-P.; Comte, P.; Nazeeruddin, M. K.; Grätzel, M. Low-Temperature Crystalline Titanium Dioxide by Atomic Layer Deposition for Dye-Sensitized Solar Cells. *ACS Appl. Mater. Interfaces* **2013**, *5* (8), 3487–3493. <https://doi.org/10.1021/am400866s>.
- (80) Ke, W.; Fang, G.; Wang, J.; Qin, P.; Tao, H.; Lei, H.; Liu, Q.; Dai, X.; Zhao, X. Perovskite Solar Cell with an Efficient TiO<sub>2</sub> Compact Film. *ACS Appl. Mater. Interfaces* **2014**, *6* (18), 15959–15965. <https://doi.org/10.1021/am503728d>.
- (81) Su, T.-S.; Hsieh, T.-Y.; Hong, C.-Y.; Wei, T.-C. Electrodeposited Ultrathin TiO<sub>2</sub> Blocking Layers for Efficient Perovskite Solar Cells. *Sci. Rep.* **2015**, *5* (1), 16098. <https://doi.org/10.1038/srep16098>.
- (82) Momblona, C.; Gil-Escríg, L. L.; Bandiello, E.; Sessolo, M.; Hutter, E. M.; Lederer, K.; Blochwitz-Nimoth, J. B.-N.; Bolink, H. J.; Sessolo, M.; Lederer, K.; et al. Efficient Vacuum Deposited P-i-n and n-i-p Perovskite Solar Cells Employing Doped Charge Transport Layers. *Energy Environ. Sci.* **2016**, *9* (11), 3456–3463. <https://doi.org/10.1039/C6EE02100J>.
- (83) Alnuaimi, A.; Almansouri, I.; Nayfeh, A. Effect of Mobility and Band Structure of Hole Transport Layer in Planar Heterojunction Perovskite Solar Cells Using 2D TCAD Simulation. *J. Comput. Electron.* **2016**, *15* (3),

- 1110–1118. <https://doi.org/10.1007/s10825-016-0850-1>.
- (84) Habisreutinger, S. N.; McMeekin, D. P.; Snaith, H. J.; Nicholas, R. J. Research Update: Strategies for Improving the Stability of Perovskite Solar Cells. *APL Mater.* **2016**, *4* (9), 91503. <https://doi.org/10.1063/1.4961210>.
- (85) Olthof, S.; Meerholz, K. Substrate-Dependent Electronic Structure and Film Formation of MAPbI<sub>3</sub> Perovskites. *Sci. Rep.* **2017**, *7* (1), 40267. <https://doi.org/10.1038/srep40267>.
- (86) Shallcross, R. C.; Olthof, S.; Meerholz, K.; Armstrong, N. R. Impact of Titanium Dioxide Surface Defects on the Interfacial Composition and Energetics of Evaporated Perovskite Active Layers. *ACS Appl. Mater. Interfaces* **2019**, *11* (35), 32500–32508. <https://doi.org/10.1021/acsami.9b09935>.
- (87) Kim, J. B.; Ahn, S.; Kang, S. J.; Nuckolls, C.; Loo, Y.; Kim, J. B.; Ahn, S.; Kang, J.; Nuckolls, C.; Loo, Y. Ligand Chemistry of Titania Precursor Affects Transient Photovoltaic Behavior in Inverted Organic Solar Cells Ligand Chemistry of Titania Precursor Affects Transient Photovoltaic Behavior in Inverted Organic Solar Cells. **2013**, *103302*. <https://doi.org/10.1063/1.4795287>.
- (88) Zhang, T.; Cheung, S. H.; Meng, X.; Zhu, L.; Bai, Y.; Ho, C. H. Y.; Xiao, S.; Xue, Q.; So, S. K.; Yang, S. Pinning Down the Anomalous Light Soaking Effect toward High-Performance and Fast-Response Perovskite Solar Cells: The Ion-Migration-Induced Charge Accumulation. *J. Phys. Chem. Lett.* **2017**, *8* (20), 5069–5076. <https://doi.org/10.1021/acs.jpclett.7b02160>.
- (89) Rühle, S. Tabulated Values of the Shockley–Queisser Limit for Single Junction Solar Cells. *Sol. Energy* **2016**, *130*, 139–147. <https://doi.org/https://doi.org/10.1016/j.solener.2016.02.015>.
- (90) Zheng, X.; Hou, Y.; Bao, C.; Yin, J.; Yuan, F.; Huang, Z.; Song, K.; Liu, J.; Troughton, J.; Gasparini, N.; et al. Managing Grains and Interfaces via Ligand Anchoring Enables 22.3%-Efficiency Inverted Perovskite Solar Cells. *Nat. Energy* **2020**, *5* (2), 131–140. <https://doi.org/10.1038/s41560-019-0538-4>.
- (91) Tokito, S.; Noda, K.; Taga, Y. Metal Oxides as a Hole-Injecting Layer for an Organic Electroluminescent Device. *J. Phys. D. Appl. Phys.* **1996**, *29* (11), 2750–2753. <https://doi.org/10.1088/0022-3727/29/11/004>.
- (92) Greiner, M. T.; Lu, Z.-H. Thin-Film Metal Oxides in Organic Semiconductor Devices: Their Electronic Structures, Work Functions

- and Interfaces. *NPG Asia Mater.* **2013**, *5* (7), e55–e55. <https://doi.org/10.1038/am.2013.29>.
- (93) Ru, P.; Bi, E.; Zhang, Y.; Wang, Y.; Kong, W.; Sha, Y.; Tang, W.; Zhang, P.; Wu, Y.; Chen, W.; et al. High Electron Affinity Enables Fast Hole Extraction for Efficient Flexible Inverted Perovskite Solar Cells. *Adv. Energy Mater.* **2020**, *10* (12), 1903487. <https://doi.org/https://doi.org/10.1002/aenm.201903487>.
- (94) Kanai, K.; Koizumi, K.; Ouchi, S.; Tsukamoto, Y.; Sakanoue, K.; Ouchi, Y.; Seki, K. Electronic Structure of Anode Interface with Molybdenum Oxide Buffer Layer. *Org. Electron.* **2010**, *11* (2), 188–194. <https://doi.org/https://doi.org/10.1016/j.orgel.2009.10.013>.
- (95) Meyer, J.; Zilberberg, K.; Riedl, T.; Kahn, A. Electronic Structure of Vanadium Pentoxide: An Efficient Hole Injector for Organic Electronic Materials. *J. Appl. Phys.* **2011**, *110* (3), 33710. <https://doi.org/10.1063/1.3611392>.
- (96) Zhao, Y.; Chen, J.; Chen, W.; Ma, D. Poly(3,4-Ethylenedioxythiophene):Poly(Styrenesulfonate)/MoO<sub>3</sub> Composite Layer for Efficient and Stable Hole Injection in Organic Semiconductors. *J. Appl. Phys.* **2012**, *111* (4), 43716. <https://doi.org/10.1063/1.3687933>.
- (97) Meyer, J.; Hamwi, S.; Bülow, T.; Johannes, H.-H.; Riedl, T.; Kowalsky, W. Highly Efficient Simplified Organic Light Emitting Diodes. *Appl. Phys. Lett.* **2007**, *91* (11), 113506. <https://doi.org/10.1063/1.2784176>.
- (98) Kröger, M.; Hamwi, S.; Meyer, J.; Riedl, T.; Kowalsky, W.; Kahn, A. Role of the Deep-Lying Electronic States of MoO<sub>3</sub> in the Enhancement of Hole-Injection in Organic Thin Films. *Appl. Phys. Lett.* **2009**, *95* (12), 123301. <https://doi.org/10.1063/1.3231928>.
- (99) Chen, L.-M.; Hong, Z.; Li, G.; Yang, Y. Recent Progress in Polymer Solar Cells: Manipulation of Polymer:Fullerene Morphology and the Formation of Efficient Inverted Polymer Solar Cells. *Adv. Mater.* **2009**, *21* (14–15), 1434–1449. <https://doi.org/https://doi.org/10.1002/adma.200802854>.
- (100) Kim, D. Y.; Subbiah, J.; Sarasqueta, G.; So, F.; Ding, H.; Irfan; Gao, Y. The Effect of Molybdenum Oxide Interlayer on Organic Photovoltaic Cells. *Appl. Phys. Lett.* **2009**, *95* (9), 93304. <https://doi.org/10.1063/1.3220064>.
- (101) Dasgupta, B.; Goh, W. P.; Ooi, Z. E.; Wong, L. M.; Jiang, C. Y.; Ren, Y.; Tok, E. S.; Pan, J.; Zhang, J.; Chiam, S. Y. Enhanced Extraction Rates

- through Gap States of Molybdenum Oxide Anode Buffer. *J. Phys. Chem. C* **2013**, *117* (18), 9206–9211. <https://doi.org/10.1021/jp3114013>.
- (102) Meyer, J.; Hamwi, S.; Kröger, M.; Kowalsky, W.; Riedl, T.; Kahn, A. Transition Metal Oxides for Organic Electronics: Energetics, Device Physics and Applications. *Adv. Mater.* **2012**, *24* (40), 5408–5427. <https://doi.org/10.1002/adma.201201630>.
- (103) Greiner, M. T.; Helander, M. G.; Tang, W.-M.; Wang, Z.-B.; Qiu, J.; Lu, Z.-H. Universal Energy-Level Alignment of Molecules on Metal Oxides. *Nat. Mater.* **2012**, *11* (1), 76–81. <https://doi.org/10.1038/nmat3159>.
- (104) Kotadiya, N. B.; Lu, H.; Mondal, A.; Ie, Y.; Andrienko, D.; Blom, P. W. M.; Wetzelar, G.-J. A. H. Publisher Correction: Universal Strategy for Ohmic Hole Injection into Organic Semiconductors with High Ionization Energies. *Nat. Mater.* **2018**, *17* (6), 563. <https://doi.org/10.1038/s41563-018-0043-3>.
- (105) Zapf, P. J.; Haushalter, R. C.; Zubieto, J. Hydrothermal Synthesis and Structural Characterization of a Series of One-Dimensional Organic/Inorganic Hybrid Materials of the  $[(\text{MoO}_3)_n(2,2'\text{-Bipy})_m]$  Family:  $[\text{MoO}_3(2,2'\text{-Bipy})]$ ,  $[\text{Mo}_2\text{O}_6(2,2'\text{-Bipy})]$ , and  $[\text{Mo}_3\text{O}_9(2,2'\text{-Bipy})_2]$ . *Chem. Mater.* **1997**, *9* (9), 2019–2024. <https://doi.org/10.1021/cm970260o>.
- (106) Abrantes, M.; Amarante, T. R.; Antunes, M. M.; Gago, S.; Almeida Paz, F. A.; Margiolaki, I.; Rodrigues, A. E.; Pillinger, M.; Valente, A. A.; Gonçalves, I. S. Synthesis, Structure, and Catalytic Performance in Cyclooctene Epoxidation of a Molybdenum Oxide/Bipyridine Hybrid Material:  $\{[\text{MoO}_3(\text{Bipy})][\text{MoO}_3(\text{H}_2\text{O})]\}_n$ . *Inorg. Chem.* **2010**, *49* (15), 6865–6873. <https://doi.org/10.1021/ic100479a>.
- (107) White, R. T.; Thibau, E. S.; Lu, Z.-H. Interface Structure of MoO<sub>3</sub> on Organic Semiconductors. *Sci. Rep.* **2016**, *6*, 21109.
- (108) Park, N.-G.; Zhu, K. Scalable Fabrication and Coating Methods for Perovskite Solar Cells and Solar Modules. *Nat. Rev. Mater.* **2020**, *5* (5), 333–350. <https://doi.org/10.1038/s41578-019-0176-2>.
- (109) Miyasaka, T. Lead Halide Perovskites in Thin Film Photovoltaics: Background and Perspectives. *Bull. Chem. Soc. Jpn.* **2018**, *91* (7), 1058–1068. <https://doi.org/10.1246/bcsj.20180071>.
- (110) Woodyard, J. R.; Landis, G. A. Radiation Resistance of Thin-Film Solar Cells for Space Photovoltaic Power. *Sol. Cells* **1991**, *31* (4), 297–329. [https://doi.org/https://doi.org/10.1016/0379-6787\(91\)90103-V](https://doi.org/https://doi.org/10.1016/0379-6787(91)90103-V).

- (111) Cho, B.; Davis, J.; Hise, L.; Korostyshevsky, A.; Smith, G.; Ley, A. V.; Sharps, P.; Varghese, T.; Stan, M. Qualification Testing of the ZTJ GaInP<sub>2</sub>/GaInAs/Ge Solar Cell to the AIAA S-111 Standard. In *2009 34th IEEE Photovoltaic Specialists Conference (PVSC)*; 2009; pp 1009–1014. <https://doi.org/10.1109/PVSC.2009.5411193>.
- (112) Yamaguchi, M.; Taylor, S. J.; Matsuda, S.; Kawasaki, O. Mechanism for the Anomalous Degradation of Si Solar Cells Induced by High Fluence 1 MeV Electron Irradiation. *Appl. Phys. Lett.* **1996**, *68* (22), 3141–3143. <https://doi.org/10.1063/1.115804>.
- (113) Kaltenbrunner, M.; Adam, G.; Głowacki, E. D.; Drack, M.; Schwödauer, R.; Leonat, L.; Apaydin, D. H.; Groiss, H.; Scharber, M. C.; White, M. S.; et al. Flexible High Power-per-Weight Perovskite Solar Cells with Chromium Oxide–Metal Contacts for Improved Stability in Air. *Nat. Mater.* **2015**, *14* (10), 1032–1039. <https://doi.org/10.1038/nmat4388>.
- (114) Chirvony, V. S.; Sekerbayev, K. S.; Pérez-Del-Rey, D.; Martínez-Pastor, J. P.; Palazon, F.; Boix, P. P.; Taurbayev, T. I.; Sessolo, M.; Bolink, H. J. Short Photoluminescence Lifetimes in Vacuum-Deposited CH<sub>3</sub>NH<sub>3</sub>PbI<sub>3</sub> Perovskite Thin Films as a Result of Fast Diffusion of Photogenerated Charge Carriers. *J. Phys. Chem. Lett.* **2019**, *10* (17). <https://doi.org/10.1021/acs.jpclett.9b02329>.
- (115) Danilchenko, B.; Budnyk, A.; Shpinar, L.; Poplavskyy, D.; Zelensky, S. E.; Barnham, K. W. J.; Ekins-Daukes, N. J. 1MeV Electron Irradiation Influence on GaAs Solar Cell Performance. *Sol. Energy Mater. Sol. Cells* **2008**, *92* (11), 1336–1340. <https://doi.org/https://doi.org/10.1016/j.solmat.2008.05.006>.
- (116) Klein-Kedem, N.; Cahen, D.; Hodes, G. Effects of Light and Electron Beam Irradiation on Halide Perovskites and Their Solar Cells. *Acc. Chem. Res.* **2016**, *49* (2), 347–354. <https://doi.org/10.1021/acs.accounts.5b00469>.
- (117) Hentz, O.; Zhao, Z.; Gradečák, S. Impacts of Ion Segregation on Local Optical Properties in Mixed Halide Perovskite Films. *Nano Lett.* **2016**, *16* (2), 1485–1490. <https://doi.org/10.1021/acs.nanolett.5b05181>.
- (118) Miyazawa, Y.; Ikegami, M.; Chen, H.-W.; Ohshima, T.; Imaizumi, M.; Hirose, K.; Miyasaka, T. Tolerance of Perovskite Solar Cell to High-Energy Particle Irradiations in Space Environment. *iScience* **2018**, *2*, 148–155. <https://doi.org/https://doi.org/10.1016/j.isci.2018.03.020>.
- (119) Huang, J.; Kelzenberg, M. D.; Espinet-González, P.; Mann, C.; Walker,

- D.; Naqavi, A.; Vaidya, N.; Warmann, E.; Atwater, H. A. Effects of Electron and Proton Radiation on Perovskite Solar Cells for Space Solar Power Application. In *2017 IEEE 44th Photovoltaic Specialist Conference (PVSC)*; 2017; pp 1248–1252. <https://doi.org/10.1109/PVSC.2017.8366410>.
- (120) Xiao, C.; Li, Z.; Guthrey, H.; Moseley, J.; Yang, Y.; Wozny, S.; Moutinho, H.; To, B.; Berry, J. J.; Gorman, B.; et al. Mechanisms of Electron-Beam-Induced Damage in Perovskite Thin Films Revealed by Cathodoluminescence Spectroscopy. *J. Phys. Chem. C* **2015**, *119* (48), 26904–26911. <https://doi.org/10.1021/acs.jpcc.5b09698>.
- (121) Song, Z.; Li, C.; Chen, C.; McNatt, J.; Yoon, W.; Scheiman, D.; Jenkins, P. P.; Ellingson, R. J.; Heben, M. J.; Yan, Y. High Remaining Factors in the Photovoltaic Performance of Perovskite Solar Cells after High-Fluence Electron Beam Irradiations. *J. Phys. Chem. C* **2020**, *124* (2), 1330–1336. <https://doi.org/10.1021/acs.jpcc.9b11483>.
- (122) Jiang, N. Electron Beam Damage in Oxides: A Review. *Reports Prog. Phys.* **2015**, *79* (1), 16501. <https://doi.org/10.1088/0034-4885/79/1/016501>.
- (123) Neelisetty, K. K.; Mu, X.; Gutsch, S.; Vahl, A.; Molinari, A.; von Seggern, F.; Hansen, M.; Scherer, T.; Zacharias, M.; Kienle, L.; et al. Electron Beam Effects on Oxide Thin Films—Structure and Electrical Property Correlations. *Microsc. Microanal.* **2019**, *25* (3), 592–600. <https://doi.org/DOI: 10.1017/S1431927619000175>.
- (124) Egerton, R. F. Radiation Damage to Organic and Inorganic Specimens in the TEM. *Micron* **2019**, *119*, 72–87. <https://doi.org/https://doi.org/10.1016/j.micron.2019.01.005>.
- (125) Herbert Schulman, J.; Dale Compton, W. *Color Centers in Solids*; Oxford, Pergamon Press, 1962.
- (126) Dong, S.; Valerio, A.; Riccardo, C.; Mingjian, Y.; Erkki, A.; Andrei, B.; Yin, C.; Sjoerd, H.; Alexander, R.; Khabiboulakh, K.; et al. Low Trap-State Density and Long Carrier Diffusion in Organolead Trihalide Perovskite Single Crystals. *Science (80-. ).* **2015**, *347* (6221), 519–522. <https://doi.org/10.1126/science.aaa2725>.
- (127) Momblona, C.; Gil-Escríg, L.; Bandiello, E.; Hutter, E. M.; Sessolo, M.; Lederer, K.; Blochwitz-Nimoth, J.; Bolink, H. J. Efficient Vacuum Deposited P-i-n and n-i-p Perovskite Solar Cells Employing Doped Charge Transport Layers. *Energy Environ. Sci.* **2016**, *9* (11), 3456–3463. <https://doi.org/10.1039/C6EE02100J>.

- (128) Kaltenbrunner, M.; Adam, G.; Głowacki, E. D.; Drack, M.; Schwödiauer, R.; Leonat, L.; Apaydin, D. H.; Groiss, H.; Scharber, M. C.; White, M. S.; et al. Flexible High Power-per-Weight Perovskite Solar Cells with Chromium Oxide–Metal Contacts for Improved Stability in Air. *Nat. Mater.* **2015**, *14* (10), 1032–1039. <https://doi.org/10.1038/nmat4388>.



## Index of figures

<b>Figure 1:</b> Global energy generation by source. Caption from reference 1	19
<b>Figure 2:</b> P-i-N device architecture (a) and potential profile (b).	22
<b>Figure 3:</b> Perovskite general $ABX_3$ crystal structure. Figure from reference 6.	23
<b>Figure 4:</b> Tolerance factors of the most used perovskites for photovoltaic applications.	23
<b>Figure 5:</b> Band diagram of $\text{CH}_3\text{NH}_3\text{PbI}_3$ . Image from reference 11.	24
<b>Figure 6:</b> Most employed deposition techniques for the preparation of perovskite layers. 1 step deposition (a), 2 step deposition via solution processing of both components or a combination of solution processing and vacuum deposition (b) and co-evaporation (c).	27
<b>Figure 7:</b> Valence and conduction bands of different metal oxides used as transport layers in perovskite solar cells. Image from reference 71.	31
<b>Figure 8:</b> Chemical structures of the molecules TaTm, F <sub>6</sub> -TCNNQ, BCP, C <sub>60</sub> and PhIm.	36
<b>Figure 9:</b> Basic schematic of the evaporation chamber and real picture of a similar chamber.	37
<b>Figure 10:</b> Schematic of the P-i-N structure (not to scale)	39
<b>Figure 11:</b> EQE measurement of a MAPI perovskite solar cell.	42
<b>Figure 12:</b> Simplified equivalent circuit model of a solar cell (diode).	43

**Figure 13:** J-V curve under dark conditions of a perovskite solar cell in semilogarithmic scale. 44

**Figure 14:** J-V curves in dark (blue) and under illumination (red) highlighting the  $V_{oc}$ ,  $J_{sc}$  and maximum power points, with common simplified band diagrams for each working regime. 46

**Figure 15:** Solar cell layouts employed in this thesis. ITO and top metal are the bottom and top contacts, respectively. 47

**Figure 16:** Energy levels of  $TiO_2$ ,  $SnO_2$  and MAPI perovskite. 52

**Figure 17:** J-V curves of N-i-P solar cells using  $TiO_2$  with (b) and without (a)  $C_{60}$  interlayer measured under a xenon lamp. Arrows indicate scan direction (negative to positive voltage bias and vice-versa). 54

**Figure 18:** Statistical distribution of the power conversion efficiency obtained for the fully evaporated devices from reference 82 and for our configuration employing  $TiO_2/C_{60}$  (left) and J-V curve of the best device (right). 56

**Figure 19:** Energy levels of the main TMOs for optoelectronic applications (figure from reference 92) 74

**Figure 20:** Energy level alignment and band bending between  $MoO_3$  and an organic HTL and sub-gap defect states of  $MoO_3$  (figures from references <sup>102</sup> and 92). 75

**Figure 21:** P-i-N device architecture (a), dark J-V curve in semilogarithmic scale (b) and illuminated J-V curve in linear scale (c) of devices comparing the effects of annealing and TPBi on the  $MoO_3$  layer. 77

**Figure 22:** J-V curves under AM1.5G illumination and energy levels of P-i-N solar cells using molecules with different HOMO energies on top of  $MoO_3$  not annealed. The sample of  $MoO_3$  annealed works as a reference. Dashed lines stand for reverse scan. 78

**Figure 23:** Schematic device architectures of n-i-p devices with (a) and without (b) TPBi interlayer. (c) J-V curves under AM1.5G illumination corresponding to devices with 0, 2, and 5 nm-thick TPBi interlayers. Dashed lines stand for reverse scan. 79

**Figure 24:** J-V curves of N-i-P solar cells under AM1.5G illumination with different molecules on top of TaTm and their chemical structures. 80

**Figure 25:** Quartz substrate-based PSCs. a) J-V curves obtained under 1 sun illumination for solar cells exposed to different accumulated fluences. b–e) PCE,  $J_{sc}$ ,  $V_{oc}$ , and FF versus accumulated electron fluence, respectively, of the quartz substrate-based solar cells. Closed symbols are the values before irradiation and open symbols are after irradiation 99

**Figure 26:** Fluorescence spectrum of devices irradiated at different electron doses in linear (a) and logarithmic scale (b). An excitation wavelength of 350 nm was used. 100

**Figure 27:** XRD spectra (a) and SEM images (b) of perovskite samples deposited on glass and capped with PMMA as encapsulation, which were exposed to different electron doses. 101



## Index of tables

<b>Table 1:</b> Solar cell parameters under full solar spectrum illumination. The measurements were performed first in reverse (from positive to negative bias) and immediately afterwards in forward direction (from negative to positive bias).	55
<b>Table 2:</b> Record device with the corresponding photovoltaic parameters.	57
<b>Table 3:</b> Average solar cell parameters for P-i-N solar cells with the MoO <sub>3</sub> layer at the front contact.	78
<b>Table 4:</b> Average PV parameters of N-i-P solar cells with MoO <sub>3</sub> on top of TaTm and on top of TaTm/TPBi.	80
<b>Table 5:</b> Photovoltaic parameters of n-i-p solar cells with different interlayers between TaTm and MoO <sub>3</sub> .	81



## Abbreviations

PV	Photovoltaic
CdTe	Cadmium Teluride
CIGS	Copper Indium Gallium Selenide
GaAs	Gallium Arsenide
CZTS	Copper Zinc Tin Sulfide
$E_g$	Bandgap Energy
PSC	Perovskite Solar Cell
$E_F$	Fermi level energy
$V_{bi}$	Built-in voltage
$E_c$	Conduction band energy
$E_v$	Valence band energy
$e^-$	Electron
$h^+$	Hole
$\text{CaTiO}_3$	Calcium Titanate
$\text{ABX}_3$	Perovskite general structure
r	Atomic radius
t	Goldschmidt tolerance factor
MA	Methylammonium cation ( $\text{CH}_3\text{NH}_3^+$ )
MAI	Methylammonium iodide ( $\text{CH}_3\text{NH}_3\text{I}$ )
FA	Formamidinium cation ( $\text{NH}_2\text{CHNH}_2^+$ )
MAPI	Methylammonium lead triiodide perovskite $(\text{CH}_3\text{NH}_3\text{PbI}_3)$
DMF	N,N dimethylformamide
DMSO	Dimethyl sulfoxide

GBL	$\gamma$ -butyrolactone
QCM	Quartz crystal microbalance
DSSC	Dye-sensitized solar cell
HTL	Hole transport layer
ETL	Electron transport layer
HIL	Hole injection layer
PEDOT:PSS	Poly(3,4-ethylenedioxythiophene) poly(styrenesulfonate)
PTAA	Poly[bis(4-phenyl)(2,4,6-trimethylphenyl)amine]
TaTm	(N4,N4,N4'',N4''-tetra([1,1'-biphenyl]-4-yl)- [1,1':4',1''-terphenyl]-4,4''-diamine)
Spiro-OMeTAD	2,2',7,7'-tetrakis(N,N-di-p-methoxyphenylamine)- 9,9'-spirobifluorene
HOMO	Highest occupied molecular orbital
LUMO	Lowest unoccupied molecular orbital
ALD	Atomic layer deposition
OLED	Organic light-emitting diode
OPV	Organic photovoltaics
OFET	Organic field-effect transistor
TCO	Transparent conductive oxide
ITO	Indium Tin Oxide
F <sub>6</sub> -TCNNQ	2,2'-(Perfluoronaphthalene2,6-diylidene) dimalononitrile
PhIm	N1,N4-bis(tri-ptolylphosphoranyli-dene) benzene- 1,4-diamine
BCP	2,9-Dimethyl-4,7-diphenyl-1,10-phenanthroline

TPBi	2,2',2''-(1,3,5-Benzenetriyl)-tris(1-phenyl-1-H-benzimidazole)
IMEC	Interuniversity Microelectronics Centre
TCI	Tokyo Chemical Industry CO
XRD	X-ray diffraction
SEM	Scanning electron microscopy
EQE	External quantum efficiency
IPCE	Incident photon to current efficiency
J-V	Current density versus voltage
R <sub>SH</sub>	Shunt resistance
R <sub>s</sub>	Series resistance
I <sub>D</sub>	Diode current
I <sub>L</sub>	Illumination current
I <sub>SH</sub>	Shunt current
J <sub>sc</sub>	Short circuit current
V <sub>oc</sub>	Open circuit voltage
MPP	Maximum power point
FF	Fill factor
PCE	Power conversion efficiency
AM1.5G	Standard sun spectrum at earth's surface
CBM	Conduction band minimum
VBM	Valence band maximum
UV	Ultraviolet
PET	Polyethylene terephthalate
TMO	Transition metal oxide
TCTA	Tris(4-carbazoyl-9-ylphenyl)amine

TRMC	Time-resolved microwave conductivity
PMMA	Poly(methyl methacrylate)

## List of publications

- 1: **Daniel Pérez-del-Rey**, Dávid Forgács, Eline M. Hutter, Tom J. Savenije, Dennis Nordlund, Philip Schulz, Joseph J. Berry, Michele Sessolo, Henk J. Bolink (2016). “Strontium Insertion in Methylammonium Lead Iodide: Long Charge Carrier Lifetime and High Fill-Factor Solar Cells”. **Adv. Mater.**, 28: 9839–9845. <https://doi.org/10.1002/adma.201603016>
- 2: Dávid Forgács, **Daniel Pérez-del-Rey**, Jorge Ávila, Cristina Momblona, Lidón Gil-Escríg, Benedikt Dänekamp, Michele Sessolo and Henk J. Bolink (2017). “Efficient wide band gap double cation – double halide perovskite solar cells”. **J. Mater. Chem. A**, 2017, 5, 3203–3207.  
<https://doi.org/10.1039/C6TA10727C>
- 3: Dávid Forgács, Lidón Gil-Escríg, **Daniel Pérez-Del-Rey**, Cristina Momblona, Jérémie Werner, Bjoern Niesen, Christophe Ballif, Michele Sessolo, Henk J. Bolink (2017). “Efficient Monolithic Perovskite/Perovskite Tandem Solar Cells”. **Adv. Energy Mater.** 2017, 7, 1602121.  
<https://doi.org/10.1002/aenm.201602121>
- 4: **Daniel Pérez-del-Rey**, Pablo P. Boix, Michele Sessolo, Afshin Hadipour, Henk J. Bolink (2018). “Interfacial Modification for High-Efficiency Vapor-Phase-Deposited Perovskite Solar Cells Based on a Metal Oxide Buffer Layer”. **J. Phys. Chem. Lett.** 2018, 9, 5, 1041–1046.  
<https://doi.org/10.1021/acs.jpclett.7b03361>
- 5: Francisco Palazón, **Daniel Pérez-del-Rey**, Sergio Marras, Mirko Prato, Michele Sessolo, Henk J. Bolink, Liberato Manna (2018). “Coating Evaporated MAPI Thin Films with Organic Molecules: Improved Stability at High Temperature and Implementation in High-Efficiency Solar Cells”. **ACS Energy Lett.** 2018, 3, 4, 835–839. <https://doi.org/10.1021/acsenergylett.8b00193>

6: Azin Babaei, Laura Albero-Blanquer, Ana María Igual-Muñoz, **Daniel Pérez-Del-Rey**, Michele Sessolo, Henk J Bolink, Rawad Tadmouri (2018). "Hansen theory applied to the identification of nonhazardous solvents for hybrid perovskite thin-films processing". **Polyhedron**, 2018, 147, 9-14.  
<https://doi.org/10.1016/j.poly.2018.03.003>

7: Vahid Fallah Hamidabadi, Cristina Momblona, **Daniel Pérez-Del-Rey**, Ali Bahari, Michele Sessolo, Henk J. Bolink (2019). "Phosphomolybdic acid as an efficient hole injection material in perovskite optoelectronic devices". **Dalton Trans.**, 2019, 48, 30-34. <https://doi.org/10.1039/C8DT03680B>

8: **Daniel Pérez-del-Rey**, Lidón Gil-Escríg, Kassio P.S. Zanoni, Chris Dreessen, Michele Sessolo, Pablo P. Boix, Henk J. Bolink (2019). "Molecular Passivation of MoO<sub>3</sub>: Band Alignment and Protection of Charge Transport Layers in Vacuum-Deposited Perovskite Solar Cells". **Chem. Mater.** 2019, 31, 17, 6945–6949. <https://doi.org/10.1021/acs.chemmater.9b01396>

9: Martin T. Neukom, Andreas Schiller, Simon Züfle, Evelyne Knapp, Jorge Ávila, **Daniel Pérez-del-Rey**, Chris Dreessen, Kassio P.S. Zanoni, Michele Sessolo, Henk J. Bolink, Beat Ruhstaller (2019). "Consistent Device Simulation Model Describing Perovskite Solar Cells in Steady-State, Transient, and Frequency Domain". **ACS Appl. Mater. Interfaces** 2019, 11, 26, 23320–23328. <https://doi.org/10.1021/acsami.9b04991>

10: Vladimir S. Chirvony, Kairolla S. Sekerbayev, **Daniel Pérez-del-Rey**, Juan P. Martínez-Pastor, Francisco Palazón, Pablo P. Boix, Toktar I. Taurbayev, Michele Sessolo, Henk J. Bolink (2019). "Short Photoluminescence Lifetimes in Vacuum-Deposited CH<sub>3</sub>NH<sub>3</sub>PbI<sub>3</sub> Perovskite Thin Films as a Result of Fast Diffusion of Photogenerated Charge Carriers". **J. Phys. Chem. Lett.** 2019, 10, 17, 5167–5172. <https://doi.org/10.1021/acs.jpclett.9b02329>

11: Francisco Palazón, **Daniel Pérez-del-Rey**, Benedikt Dänekamp, Chris Dreessen, Michele Sessolo, Pablo P. Boix, Henk J. Bolink (2019). "Room-Temperature Cubic Phase Crystallization and High Stability of Vacuum-Deposited Methylammonium Lead Triiodide Thin Films for High-Efficiency

Solar Cells". **Adv. Mater.** 2019, 31, 1902692.  
<https://doi.org/10.1002/adma.201902692>

12: Azin Babaei, Kassio P.S. Zanoni, Lidón Gil-Escríg, **Daniel Pérez-del-Rey**, Pablo P. Boix, Michele Sessolo, Henk J. Bolink (2020). "Efficient Vacuum Deposited P-I-N Perovskite Solar Cells by Front Contact Optimization". **Front. Chem.** 7:936. <https://doi.org/10.3389/fchem.2019.00936>

13: Kassio P.S. Zanoni, **Daniel Pérez-del-Rey**, Chris Dreessen, M<sup>a</sup> Ángeles Hernández-Fenollosa, Andrea S.S. De Camargo, Michele Sessolo, Pablo P. Boix, Henk J. Bolink (2020). "Use of Hydrogen Molybdenum Bronze in Vacuum-Deposited Perovskite Solar Cells". **Energy Technol.**, 8: 1900734. <https://doi.org/10.1002/ente.201900734>

14: Chris Dreessen, **Daniel Pérez-del-Rey**, Pablo P. Boix, Henk J. Bolink (2020). "Radiative and non-radiative losses by voltage-dependent in-situ photoluminescence in perovskite solar cell current-voltage curves". **Journal of Lum.**, 222, 2020, 117106. <https://doi.org/10.1016/j.jlumin.2020.117106>

15: Pedro Hierrezuelo-Cardet, Anderzon F. Palechor-Ocampo, Jorge Caram, Federico Ventosinos, **Daniel Pérez-del-Rey**, Henk J. Bolink, Javier A. Schmidt (2020). "External quantum efficiency measurements used to study the stability of differently deposited perovskite solar cells". **Journal of Applied Physics** 127, 235501 (2020). <https://doi.org/10.1063/5.0011503>

16: **Daniel Pérez-del-Rey**, Chris Dreessen, Ana M. Igual-Muñoz, Lennart van den Hengel, María C. Gélvez-Rueda, Tom J. Savenije, Ferdinand C. Grozema, Claus Zimmermann, Henk J. Bolink (2020). "Perovskite Solar Cells: Stable under Space Conditions". **Sol. RRL**, 4: 2000447. <https://doi.org/10.1002/solr.202000447>